D10.2

Energy storage solution for AC railway grid : A description document for the optimal design and control strategies of energy storage and interface converter for AC infrastructure

Project acronym:	Rail4EARTH
Starting date:	01/12/2022
Duration (in months):	48
Call (part) identifier:	
Grant agreement no:	101101917
Due date of deliverable:	Month 30
Actual submission date:	05/05/2025
Responsible/Author:	Qianwen XU (KTH)
Dissemination level:	PU
Status:	V2 Report

Reviewed: (yes/no)

This project has received funding from the European Union's Horizon Europe research and innovation programme under Grant Agreement No 101101917.

Disclaimer

The information contained in this document shall be treated as confidential, unless explicitly stated otherwise. Reproduction, modification, use or disclosure to third parties, is strictly prohibited. The FP4 - Rail4EARTH project under Grant Agreement n°101101917 is supported by the Europe's Rail Joint Undertaking and its members. Views and opinions expressed are however those of the author(s) only and do not necessarily reflect those of the European Union or the Europe's Rail Joint Undertaking. Neither the European Union nor the granting authority can be held responsible for them.

Document history		
Revision	*Date*	*Description*
1	04/05/2025	Submission for internal review
2	05/05/2025	Submission for SP review
3	13/05/2025	Submission for Project coordinator review

Report contributors		
Name	**Beneficiary Short Name**	**Details of contribution**
Matthias ASPLUND	TRV	Monitor progress
Qianwen Xu Yang ZHANG	KTH	Generations of ideas, writer & review
Niklas BIEDERMANN	TRV	Expert comments and suggestions
Stefan ÖSTLUND	KTH	Expert comments and suggestions
Benoit SONIER	SNCF	Internal WP review

Table of Contents

1. Executive Summary

The document depicts the advancement of task 10.2. This work develops a comprehensive system-level simulation model of the Swedish railway traction power system based on real-world field data. The model includes detailed sub-models of static frequency converters (both DC-link and multilevel topologies), electrical locomotives, catenary systems, high-voltage feeder lines, and traction transformers. Its validity is demonstrated through two representative case studies. Various energy storage solutions and corresponding interface converter technologies are investigated and evaluated for the energy storage system (ESS) deployment in railway applications, with a final focus on Li-ion batteries, supercapacitors, flywheel ESS and superconducting magnet energy system (SMES). A dedicated DC-AC converter topology is designed to support ESS integration, aiming to enhance voltage stability and facilitate regenerative braking energy recovery. The performance of the proposed converter, in combination with the four selected ESS technologies, is evaluated with and without a bidirectional DC-DC converter. Furthermore, a novel ESS integration method into existing static frequency converters is proposed to enable peak power shaving and improve the utilization of regenerative energy. This approach is demonstrated using a multilevel converter equipped with supercapacitors, with performance assessment conducted through the developed simulation framework.

2. Abbreviations and acronyms

Abbreviation / Acronym	Description
DC	Direct current
AC	Alternating current
TPS	Traction power substation
VSC	Voltage source converter
GTO	Gate turn-off thyristor
IGBT	Insulated gate bipolar transistor
RFC	Rotary frequency converter
SFC	Static frequency converter
BT	Booster transformer
AT	Autotransformer
OCS	Overhead catenary system
HV	High voltage
VSI	Voltage source inverter
PWM	Pulse-width modulation
ESS	Energy storage system
IGCT	Integrated gate-commutated thyristors
PI	Proportional-integral
PLL	Phase-locked loop
PR	Proportional-resonant
RMS	Root mean square
EMF	Electromotive force
PF	Power factor
THD	Total harmonic distortion
FFT	Fast Fourier transformation
PHES	Pumped hydroelectric storage
CAES	Compressed air energy storage
GES	Gravity energy storage
LA	Lead-Acid
Ni-Cd	Nickel-Cadmium
Li-ion	Lithium-Ion
Ni-MH	Nickel-Metal Hydride
LRV	Light rail vehicle
VRB	Vanadium redox battery
FC	Fuel cell
SMES	Superconducting magnetic energy storage
EDLC	Electrical double-layer capacitor
BESS	Battery ESS
SITRAS SES	Stationary Energy Storage System
WESS	Wayside ESS

PMSM	Permanent magnet synchronous machine
DAB	Dual active full-bridge
NPC	Neutral-point-clamped
MMC	Modular multi-level converter
CHB	Cascaded H-bridge
MPC	Model predictive control
HESS	Hybrid ESS
SOC	State of charge
UPS	Uninterruptible power supply
TCC	Total capital cost
PCS	Power conversion system
BOP	Balance-of-plant
LCC	Life cycle cost
O&M	Operation and maintenance
4QC	Four-quadrant converter
IPMSM	Interior permanent magnet synchronous motor
MPTA	Maximum torque per ampere
SVPWM	Space vector pulse-width modulation
FCS-MPC	Finite control set model predictive control

3. Background

Energy storage on alternating current (AC) rail networks represents an essential lever for improving the efficiency, resilience and sustainability of rail transport. In particular, it helps to smooth out power peaks associated with train acceleration phases, thus avoiding costly oversizing of electrical infrastructures. It also plays a key role in recovering braking energy, which is often lost due to a lack of simultaneous consumption on the AC network, by storing it for later use. By integrating renewable energy sources, storage helps to reduce the rail sector's carbon footprint. It also enhances network resilience by providing back-up power in the event of disruption. However, if the integration of energy storage systems in DC has been widely worked on in the last years, the integration of these systems on an AC network imposes specific technical constraints, notably synchronization with the network frequency, management of voltage variations and the use of high-performance AC/DC converters. These technical challenges need to be overcome if the full potential of energy storage in rail applications is to be realized.

4. Objective/Aim

This document has been prepared to provide intermediate results and report the status and progress of WP10 task 10.2 activities until M30.

WP10 has a duration of 48 months.

WP10 provides information, via the Rail4Earth WP28 consolidated STIP file, to System Pillar regarding the need for new or the modification of existing standards or regulations

5. Deliverables

This deliverable D10.2 “Design and control strategies for energy storage integration in AC Infrastructure: A description document for the optimal design and control strategies of energy storage and interface converter for AC infrastructure” is the second of the six deliverables agreed in WP10.

It follows deliverable D10.1 “Smart Infrastructure power supply intermediate report n°1” that has been issued in M16.

Below is presented the list of deliverables that will be produced in WP10:

- D10.3 – Design and control strategies of FACTS (Flexible Alternating Current Transmission Systems) solutions: Description of the optimal topologies and control strategies of the FACTS products according to the specifications (M36)
- D10.4 – Smart infrastructure power supply demonstrator integration studies: Presentation of the results of the simulations and the integration studies for the 2 solutions. Assessment of the relevance and feasibility of a demonstrator according to the potential sites (M48)
- D10.5 – Optimization algorithms for operation, sizing and placement of energy storage in AC infrastructure: A description document of for optimal operation, sizing and placement of energy storage (M48)
- D10.6 – AC & DC infrastructure use case demonstration: Presentation of the use cases (AC & DC) and of the results/outputs of the tool according to the objectives (M48)

6. Link to FA4 KPIs

- **Physical energy consumption** yes (direct)
  The proposed solution on the integration of ESSs into the Swedish railway traction network allows for effective peak shaving and enhanced utilization of regenerative braking energy. These improvements reduce the overall energy drawn from the grid, thereby directly lowering the physical energy consumption of the railway operations.
- **Physical CO2 equivalent emissions** yes (indirect)
  By guaranteeing the safety of system operations, enabling appropriate integration of ESSs, and enhancing energy efficiency, this work contributes to reduced reliance on fossil-based power generation and then indirectly supports a reduction in lifecycle CO_2 equivalent

emissions associated with propulsion and infrastructure energy use.

- **Life Cycle Costs reduction** yes (indirect)
  The analysis and comparison of multiple ESS technologies, considering efficiency, lifecycle, and cost per cycle, provide clear guidance on the most cost-effective solutions. The demonstrated benefits of EDLCs and flywheels in terms of lifecycle and energy utilization help inform investment decisions that reduce long-term operational and maintenance costs, contributing to lower overall life cycle costs for the railway traction system.

7. Task 10.2 advancement

6.1. Energy storage solution for AC railway grid

6.1.1. Introduction to modern electrified railway traction system in Europe

Since the early 20th century, railway electrification in Europe has primarily followed two major systems: direct current (DC) and alternating current (AC) [1], [2], as illustrated in Fig. 1.

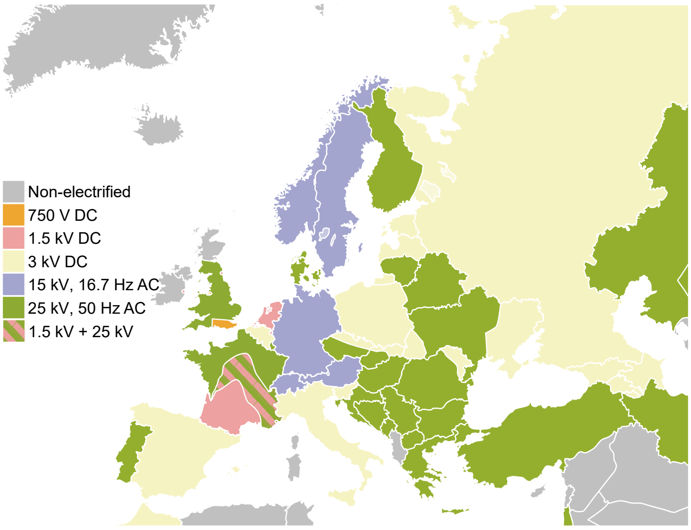

Fig. 1. Electrified railway traction system in Europe

The DC system is predominantly used in urban and suburban transport, including trams and metros, with operating voltages progressively increasing from 750 V to 1.5 kV and 3 kV. However, for historical and logistical reasons, DC traction remains in use on certain mainline railways. For instance, the 1.5 kV DC system is still prevalent in the eastern and southern regions of France, accounting for approximately 43% of the country's electrified railway network [3], and is also widely implemented in the Netherlands. Similarly, the 3 kV DC system was adopted in Belgium, Italy, Spain, Poland, Slovakia, Slovenia, northern Czech Republic, and the former Soviet republics, primarily to enhance railway transport capacity [4].

In contrast, AC electrification has been widely implemented in mainline railways across Europe. Based on voltage and frequency, AC systems are categorized into 15 kV - 16⅔ Hz (16.7 Hz) and 25 kV - 50 Hz configurations. The former is predominantly used in Germany, Austria, Switzerland, Norway, and Sweden, while the latter is common in England, Wales, Portugal, northern France, Denmark, Finland, and other parts of Western Europe [4].

Compared to DC systems, AC electrification offers distinct advantages, particularly the ability to operate at higher voltages. This results in reduced current levels, lower transmission losses, and decreased infrastructure and operational costs. These advantages have contributed to the growing preference for AC traction systems to meet increasing transportation demands.

6.1.1.1. DC traction electrification system

In DC railway systems, traction power is derived from a three-phase AC distribution network at medium or high voltage and subsequently converted to DC through rectifiers housed within traction power substations (TPSs). A typical TPSS architecture is depicted in Fig. 2.

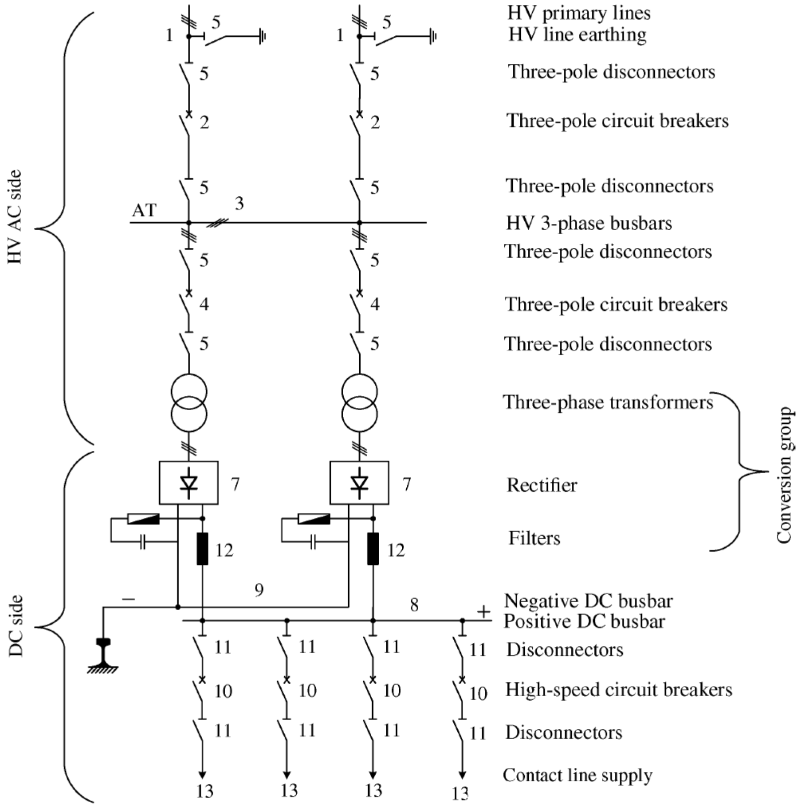

Fig. 2. A typical railway TPS architecture in the DC electrification system

The AC section of a TPS contains control gear, protection mechanisms, and measurement equipment for grid connection and power conversion. The DC section comprises rectifiers, line filters, and additional control and protection components for the traction network [1].

Diode-based rectifiers are the preferred choice in DC TPSs due to their simplicity and reliability. However, their lack of control mechanisms limits voltage regulation, power flow management, and regenerative braking energy recovery. To address these shortcomings, thyristor-based inverters operating in parallel with diode rectifiers, or voltage source converters (VSCs) based on gate turn-off thyristors (GTOs) or insulated gate bipolar transistors (IGBTs), are introduced [4].

Voltage drops in DC traction networks are governed by the resistive properties of power supply lines. These can be mitigated by bilateral power supply configurations on double-track lines [1]. A key drawback of DC systems is stray current, which leaks from rails into the ground and, if not properly managed, returns to the substation via the earth mat or nearby rail segments. This phenomenon can induce electrolytic corrosion, potentially damaging underground gas pipelines and reinforcing steel structures in civil engineering projects [4].

6.1.1.2. AC traction electrification system

To facilitate higher voltage operation while minimizing current demand, AC electrification has become the predominant choice for modern railway systems.

Historically, a three-phase electrification system was implemented in northern Italy, utilizing two parallel overhead wires and running rails for power transmission. However, this system was decommissioned in the late 1960s due to the complexities associated with double-pantograph current collection and the need for intricate phase-changing apparatus on traction units [4]. Presently, single-phase AC systems are universally employed, enabling simpler single-wire overhead line configurations.

In a 25 kV - 50 Hz traction system, power is supplied from a three-phase high-voltage industrial network via transformers, as illustrated in Fig. 3. To minimize voltage imbalance in the three-phase grid, TPSS transformers are strategically connected to alternating phase pairs (e.g., RS, ST, TR in Fig. 3) [5].

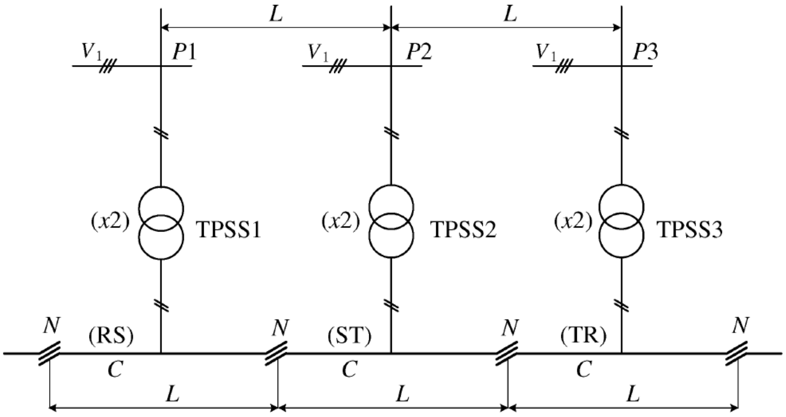

Fig. 3. Single-phase AC power supply for 25 kV – 50 Hz system

For 15 kV - 16⅔ Hz (16.7 Hz) systems, two primary power supply configurations exist: one is centralized distribution system, and another is distributed conversion system. A high-voltage line network equipped with single-phase transformers supplies TPSs along the railway. This network is powered by dedicated power plants (hydroelectric or thermoelectric) or by industrial three-phase networks via rotary frequency converters (RFCs) or static frequency converters (SFCs), as depicted in Fig. 4. In Germany, Switzerland, and Austria, synchronous generators or RFCs modify the nominal frequency from 16⅔ Hz to 16.7 Hz to prevent synchronization issues with the 50 Hz grid [1]. Here, TPSs are directly linked to the industrial grid, performing both voltage transformation and frequency conversion in a single stage (Fig. 5).

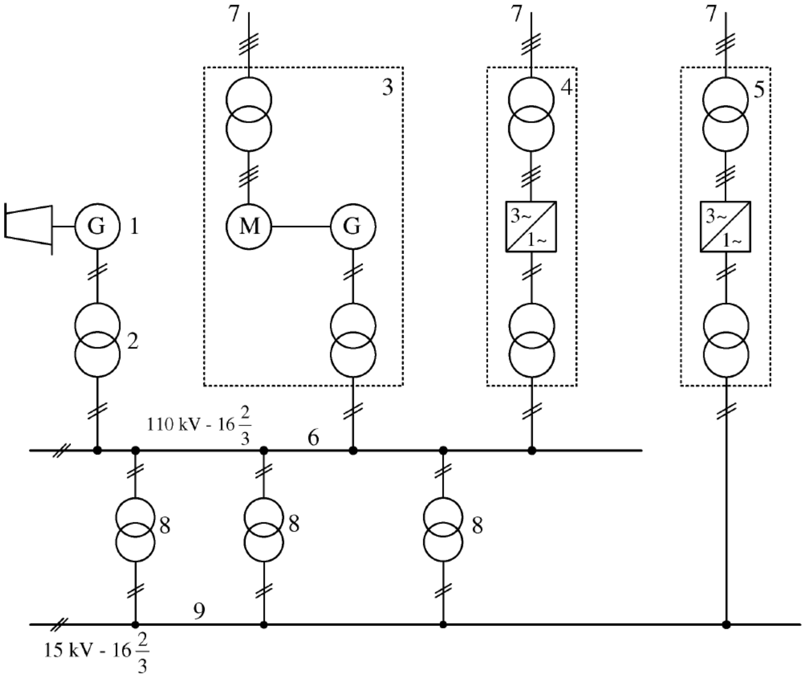

Fig. 4. Single-phase AC system at 16⅔ Hz (16.7 Hz) with centralized distribution

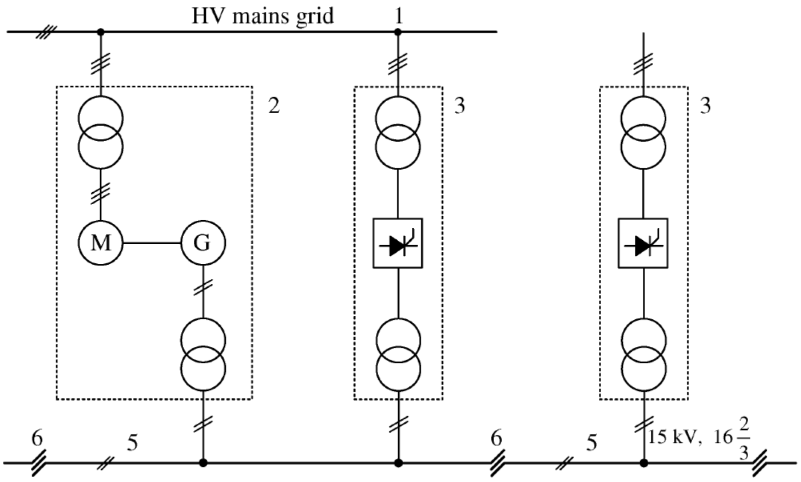

Fig. 5. Single-phase AC system at 16⅔ Hz (16.7 Hz) with distributed conversion

A significant advantage of AC traction is regenerative braking, wherein braking energy is preferentially consumed by other trains drawing power from the same network. If immediate consumption is not possible, regenerative energy may be fed back into the industrial grid via transformers or SFCs [6]. However, grid stability considerations may restrict reverse power flow, particularly in 50 Hz networks, where train regeneration is sometimes prohibited. Conversely, in 16.7 Hz networks, regenerative energy is actively managed by SFCs, with surplus energy dissipated as thermal energy via braking resistors when necessary.

Stray currents, though present in AC systems, generally do not cause electrolytic corrosion due to the alternating nature of the current [4]. Strategies to mitigate stray currents include:

- Booster Transformer (BT) Scheme: A return conductor, installed at elevated positions, is connected in series with booster transformer secondary windings to counteract stray currents (Fig. 6).
- Autotransformer (AT) Scheme: This approach, shown in Fig. 7, halves the current, reduces voltage drop, and directs return current through an auxiliary feeder, mitigating stray current effects [1], [5].

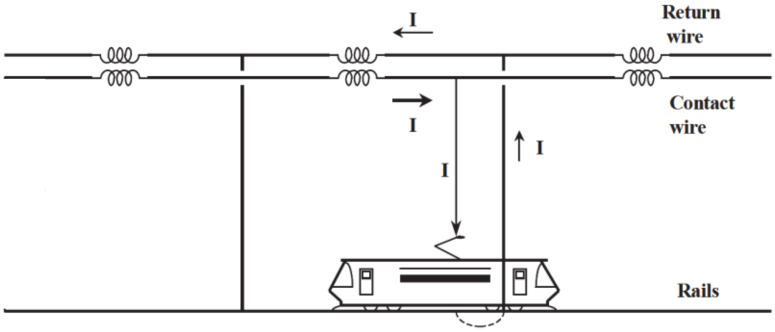

Fig. 6. Booster transformer scheme

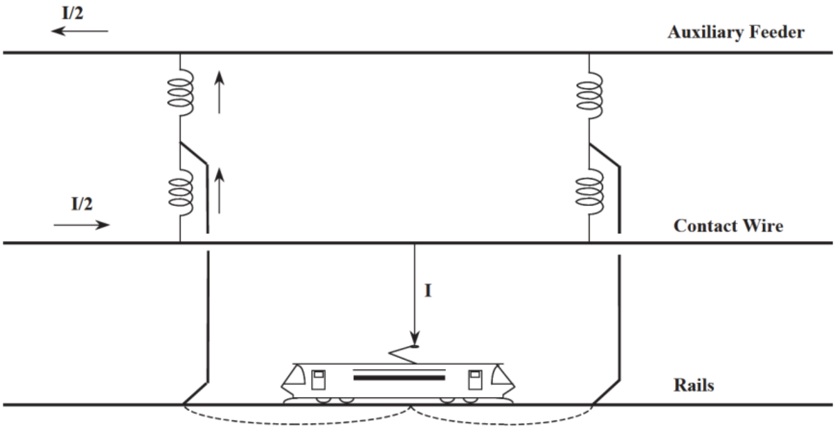

Fig. 7. Autotransformer scheme

Additionally, in 50 Hz systems, V-V and Scott-transformer configurations are employed for three-phase to two-phase conversion to improve grid balance, as depicted in Fig. 8 [7].

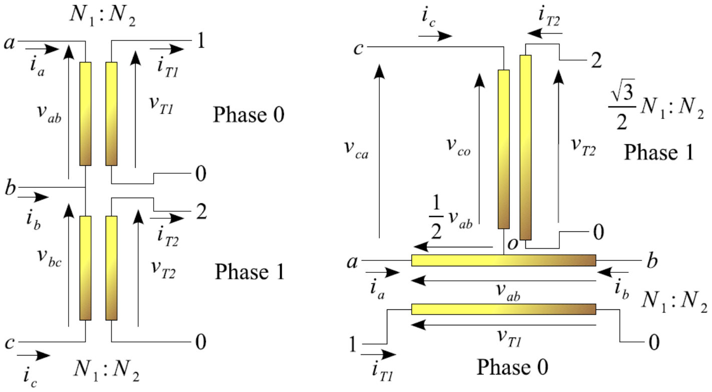

(a) (b)

Fig. 8. Traction transformer used in 50 Hz system. (a) V-V configuration. (b) Scott configuration.

6.1.2. Swedish railway power supply system

Sweden’s railway system operates on a single-phase, 16⅔ Hz, 15 kV AC electrification system, supplied by the national 50 Hz power grid. Unlike some countries that rely on dedicated power plants for railway traction, Sweden utilizes a distributed conversion system, where power is drawn from the national grid and converted to the required frequency and voltage using converter substations. This approach has shaped the evolution of Sweden’s railway electrification, integrating both historical and modern technologies to ensure a reliable power supply.

6.1.2.1. System development and architecture

The electrification of Sweden’s railway network began in the early 20th century with the 15 Hz system used for iron ore transportation in the north, powered by the Porjus hydropower plant. This system employed 80 kV transmission lines and 80/15 kV transformers along the railway. In the mid-1920s, the railway line between Stockholm and Gothenburg was electrified using RFCs, which enabled direct power conversion from the three-phase industrial network to the single-phase railway system. This marked the transition towards a distributed conversion system, which remains the foundation of Sweden’s railway electrification [8].

To enhance the power supply for heavy freight transport, a 132 kV transmission line was constructed in 1985, extending from Hallsberg to Jörn. This development introduced elements of a centralized distribution system, similar to those found in Germany and Switzerland. More recently, additional 132 kV transmission lines have been installed in central Sweden to strengthen the traction power system, though expansion in the southern regions has been limited due to the challenges associated with constructing new overhead lines [9].

The Swedish railway power supply system is presented in Fig. 9, which consists of:

- Overhead catenary system (OCS), which provides the primary 16⅔ Hz, 15 kV AC power supply to trains.
- High-voltage (HV) feeder line (132 kV Line), which is a 2×66 kV, 16⅔ Hz system designed to reduce the power flow on the catenary and minimize the number of supply stations.
- Converter substations, which facilities that convert three-phase, 50 Hz electricity from the national grid into single-phase, 16⅔ Hz power for railway traction. These substations are typically spaced 60-90 km apart.
- Transformer stations, which is located approximately every 40-50 km. These stations step up the voltage from 15 kV to 132 kV for transmission along the HV feeder line.

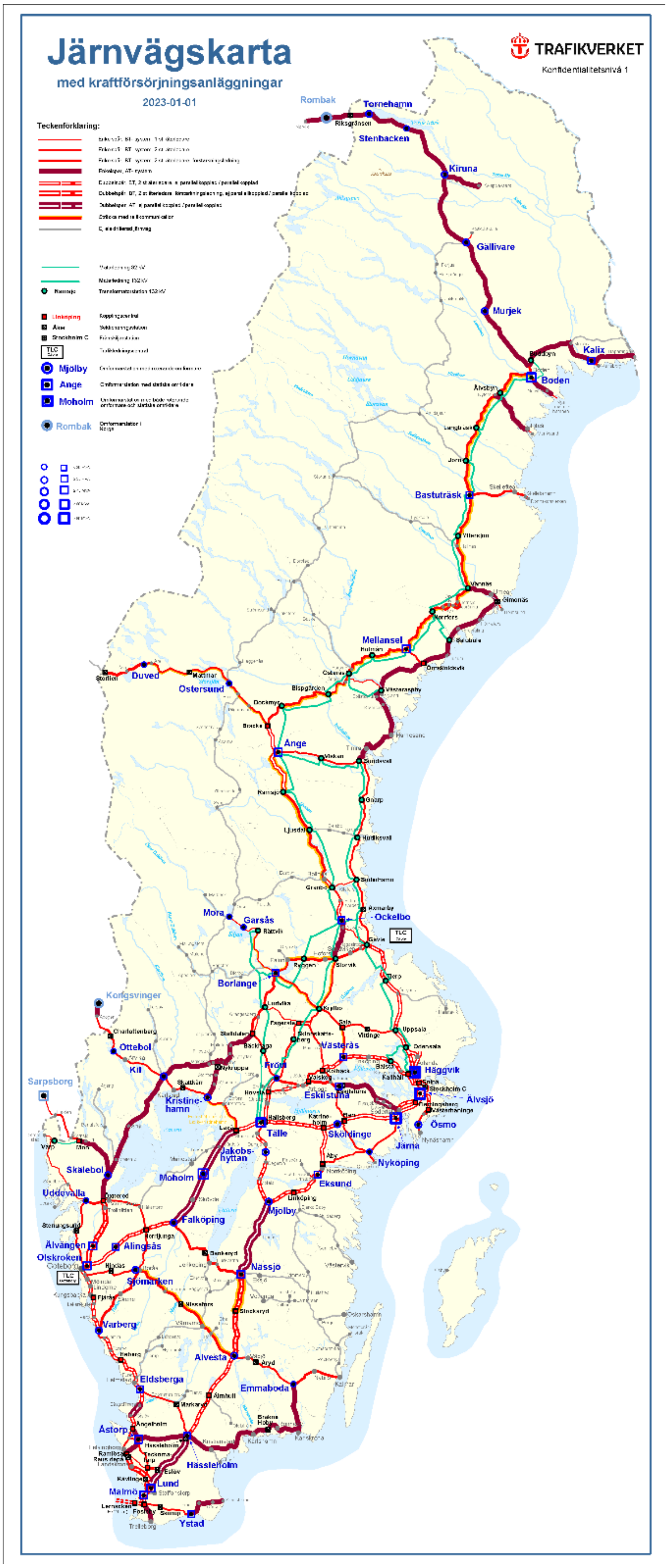
Järnvägskarta
med kraftförsörjningsanläggningar
2023-01-01
TRAFIKVERKET
Konfidentialitetsnivå 1
Teckenforklaring:
Mjölby
Ange
Moholm
Rombak
Torneh amn
Riksgränsen
Stenbacken
Kiruna
Gällivare
Murjek
Boden
Kalix
Älvsbyn
Jörn
Bastuträsk
Vännäs
Mellansel
Storlien
Duved
Östersund
Bispgården
Ånge
Ljusdal
Mora
Garsås
Ockelbo
Borlänge
Kongsvinger
Charlottenberg
Ottebol
Kil
Sarpsborg
Kristinehamn
Västerås
Frövi
Häggvik
Eskilstuna
Älvsjö
Tälle
Sköldinge
Ösmo
Järna
Nyköping
Skälebol
Uddevalla
Jakobshyttan
Moholm
Eksund
Mjölby
Falköping
Älvängen
Alingsås
Olskroken
Nässjö
Sjömarken
Varberg
Alvesta
Eldsberga
Emmaboda
Åstorp
Hässleholm
Lund
Malmö
Ystad
Uppsala
Stockholm C
Trelleborg

Fig. 9. The Swedish railway power supply system

6.1.2.2. Frequency converters

Historically, power conversion for Sweden's railway system relied on RFCs, which use a motor-generator arrangement to convert three-phase, 50 Hz power into single-phase, 16⅔ Hz electricity. Despite their effectiveness, RFCs have significant drawbacks, including high maintenance requirements, lower efficiency, and limited scalability. Consequently, RFCs are being progressively replaced by SFCs, which offer higher efficiency, reduced maintenance costs, and improved power quality [10][11].

Currently, three types of SFCs are utilized in Sweden: cyclo-converters, DC-link converters, and multilevel converters. The cyclo-converters consist of two double thyristor bridges connected in series. This converter has a robust construction, a higher efficiency compared to RFC and can feed regenerative energy back into the grid. However, the low overload capability and the severe harmonics in the output voltage which place high demands on the filters and may have an impact on the catenaries, are the main drawback. The DC-link converters consist of two parts, a three-phase twelve-pulse rectifier and a single-phase PWM inverter. The rectifier converts three-phase, 50 Hz AC input power to DC, and then the inverter converts this electrical DC power to single-phase, 16⅔ Hz (16.7 Hz) AC power for the traction system. Such SFC is the most common one in the Swedish rail power supply system due to its high efficiency, up to 97% - 98%, and the harmless influences on the single-phase and three-phase networks. Except for some older models of DC-link converter, most DC-link converters can return regenerated power to the grid. Nowadays, new design solution for SFC that consists of a cyclo-converter with several serial connected H-bridge modules, called multilevel converter. It has very high efficiency, up to 98.5%, negligible harmonics in the output voltage, and redundant design with fault tolerance. Moreover, since there is no need for transformer and filters on the three-phase side and there are lighter requirements for filters on the single-phase side, this converter can save much space.

As of 2022, SFCs provided a total power capacity of 1143 MVA, exceeding the capacity of RFCs by approximately 110%, a trend expected to continue with further advancements in power electronics and control systems [6].

6.1.2.3. Electrical locomotives in Sweden

The type of locomotive used in an electrified railway system significantly influences power quality and system efficiency. Sweden's older RC-type locomotives, which utilize thyristor-based rectifiers to supply power to DC traction motors, exhibit several disadvantages, including low power factor, increased energy losses, and substantial harmonic emissions. These factors contribute to higher system losses and reduced power transfer efficiency.

In contrast, modern voltage source inverter (VSI) locomotives, which employ pulse-width modulation (PWM) converters, offer superior performance, including higher efficiency, improved power factor, and the ability to return regenerative energy to the grid. The transition to VSI locomotives aligns with the broader modernization of Sweden's railway power infrastructure, further enhancing system stability and sustainability.

The Swedish railway power supply system has undergone significant transformations, transitioning from localized RFC-based conversion to a combination of decentralized and centralized power distribution. The increasing adoption of HV feeder lines, modern SFCs, and advanced locomotive technologies has led to enhanced efficiency, reliability, and sustainability. As Sweden continues to expand and modernize its railway network, further innovations in power electronics, energy storage, and smart grid integration will play a crucial role in shaping the future of railway electrification.

6.1.3. Simulation models of system

To investigate the impact of the energy storage system (ESS) on the Swedish railway power supply network, this section presents the development of a simulation model for the system. As previously discussed, the railway power system primarily comprises frequency converters, transmission lines, and locomotives. Given both the current operational framework and anticipated technological advancements, the simulation focuses on DC-link converters and multilevel converters, reflecting the predominant and emerging conversion technologies. Additionally, the model incorporates thyristor rectifier-based RC-type locomotives, which represent legacy traction systems, alongside modern locomotives employing fully controlled VSIs to capture the evolving landscape of railway traction.

6.1.3.1. Static frequency converters

6.1.3.1.1. DC-link converter

The DC-link converter is a type of frequency converter in which frequency transformation is achieved through a 50 Hz rectifier bridge and a 16⅔ Hz inverter, interconnected via a DC-link. In earlier installations, such as the YRLA, TGTO, Megamacs, SFC1, and SFC2 models, the 50 Hz rectifier is typically implemented using a three-phase 12-pulse rectifier. However, in more recent systems, such as the PCS model, the rectifier is based on integrated gate-commutated thyristors (IGCTs), enabling the regeneration of braking energy back to the national grid.

The PWM inverter in these converters can be implemented using either a two-level bridge, as seen in the YRLA, TGTO, and Megamacs models, or a three-level bridge, as used in the SFC1, SFC2, and PCS models, where multiple voltage levels are synthesized through a single-phase transformer. The latter configuration offers superior power quality due to its ability to generate a higher number of voltage levels, thereby reducing harmonic distortion. Additionally, with the exception of the YRLA-type inverters, which employ thyristors, all other models utilize fully controlled switching devices, such as GTOs and IGCTs, enhancing efficiency and controllability.

A simulation model of a typical DC-link converter has been developed in MATLAB/Simulink, with the power stage schematic illustrated in Fig. 10. This model employs a three-phase 12-pulse rectifier as a representative example, incorporating a three-phase Y-Y/D1 transformer characterized by its rated power (S_{rec}), turn ratio (k_{rec}), leakage impedance (Z_{lrec}), and magnetization impedance (Z_{mrec}). The rectifier stage consists of two thyristor-based three-phase bridges, ensuring efficient AC-DC conversion.

The DC-link serves as an intermediate energy storage stage, comprising an equivalent capacitor (C_{dc}) to stabilize the DC voltage, along with a resonant filter (C_{n0}, L_{n0}, R_{n0}) designed to mitigate second-harmonic (33⅓ Hz) fluctuations originating from the railway traction system. Additionally, an over-voltage limiter consisting of a transistor (Q) and a resistor (R_{ov}) is implemented to protect the system from voltage surges.

For the inverter stage, a two-level PWM inverter is selected due to its representative nature in practical railway applications. This inverter comprises multiple GTO-based H-bridge modules, which are parallel-connected at their DC terminals and series-connected at their AC terminals via a single-phase transformer. The transformer is characterized by its rated power (S_{inv}), turn ratio (k_{inv}), leakage impedance (Z_{linv}), and magnetization impedance (Z_{minv}). To ensure high power quality, a resonant filter (C_{n1}, L_{n1}, R_{n1}) is incorporated to suppress high-frequency harmonics induced by inverter switching actions, while an output inductor (L_{f}) is included to attenuate low-frequency harmonics from both the railway traction system and the inverter itself at the single-phase output terminal.

The simulation model also defines key electrical parameters to facilitate explanation. The three-phase voltages and currents are denoted as v_{sabc} and i_{sabc}, respectively, while the DC-link voltage is represented as v_{dc}. At the single-phase output terminal, the voltage and current are expressed as v_{o} and i_{o}, respectively. The positive directions of these variables are clearly indicated in Fig. 10, ensuring consistency in the interpretation of simulation results.

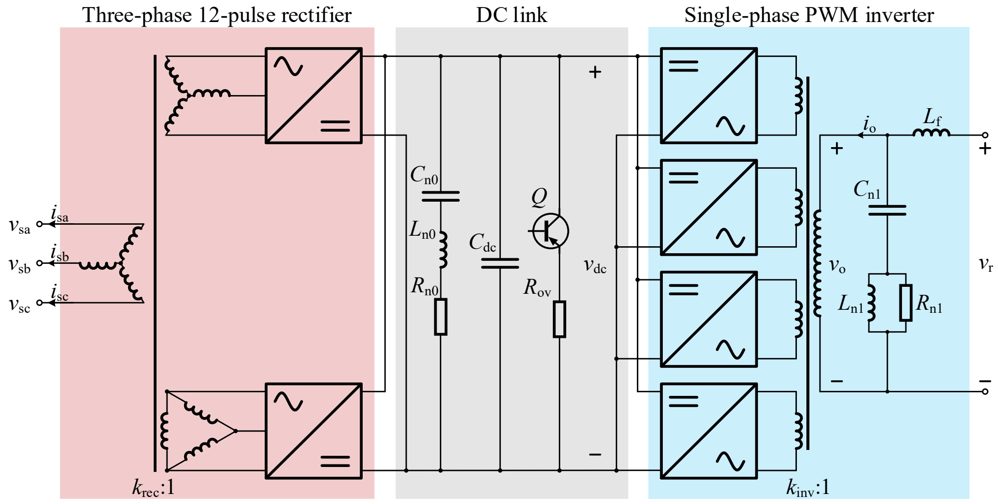

Fig. 10. Power stage schematic of typical DC-link converter in simulation model

In general, the SFC is required to provide a continuous power transfer from the 50 Hz national grid to the 16⅔ Hz railway power supply system. The operational behavior of SFCs is designed to emulate that of RFCs by utilizing the phase angle of the output voltage to regulate active power flow. Consequently, for DC-link converters that are not designed to recover regenerative braking energy, the load angle characteristic employed in the simulation model is illustrated in Fig. 11.

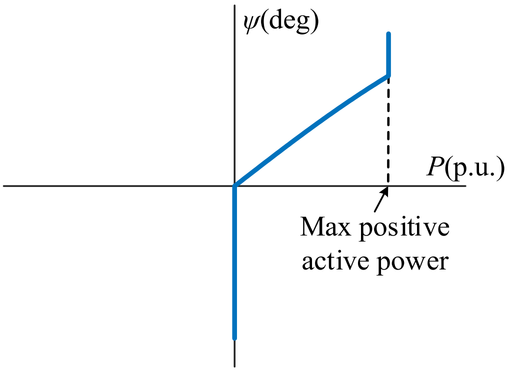

Fig. 11. Load angle characteristics for preventing negative power supply

Building upon the operational requirements of the DC-link converter, the control scheme implemented in the simulation model is depicted in Fig. 12. This control framework is structured into two primary components: the 12-pulse rectifier control and the PWM inverter control.

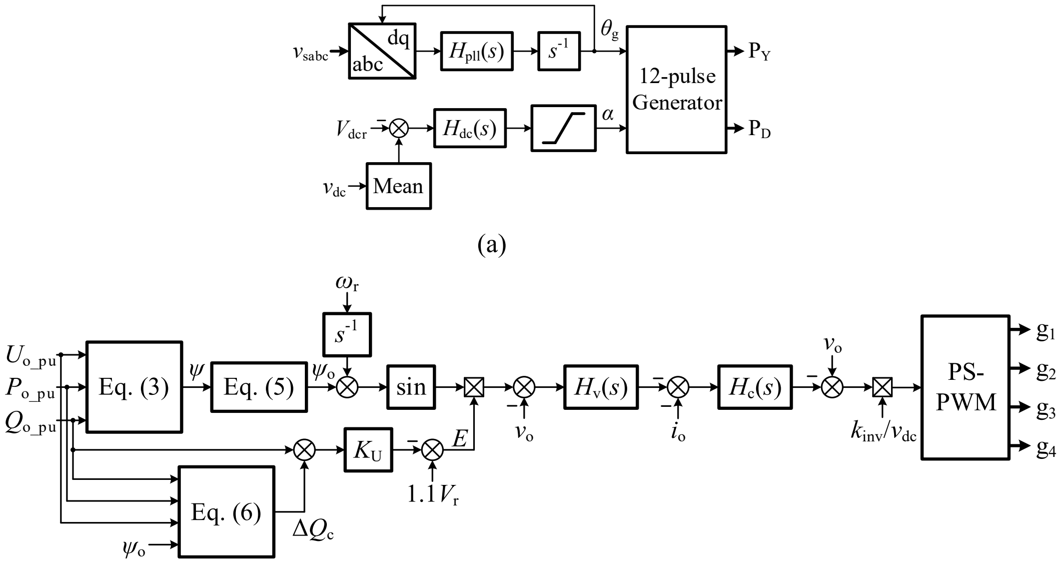

(a)

(b)

Fig. 12. Control scheme of dc-link converter: (a) 12-pulse rectifier control, and (b) PWM inverter control

As illustrated in Fig. 12 (a), the three-phase 12-pulse rectifier control is primarily responsible for maintaining DC-link voltage stability. The nominal DC-link voltage, denoted as V_{dcr}, is regulated through a proportional-integral (PI) controller, denoted as $H_{\mathrm{dc}}(s)$, which comprises a proportional gain (K_{dcp}) and an integral gain (K_{dci}). To prevent the regenerative braking energy from being fed back into the national grid, a saturation limit is imposed on the thyristor firing angle (α), restricting it to the range of 0° to 90°. Additionally, a phase-locked loop (PLL) is employed to extract the grid phase angle (θ_{g}), which serves as the reference for 12-pulse drive generation. The PLL is regulated by $H_{\mathrm{PLL}}(s)$, a PI controller characterized by proportional gain (K_{pllp}) and integral gain (K_{plli}).

The single-phase PWM inverter control, shown in Fig. 12 (b), is designed to enable the converter to provide voltage and frequency support to the railway traction system. This is accomplished through a nested control structure, incorporating current, voltage, and power control loops. The current controller employs a multiple quasi-proportional-resonance (PR) regulator for tracking the fundamental component as well as mitigating the significant third and fifth harmonic component, mathematically expressed as

$$H_{\mathrm{c}}(s) = K_{\mathrm{cp}} + \sum_{n=1,3,5} \frac{2K_{\mathrm{cr}n}\omega_{\mathrm{cb}}s}{s^2 + 2\omega_{\mathrm{cb}}s + (n\omega_{\mathrm{r}})^2} \tag{1}$$

where K_{cp} is the proportional gain for current control, while $K_{\mathrm{cr}n}$ represents the resonant gain of quasi-PR regulator for the n-th harmonic component. The parameters ω_{cb} corresponds to the bandwidth angular frequencies of quasi-PRs for current control, and ω_{r} denotes the resonant angular frequency, which is $2\pi \times 16⅔$ rad/s.

The voltage controller employs a cascaded multiple quasi-PR controller with an additional lead compensation term, mathematically expressed as

$$H_{\mathrm{v}}(s)=(K_{\mathrm{vp}}+\sum_{n=1,3,5}\frac{2K_{\mathrm{v r}n}\omega_{\mathrm{vb}}s}{s^2+2\omega_{\mathrm{vb}}s+(n\omega_{\mathrm{r}})^2})\times\frac{\omega_{\mathrm{p}}}{\omega_{\mathrm{z}}}\frac{s+\omega_{\mathrm{z}}}{s+\omega_{\mathrm{p}}} \tag{2}$$

where K_{vp} and $K_{\mathrm{vr}n}$ denote the proportional gain and the resonant gain of quasi-PR regulator for the n-th harmonic component, respectively, while ω_{vb} corresponds to the bandwidth angular frequency of quasi-PR regulator for the voltage control. The additional parameters ω_{z} and ω_{p} represent the zero and pole angular frequencies, respectively.

The active power control is based on the load angle (ψ), which is formulated as

$$\psi=-\frac{1}{3}\arctan(X_{\mathrm{q}}^{\mathrm{m}}P_{\mathrm{o\_pu}})-\arctan(\frac{X_{\mathrm{q}}^{\mathrm{g}}P_{\mathrm{o\_pu}}}{U_{\mathrm{o\_pu}}{}^2+X_{\mathrm{q}}^{\mathrm{g}}Q_{\mathrm{o\_pu}}}) \tag{3}$$

where $X_{\mathrm{q}}^{\mathrm{m}}$ and $X_{\mathrm{q}}^{\mathrm{g}}$ denote the quadrature reactance of the motor and generator, respectively, while $P_{\mathrm{o\_pu}}$ and $Q_{\mathrm{o\_pu}}$ represent the per-unit active and reactive power output, and $U_{\mathrm{o\_pu}}$ corresponds to the per-unit root mean square (RMS) value of voltage at the output terminal. This formulation enables the DC-link converter to emulate the characteristics of RFCs by adjusting active power output through load angle modulation.

Furthermore, a Q-V droop control is introduced to regulate voltage magnitude, expressed as

$$E=\ 1.1V_r-K_{\mathrm{U}}Q_{\mathrm{o\_pu}} \tag{4}$$

where V_{r} represents the nominal peak voltage, which is usually regulated at 1.1 per unit (p.u.) to ensure compatibility with railway traction loads, and K_{U} is the droop coefficient. This mechanism ensures that the voltage magnitude dynamically adjusts in response to reactive power variations, thereby improving stability and power-sharing coordination in the railway traction network.

To prevent the recovery of regenerative braking energy, a constraint is imposed on ψ, ensuring it does not fall below a predefined minimum value (ψ_{min}). When the active power (P_{o}) fluctuates around zero, ψ transitions between ψ_{min} and its nominal value, leading to abrupt phase angle variations that can induce power oscillations. To mitigate these sudden changes, a smoothing function is introduced, allowing a gradual transition from the original value of ψ to ψ_{min} as P_{o} crosses from positive to negative. It is important to note that the sign of P_{o} depends on the direction of current flow. In the simulation model, the DC-link converter is designed such that it outputs negative active power and absorbs positive active power. This regulation is formulated as

$$\psi_{\mathrm{o}}=\ \psi+\frac{(\psi_{\mathrm{min}}-\psi)}{1+e^{-\gamma P_{\mathrm{o\_pu}}}} \tag{5}$$

where γ is used to control the steepness of the transition.

Moreover, to enforce the maximum power constraints illustrated in Fig. 11, an additional reactive power compensation term ΔQ_{c} is introduced within the voltage-reactive power droop control. This adjustment enables further regulation of voltage magnitude E when the load angle reaches its maximum permissible value (ψ_{max}). The modified voltage control equation is expressed as

$$\Delta Q_{\mathrm{c}}=\begin{cases}K_{\mathrm{Qc}}(\psi-\psi_{\mathrm{max}}), & P_{\mathrm{o\_pu}}\le -1\\ 0, & P_{\mathrm{o\_pu}}>-1\end{cases} \tag{6}$$

where K_{Qc} is a gain coefficient, and ψ_{max} is determined by

$$\psi_{\max} = -\frac{1}{3}\arctan(-X_{\mathrm{q}}^{\mathrm{m}}) - \arctan\left(\frac{-X_{\mathrm{q}}^{\mathrm{g}}}{U_{\mathrm{o\_pu}}{}^{2} + X_{\mathrm{q}}^{\mathrm{g}} Q_{\mathrm{o\_pu}}}\right).$$

From this formulation, it is shown that when $\psi > \psi_{\max}$, the system actively reduces the output voltage amplitude and locks the active power P_{o} at its maximum permissible value by dynamically adjusting reactive power compensation.

6.1.3.1.2. Multilevel converter

Unlike the DC-link converter, the multilevel converter enables direct 50 Hz AC to 16⅔ Hz AC conversion without the need for an intermediate DC link. This topology consists of three upper arms and three lower arms, each comprising multiple series-connected submodules. The common connection point of the upper and lower arms is linked to the single-phase railway traction system, while the midpoints of the three arms are connected to the three-phase national grid. To achieve direct frequency conversion, full-bridge submodules with IGBTs are employed, allowing for the generation of bipolar arm voltages, which are essential for ensuring stable and efficient operation.

A simulation model of a multilevel converter (PLUS model) has been developed in MATLAB/Simulink, with its power stage schematic depicted in Fig. 13. Each arm of the converter consists of five submodules and an arm inductor (L) in series with a resistor (R). Moreover, each submodule incorporates a capacitor (C_{m}) To maintain high power quality, an output filtering inductor (L_{s}) is included at the single-phase output terminal to mitigate low-frequency harmonics originating from both the railway traction system and the inverter itself. Additionally, a resonant filter (C_{n}, L_{n}, R_{n}) is implemented to suppress high-frequency harmonics induced by inverter switching operations.

To ensure clarity in the analysis, the simulation model explicitly defines key electrical parameters. The three-phase voltages and currents are denoted as v_{sabc} and i_{sabc}, respectively. The capacitor voltage of each submodule is represented as $v_{\mathrm{c}xyz}$, where $x = \mathrm{u}, \mathrm{l}$ (indicating upper and lower arms), $y = \mathrm{a}, \mathrm{b}, \mathrm{c}$ (indicating three phases) and $z = 1, \ldots, 5$ (indicating individual submodules). At the single-phase output terminal, the voltage and current are expressed as v_{r} and i_{r}, respectively. The positive directions of these variables are clearly specified in Fig. 13, ensuring consistency in the interpretation of simulation results.

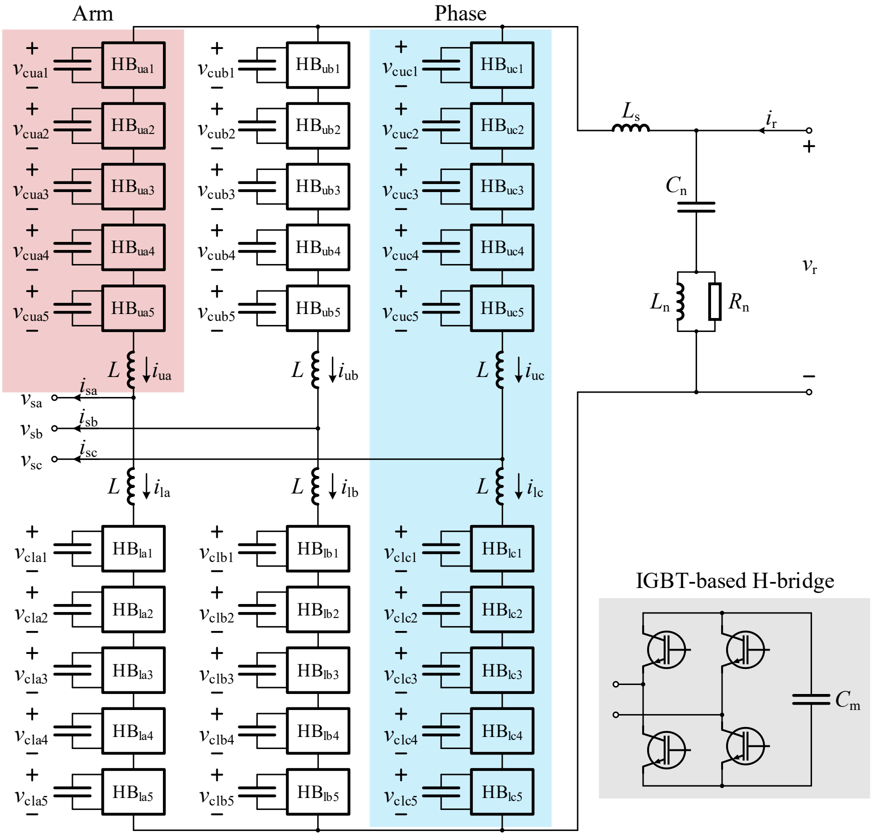

Fig. 13. Power stage schematic of multilevel converter in simulation model

The multilevel converters can be used to recover regenerative braking energy, and its load angle characteristic employed in the simulation model is illustrated in Fig. 14.

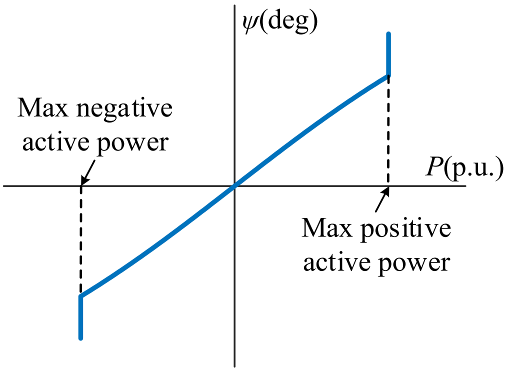

Fig. 14. Load angle characteristics for bidirectional power supply

Based on the operational requirements of the multilevel converter, the control scheme implemented in the simulation model comprises three interrelated components: the control of the three-phase side, the control of the single-phase side, and the module voltage balancing. The detailed structure of this control framework is illustrated in Fig. 15.

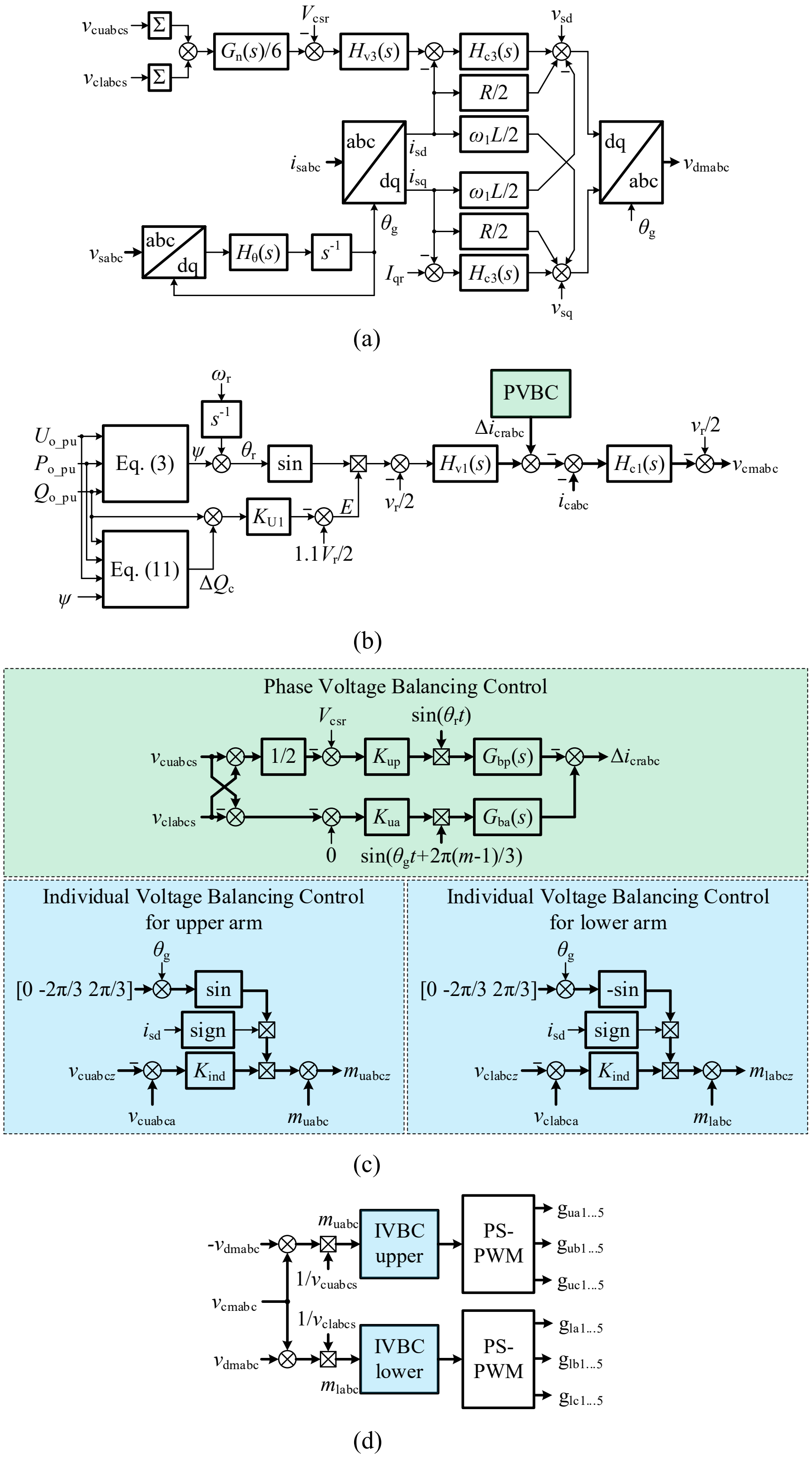

(a)

(b)

(c)

(d)

Fig. 15. Control scheme of multilevel converter: (a) three-phase side control, (b) single-phase side control, and (c) module voltage balancing control; (d) modulation signal synthesis

On the three-phase side control, the primary objective is to manage power exchange between the three-phase grid and the single-phase railway traction system. This is accomplished through a PI regulator-based dq-frame current control in conjunction with a global module capacitor voltage regulation strategy. The total capacitor voltage across the modules of each arm, denoted as v_{cxy} with x = u, l and y = a, b, c, is regulated to follow the reference value V_{csr} using PI regulator $H_{\mathrm{v3}}(s)$, defined by a proportional gain (K_{v3p}) and an integral gain (K_{v3i}). The output of $H_{\mathrm{v3}}(s)$ is served as the reference current in the d-axis, while the reference current in the q-axis is set to I_{qr}. The variables v_{sdq} and i_{sdq} are the three-phase currents and voltages transformed into the dq-frame, where the latter is regulated using PI controller, $H_{\mathrm{c3}}(s)$, defined by a proportional gain (K_{c3p}) and an integral gain (K_{c3i}). To mitigate the influence of the common-mode zero-sequence voltage components at twice the fundamental frequency ($2\omega_{\mathrm{r}}$), a notch filter is incorporated into the global module capacitor voltage control and formulated as

$$G_{\mathrm{n}}(s) = \frac{s^2 + (2\omega_{\mathrm{r}})^2}{s^2 + \alpha_{\mathrm{n}} s + (2\omega_{\mathrm{r}})^2} \tag{7}$$

where α_{n} is the damping factor.

Furthermore, to maintain synchronization with the grid, a phase-locked loop (PLL) extracts the phase angle (θ_{g}), which is regulated by a PI controller $H_{\theta}(s)$ with proportional and integral gains $K_{\theta\mathrm{p}}$ and $K_{\theta\mathrm{i}}$, respectively.

On the single-phase side, the multilevel converter provides voltage and frequency support to the railway traction system. This regulation is achieved through a hierarchical control structure that involves current, voltage, and power loops, analogous to those applied in a DC-link converter. The circulating currents among three phases, denoted as i_{cy} for y = a, b, c, are determined by the expression $i_{cy} = (i_{uy} + i_{ly})/2$ and are regulated through a multiple quasi-PR controller, expressed as

$$H_{\mathrm{c1}}(s) = K_{\mathrm{c1p}} + \sum_{n=1,3,5} \frac{2K_{\mathrm{c1}rn}\omega_{\mathrm{c1b}} s}{s^2 + 2\omega_{\mathrm{c1b}} s + (n\omega_{\mathrm{r}})^2} \tag{8}$$

where K_{c1p} and K_{c1r} represent the proportional and resonant gains, respectively, and ω_{c1b} corresponds to the bandwidth angular frequency of quasi-PR regulator for circulating current control. Similar to the voltage control strategy implemented in the DC-link converter, the voltage regulation mechanism in this case also employs a cascaded multiple quasi-PR controller with an additional lead compensation term, mathematically expressed as

$$H_{\mathrm{v1}}(s) = (K_{\mathrm{v1p}} + \sum_{n=1,3,5} \frac{2K_{\mathrm{v1}rn}\omega_{\mathrm{v1b}} s}{s^2 + 2\omega_{\mathrm{v1b}} s + (n\omega_{\mathrm{r}})^2}) \times \frac{\omega_{\mathrm{p1}}}{\omega_{\mathrm{z1}}} \frac{s + \omega_{\mathrm{z1}}}{s + \omega_{\mathrm{p1}}} \tag{9}$$

where K_{v1p} and K_{v1r} denote the proportional gain and the resonant gain of quasi-PR regulator for the n-th harmonic component, respectively, while ω_{v1b} corresponds to the bandwidth angular frequency of quasi-PR regulator for the voltage control. The additional parameters ω_{z1} and ω_{p1} represent the zero and pole angular frequencies, respectively.

Moreover, the voltage-reactive power droop control is modified to be

$$E = 1.1\frac{V_r}{2} - K_{\mathrm{U1}} Q_{\mathrm{o\_pu}} \tag{10}$$

where K_{U1} represents the droop coefficient. To enforce the upper and lower power constraints dictated by the load angle characteristics, the reactive power compensation term is refined as

$$\Delta Q_{\mathrm{c}} = \begin{cases} K_{\mathrm{Qc1}}\left(\psi - \psi_{\max}\right), & P_{\mathrm{o\_pu}} \le -1 \\ 0, & -1 < P_{\mathrm{o\_pu}} < 1 \\ -K_{\mathrm{Qc1}}\left(\psi - \psi_{\max}\right), & P_{\mathrm{o\_pu}} \ge 1 \end{cases} \tag{11}$$

where K_{Qc1} denotes the gain coefficient, and the maximum load angle $\psi_{\max}$ is determined by

$$\psi_{\max} = \begin{cases} -\dfrac{1}{3}\arctan(-X_{\mathrm{q}}^{\mathrm{m}}) - \arctan\left(\dfrac{-X_{\mathrm{q}}^{\mathrm{g}}}{U_{\mathrm{o\_pu}}{}^{2} + X_{\mathrm{q}}^{\mathrm{g}} Q_{\mathrm{o\_pu}}}\right), & P_{\mathrm{o\_pu}} \le -1 \\ -\dfrac{1}{3}\arctan(X_{\mathrm{q}}^{\mathrm{m}}) - \arctan\left(\dfrac{X_{\mathrm{q}}^{\mathrm{g}}}{U_{\mathrm{o\_pu}}{}^{2} + X_{\mathrm{q}}^{\mathrm{g}} Q_{\mathrm{o\_pu}}}\right), & P_{\mathrm{o\_pu}} \ge 1 \end{cases} .$$

A module voltage balancing control strategy is incorporated to address imbalances in capacitor voltages, which arise due to the inherent harmonic characteristics of the multilevel converter. Such imbalances manifest both between different phases and between the upper and lower arms of each phase. To mitigate these voltage discrepancies, the phase voltage balancing control consists of two interrelated mechanisms: the first ensures that the total capacitor voltage of each phase tracks the reference value V_{csr} by appropriately adjusting the circulating current component at ω_{r}, while the second ensures that the difference between the upper and lower arm capacitor voltages remains zero by introducing a circulating current component at ω_1. The gains associated with these control loops, denoted as K_{up} and K_{ua}, respectively, play a key role in maintaining voltage stability.

To further minimize the introduction of undesired harmonics in the circulating currents, a filtering strategy is implemented using band-pass filters, allowing only the components at ω_{r} and ω_1 to pass. These filters are mathematically formulated as

$$G_{\mathrm{bp}}(s) = \frac{\alpha_{\mathrm{bp}} s}{s^2 + \alpha_{\mathrm{bp}} s + \omega_{\mathrm{r}}{}^2} \tag{12}$$

$$G_{\mathrm{ba}}(s) = \frac{\alpha_{\mathrm{ba}} s}{s^2 + \alpha_{\mathrm{ba}} s + \omega_1{}^2} \tag{13}$$

where α_{bp} and α_{ba} represent the respective damping factors. In addition to phase voltage balancing, an individual voltage balancing control strategy is developed to regulate the voltage of each submodule within an arm toward the average capacitor voltage $v_{\mathrm{c}xya}$ (x = u, l and y = a, b, c), facilitated by a proportional controller with a gain coefficient K_{ind}.

6.1.3.2. Electrical locomotives

6.1.3.2.1. Thyristor locomotive

The RC-type locomotive remains the most widely used locomotive in Sweden. This locomotive employs series-connected half-controlled thyristor bridges to rectify 16⅔ Hz AC into DC, which is then supplied to DC traction motors. Since this locomotive is its reliance solely on mechanical brakes, it lacks the capability to regenerate power back into the railway power supply system.

A simulation model of its DC motor propulsion system has been developed in MATLAB/Simulink, with the power stage schematic illustrated in Fig. 16. A major drawback of Swedish thyristor-based locomotives is their low power factor, which restricts the amount of power that can be transmitted through the catenary system. To mitigate reactive power demand, the simulation model adopts a topology consisting of two series-connected half-controlled thyristor bridges. These bridges interface with the railway traction network through a three-winding transformer, characterized by its rated power (S_{thy}), turn ratio (k_{thy}), and leakage impedance (Z_{lthy}), and magnetization impedance (Z_{mthy}). Furthermore, the DC motor is modeled as an inductor (L_{M}) in series with a variable resistor (R_{M}). The voltage at pantograph and the current drawn by the locomotive are denoted as v_{L} and i_{L}, respectively, while the terminal voltage and armature current of the DC motor are represented as u_{d1} and I_{M}, respectively. The electromotive force (EMF) of the machine is denoted by E.

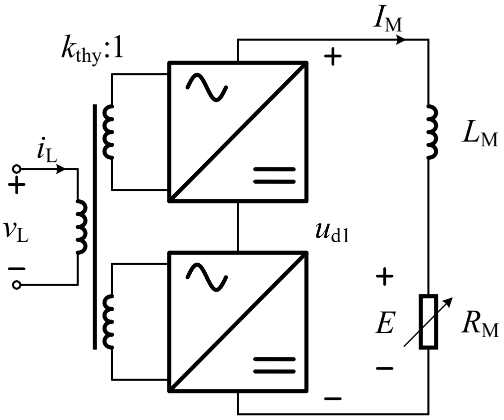

Fig. 16. Power stage schematic of thyristor locomotive in simulation model

At startup, the motors are fully magnetized. Up to a base speed v_{base}, the magnetic field remains constant at its maximum level. Beyond this threshold, field weakening is employed to maintain the machine's terminal voltage at its maximum permissible value. The relationship between machine EMF and speed for the RC-type locomotive is depicted in Fig. 17.

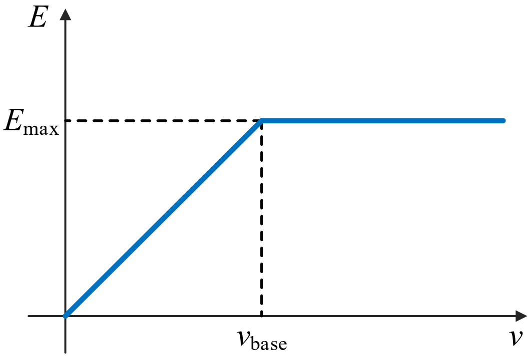

Fig. 17. Relationship between machine EMF and speed

To accurately characterize the DC motor's behavior, the value of R_{M} is determined as

$$R_{\mathrm{M}} = \frac{E^2}{P_{\mathrm{m}}} \tag{14}$$

where P_{m} represents the mechanical power at the wheels, which is given by the product of tractive effort and speed. Given that the voltage drop across L_{M} can be neglected, the primary control objective is to regulate u_{d1} to ensure compliance with the EMF-speed relationship shown in Fig. 17. This is achieved through the adjustment of the firing angles α_1 and α_2 for the respective thyristor bridges, as illustrated in Fig. 18.

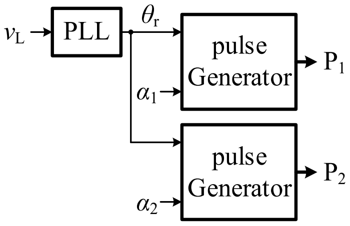

Fig. 18. Control scheme of thyristor locomotive

To synchronize with the railway traction network, a PLL extracts the phase angle (θ_r), which serves as the reference for pulse generation. At low speeds, the firing angle of the second bridge, α_2, is maintained at 180°, meaning that only the first bridge contributes to the generation of DC voltage for the motor. As the locomotive speed increases, the first bridge gradually decreases its firing angle until $\alpha_1 = 0$, at which point the second bridge begins lowering its firing angle to further increase the output voltage. However, beyond a certain speed threshold, the second bridge can no longer reduce its firing angle. This occurs either when $\alpha_1 = \alpha_2 = 0$ or when the DC motor reaches its maximum permissible terminal voltage, a condition that depends on the amplitude of the voltage at pantograph.

6.1.3.2.2. VSI locomotive

Modern locomotives in Sweden are classified as VSI locomotives. These locomotives utilize a single-phase PWM rectifier to convert the AC voltage collected at the pantograph into a nearly constant DC-link voltage. Subsequently, a three-phase PWM inverter converts this DC voltage into three-phase AC current to drive the induction motors. Unlike the RC-type locomotive, VSI locomotives possess the capability to regenerate electrical energy back into the railway power supply system.

A simulation model of the three-phase induction motor propulsion system has been developed in MATLAB/Simulink, with its power stage schematic presented in Fig. 19. The system interfaces with the railway traction network through a fully controlled H-bridge rectifier, which is coupled to the network via a transformer characterized by its rated power (S_{VSI}), turn ratio (k_{VSI}), leakage impedance (Z_{lVSI}), and magnetization impedance (Z_{mVSI}). The DC link functions as an intermediate energy storage stage, incorporating an equivalent capacitor (C_{d2}) to stabilize the DC voltage (u_{d2}) and a resonant filter (C_r, L_r, R_r) designed to attenuate second-harmonic (33⅓ Hz) fluctuations induced by the railway traction system. Furthermore, due to the decoupling effect provided by the DC link, the three-phase induction motor and its associated PWM inverter are represented in the simulation as an ideal current source, effectively characterizing the system's power consumption.

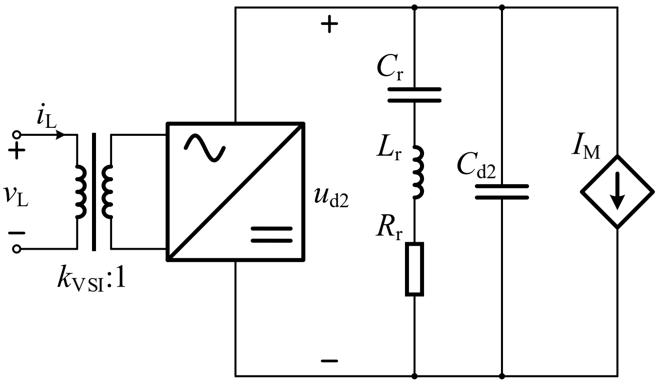

Fig. 19. Power stage schematic of VSI locomotive in simulation model

A key advantage of VSI locomotives lies in their ability to maintain an input power factor close to unity, facilitated by the full control of the rectifier bridge. The detailed control framework governing this functionality is illustrated in Fig. 20.

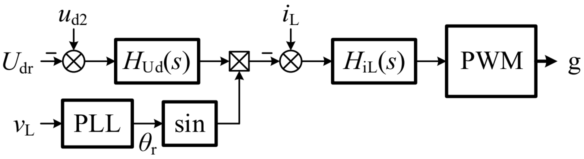

Fig. 20. Control scheme of VSI locomotive

As shown in Fig. 20, the regulation of the DC-link voltage is achieved through a PI controller, denoted as $H_{Ud}(s)$, which consists of a proportional gain (K_{Udp}) and an integral gain (K_{Udi}). This controller ensures that the DC-link voltage remains at its reference value (U_{dr}). The output of the DC-link voltage controller determines the reference current magnitude, while its phase angle (θ_r) is generated by a PLL to achieve unity power factor operation. The current is subsequently regulated by a quasi-PR controller, denoted as $H_{iL}(s)$, which shares a similar structure to (1) and is characterized by a proportional gain (K_{iLp}), a resonant gain (K_{iLr}), and a bandwidth angular frequency (ω_{iLb}).

6.1.3.3. Overhead catenary systems and HV feeder lines

Both the OCSs and HV feeder lines can be effectively represented using π-equivalent circuit models, incorporating series resistance (R_l), series inductance (L_l), and shunt capacitance (C_l), as depicted in Fig. 21.

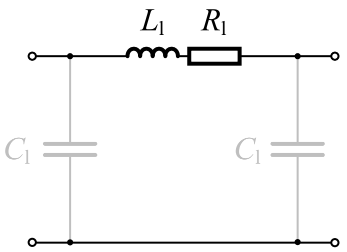

Fig. 21. Equivalent circuit of OCSs and HV feeder lines in simulation model

Although OCS configurations employing booster transformer (BT) and autotransformer (AT) systems differ in their physical structure, they can both be modeled using the π-equivalent approach, with the primary distinction lying in the per-kilometer equivalent impedance values assigned within the model. However, given the relatively short line lengths typically encountered in railway traction systems, the influence of shunt capacitance is negligible and can therefore be omitted from the model.

6.1.3.4. Transformers

In the developed simulation model, all transformers are represented using an equivalent circuit configuration in which the magnetizing impedance (Z_{mtf}) is modeled in parallel with the ideal transformer windings, while the leakage impedance (Z_{ltf}) is placed in series with them, as illustrated in Fig. 22. Although this simplified representation may not fully capture transformer behavior at very high frequencies, it remains sufficiently accurate for the frequency range corresponding to the harmonics of interest in this study.

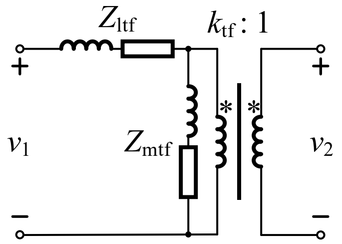

Fig. 22. Equivalent circuit of transformers in simulation model

6.1.4. Simulation models verification

The effectiveness of the developed simulation model is assessed through a series of case studies. Initially, a single SFC is simulated to demonstrate the capability of an individual traction substation to operate under normal conditions. Subsequently, the model is applied to a realistic railway traction system, allowing for a more comprehensive evaluation of its ability to accurately capture the system's dynamic behavior and operational characteristics.

6.1.4.1. Case study for single SFC

As previously discussed, the SFC must ensure continuous and stable power transfer from the 50 Hz national grid to the 16⅔ Hz railway power supply system while maintaining a power factor (PF) within the range of 0.8 capacitive to 0.8 inductive. Additionally, the converter must be capable of operating near its rated power within an inductive load range of 0.8 to 0.95, even under conditions where the current total harmonic distortion (THD) reaches up to 30%.

In addition to ensuring stable operation, the converter must meet several key performance criteria:

1) The power factor on the three-phase input side should remain as close to unity as possible to minimize reactive power exchange with the national grid.
2) The THD of the output voltage should not exceed 5%.
3) The DC component in the output voltage must be minimized to prevent unwanted offset and asymmetry in the power supply.

To evaluate the performance of the developed simulation models for both the DC-link converter and the multilevel converter, three operating conditions are configured. In Condition 1, the output active power is set close to its rated value with a power factor of 0.8 (capacitive). In Condition 2, the output active power is significantly reduced, corresponding to a power factor of 0.15 (inductive). In Condition 3, the output active power is again set near its rated value with a power factor of 0.89 (inductive), while the third and fifth harmonic components are introduced into the load current, resulting in approximately 30% THD. To simplify implementation, the three-phase terminal of the converter is directly connected to a three-phase voltage source, while the single-phase terminal is connected to an ideal controlled current source representing the load.

6.1.4.1.1. DC-link converter

The detailed parameters of the DC-link converter used in simulation is listed in Table I.

Table I. Parameters of DC-link converter used in simulation

PARAMETER	VALUE	PARAMETER	VALUE
Rated apparent power S_b	18 MVA	Inductor of resonant filter L_{n1}	6.3 µH
Rated active power P_b	14.4 MW	Resistor of resonant filter R_{n1}	15 Ω
Rated reactive power Q_b	10.8 MVar	Output filtering inductor L_f	32 mH
Nominal 3-phase line voltage V_{ls}	15 kV	Proportional gain K_{dcp} in $H_{dc}(s)$	0.01
Nominal 3-phase voltage frequency ω_1	50 Hz	Integral gain K_{dci} in $H_{dc}(s)$	5
Nominal 1-phase peak voltage V_r	$15\sqrt{2}$ kV	Proportional gain K_{pllp} in $H_{PLL}(s)$	0.0041
Nominal 1-phase voltage frequency ω_r	16⅔ Hz	Integral gain K_{plli} in $H_{PLL}(s)$	0.0558
Nominal DC-link voltage V_{dcr}	1350 V	Proportional gain K_{cp} in $H_c(s)$	24.69
Rated power of transformer S_{rec}	18 MVA	Resonant gain K_{cr1} in $H_c(s)$	4279.6
Turn ratio of transformer k_{rec}	150/11	Resonant gain K_{cr3} in $H_c(s)$	2261.4
Leakage inductor of transformer L_{lrec}	0.09 p.u.	Resonant gain K_{cr5} in $H_c(s)$	3784.2
Leakage resistor of transformer R_{lrec}	0.008 p.u.	Bandwidth angular frequency ω_{cb}	0.2π
Magnetization inductor L_{mrec}	200 p.u.	Proportional gain K_{vp} in $H_v(s)$	0.062
Magnetization resistor R_{mrec}	200 p.u.	Resonant gain K_{vr1} in $H_v(s)$	19.16
Equivalent DC link capacitor C_{dc}	0.5 F	Resonant gain K_{vr3} in $H_v(s)$	6.09
Capacitor of resonant filter C_{n0}	0.5 F	Resonant gain K_{vr5} in $H_v(s)$	1.52
Inductor of resonant filter L_{n0}	45.6 µH	Bandwidth angular frequency ω_{vb}	0.2π
Resistor of resonant filter R_{n0}	0.96 mΩ	Zero angular frequency ω_z	1123.4
Rated power of transformer S_{inv}	18 MVA	Pole angular frequency ω_p	2690.5
Turn ratio of transformer k_{inv}	9/200	Quadrature reactance of motor X_q^m	0.49

Leakage inductor of transformer L_{linv}	0.16 p.u.	Quadrature reactance of generator X_q^g	0.53
Leakage resistor of transformer R_{linv}	0.016 p.u.	Droop coefficient K_U	2120
Magnetization inductor L_{minv}	500 p.u.	Steepness of transition γ	500
Magnetization resistor R_{minv}	500 p.u.	Gain coefficient K_{Qc}	300
Capacitor of resonant filter C_{n1}	40 μF		

Fig. 23 illustrates the simulated power characteristics on both the three-phase and single-phase sides under Conditions 1, 2, and 3. Here, P_s and Q_s denote the active and reactive power on the three-phase side, while P_o and Q_o correspond to the active and reactive power on the single-phase side. As observed in Fig. 23, the PF on the three-phase side remains significantly lower than unity, indicating non-compliance with the unity PF requirement. This deficiency primarily arises from the inherent inability of the three-phase 12-pulse thyristor rectifier to regulate reactive power in the absence of power factor correction devices within the developed DC-link converter. Such limitations are characteristic of earlier DC-link converter models employing thyristor-based rectifiers. In contrast, modern designs incorporating IGBT-based rectifiers are capable of achieving near-unity PF due to their superior controllability.

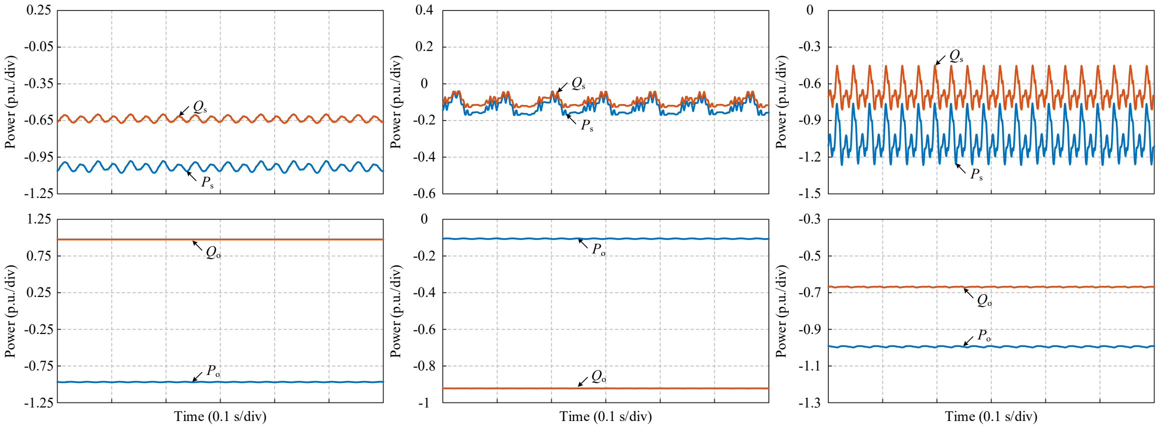

(a) (b) (c)

Fig. 23. Three-phase side and single-phase side powers of DC-link converter for (a) Condition 1, (b) Condition 2, and (c) Condition 3

Fig. 24 presents the steady-state waveforms of the single-phase output voltage and current for the DC-link converter under the three operating conditions, along with their respective voltage spectra obtained via fast Fourier transformation (FFT). The simulation results indicate that even under Condition 3, where the current THD reaches 29.57%, the output voltage remains virtually undistorted. Analysis of the voltage spectrum reveals that the DC components of the output voltage are 0.3 V, 0.16 V, and 0.21 V for Conditions 1, 2, and 3, respectively, values that are sufficiently small to be considered negligible. Furthermore, the THD of the output voltage is measured at 0.08%, 0.07%, and 0.48% for Conditions 1, 2, and 3, respectively, all well within the acceptable limit of 5%.

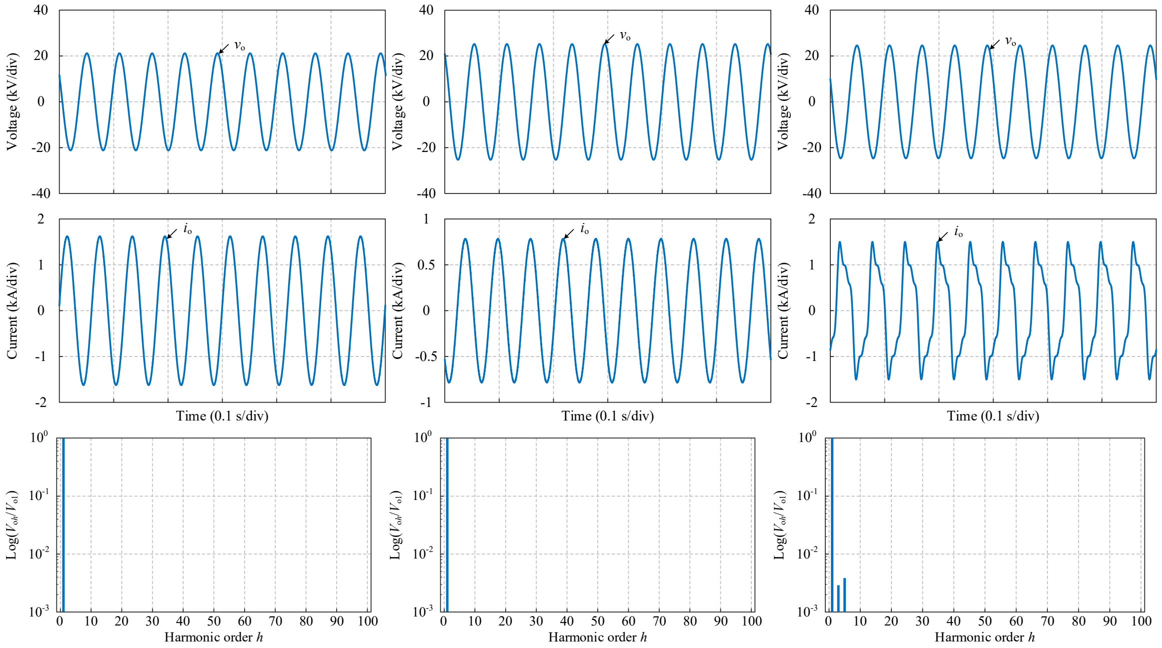

(a) (b) (c)

Fig. 24. Performance of single-phase output voltage and current of DC-link converter for (a) Condition 1, (b) Condition 2, and (c) Condition 3

6.1.4.1.2. Multilevel converter

The detailed parameters of the multilevel converter used in simulation is listed in Table II.

Table II. Parameters of multilevel converter used in simulation

PARAMETER	VALUE	PARAMETER	VALUE
Rated apparent power S_b	17 MVA	Proportional gain K_{c1p} in $H_{c1}(s)$	22.85
Rated active power P_b	13.6 MW	Resonant gain K_{c1r1} in $H_{c1}(s)$	3959.6
Rated reactive power Q_b	10.2 MVar	Resonant gain K_{c1r3} in $H_{c1}(s)$	2094
Nominal 3-phase line voltage V_{ls}	15 kV	Resonant gain K_{c1r5} in $H_{c1}(s)$	3504.4
Nominal 3-phase voltage frequency ω_1	50 Hz	Bandwidth angular frequency ω_{c1b}	0.2π
Nominal 1-phase peak voltage V_r	15√2 kV	Proportional gain K_{v1p} in $H_{v1}(s)$	0.042
Nominal 1-phase voltage frequency ω_r	16⅔ Hz	Resonant gain K_{v1r1} in $H_{v1}(s)$	12.61
Nominal sum module voltage V_{csr}	25 kV	Resonant gain K_{v1r3} in $H_{v1}(s)$	4.35
Arm inductor L	6.3 mH	Resonant gain K_{v1r5} in $H_{v1}(s)$	1.09
Arm resistor R	0.2 Ω	Bandwidth angular frequency ω_{vb}	0.2π
Submodule capacitor C_m	2.7 mF	Zero angular frequency ω_z	1138.7
Output filtering inductor L_s	10 mH	Pole angular frequency ω_p	2678.2

Capacitor of resonant filter C_n	40 µF	Quadrature reactance of motor X_q^m	0.49
Inductor of resonant filter L_n	6.3 µH	Quadrature reactance of generator X_q^g	0.53
Resistor of resonant filter R_n	15 Ω	Droop coefficient K_{U1}	1060
Proportional gain K_{v3p} in $H_{v3}(s)$	0.26	Gain coefficient K_{Qc1}	300
Integral gain K_{v3i} in $H_{v3}(s)$	21.68	Proportional gain K_{up} for PVBC	0.3
Proportional gain K_{c3p} in $H_{c3}(s)$	2.45	Proportional gain K_{ua} for PVBC	0.2
Integral gain K_{c3i} in $H_{c3}(s)$	1409	Damping factor α_{bp}	105
Damping factor α_n	105	Damping factor α_{ba}	105
Proportional gain $K_{\theta p}$ in $H_\theta(s)$	0.0041	Proportional gain K_{ind} for IVBC	0.00024
Integral gain $K_{\theta i}$ in $H_\theta(s)$	0.0558		

Fig. 25 illustrates the simulated power characteristics on both the three-phase and single-phase sides under Conditions 1, 2, and 3. Unlike the DC-link converter, the multilevel converter maintains a unity PF on the three-phase side across all conditions, thereby minimizing reactive power exchange with the national grid and enhancing overall power quality.

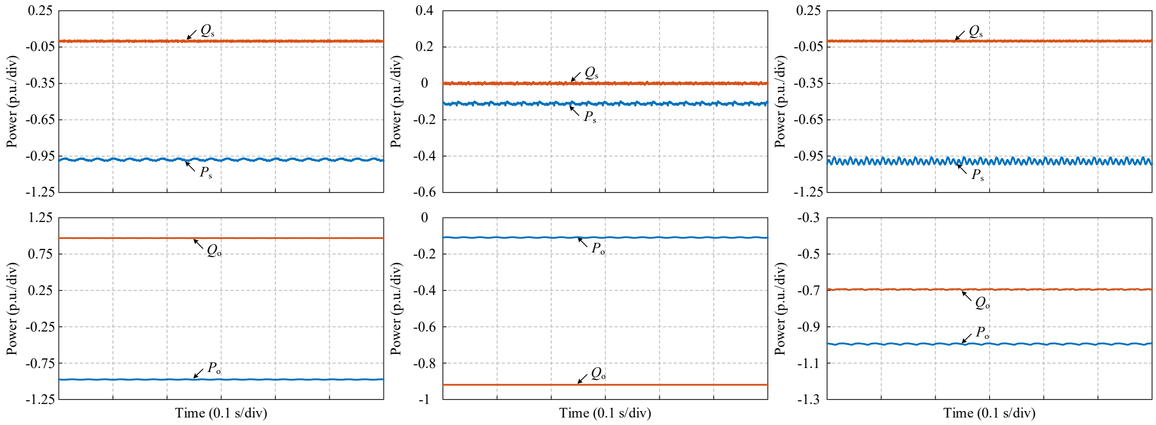

(a) (b) (c)

Fig. 25. Three-phase side and single-phase side powers of multilevel converter for (a) Condition 1, (b) Condition 2, and (c) Condition 3

Fig. 26 presents the steady-state waveforms of the single-phase output voltage and current for the multilevel converter under the three operating conditions, along with their respective voltage spectra. The simulation results demonstrate that even under Condition 3, where the current THD reaches 31.28%, the output voltage remains virtually undistorted. Spectral analysis further reveals that the DC components of the output voltage are 0.18 V, 0.082 V, and 0.026 V for Conditions 1, 2, and 3, respectively, values sufficiently small to be considered negligible. Additionally, the THD of the output voltage is measured at 0.06%, 0.04%, and 0.42% for Conditions 1, 2, and 3, respectively, all well within the permissible threshold of 5%, thereby confirming the converter's capability to maintain high power quality under varying operational conditions.

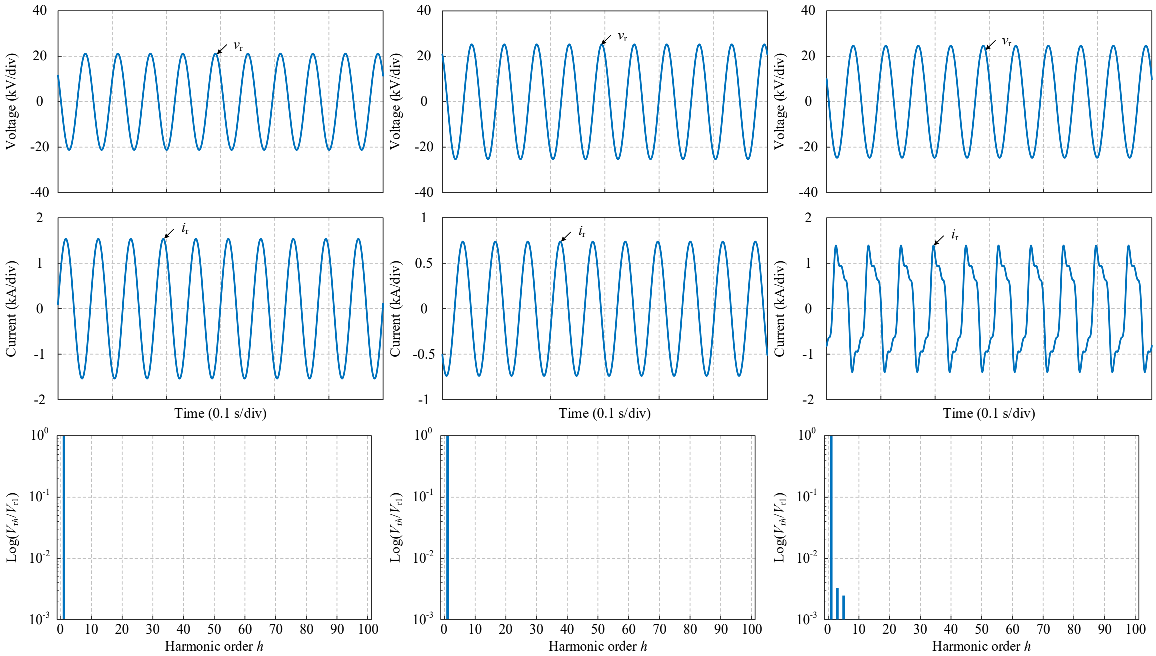

(a) (b) (c)

Fig. 26. Performance of single-phase output voltage and current of multilevel converter for (a) Condition 1, (b) Condition 2, and (c) Condition 3

6.1.4.2. Case study based on realistic system

To provide a more comprehensive evaluation of the developed simulation models, two cases of a simplified yet realistic railway traction system are considered in this section.

6.1.4.2.1. Case 1 for northern railway traction system

Case 1 examines the railway traction system in northern Sweden, spanning from Bastuträsk to Boden. Fig. 27 presents the detailed traction network configuration, including the catenary electrical system and the distances between TPSs.

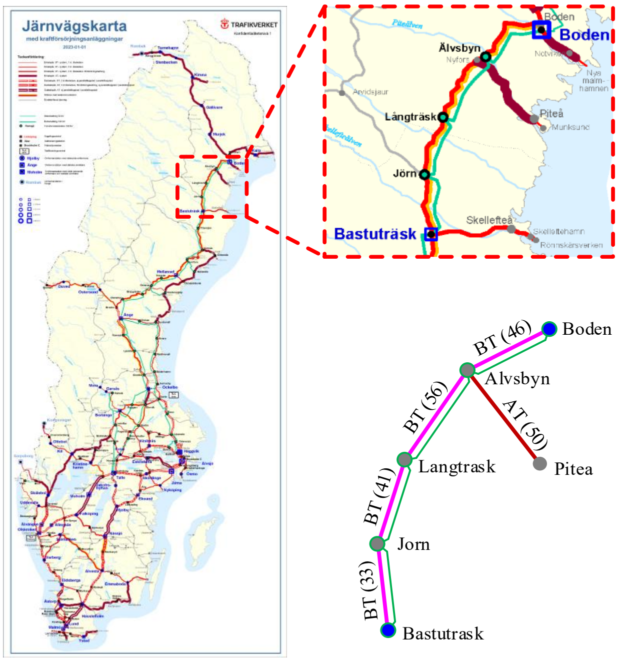

Fig. 27. Exemplified Swedish northern part of railway traction system

In the simulation, two converter-based TPSs, Bastuträsk and Boden, are modeled. In the actual system, Bastuträsk TPS comprises two 15 MVA DC-link converters (Megamacs), while Boden TPS consists of four. For simulation purposes, these are represented by one equivalent 18 MVA DC-link converter, as described in Section 1.1.3.1. The converter parameters remain consistent with Table I, except for X_q^m and X_q^g, which are set to 0.098 p.u. and 0.106 p.u., respectively. Additionally, the simulation incorporates the 132 kV HV feeder system utilized in the northern Swedish railway, where transformer-based TPSs - Jörn, Långträsk, and Älvsbyn - are each equipped with one 16 MVA transformer, while Bastuträsk and Boden TPSs are fitted with one 25 MVA transformers, respectively. The transformer and transmission line parameters are provided in Table III and Table IV.

For simplification, the modeled railway network includes the mainline from Bastuträsk to Boden and a single branch line from Älvsbyn to Piteå, as shown in Fig. 27. Table IV lists the OCS parameters for both BT and AT systems. Passenger transport along the mainline is operated by Norrtåg using X62 locomotives and by SJ using Rc6 locomotives, while Green Cargo dominates freight operations with Rc6 locomotives. The branch line does not support regular passenger service but experiences frequent freight traffic with up to a dozen daily train pairs, primarily using Rc4 locomotives.

Table III. Parameters of transformers

PARAMETER	VALUE
Rated power S_{tf}	16/25 MVA
Turn ratio of transformer k_{tf}	8/1
Leakage inductor of transformer L_{ltf}	0.052 p.u.
Leakage resistor of transformer R_{ltf}	0.0037 p.u.

Magnetization inductor L_{mtf}	500 p.u.
Magnetization resistor R_{mtf}	500 p.u.

Table IV. Parameters of 132 kV HV line and OCSs with BT and AT systems

PARAMETER	**VALUE**
Equivalent inductor for 132 kV line L_{l132}	0.1009 Ω/km
Equivalent resistor for 132 kV line R_{l132}	0.248 mH/km
Equivalent inductor for OCS with BT system L_{lBT}	0.2 Ω/km
Equivalent resistor for OCS with BT system R_{lBT}	1.9 mH/km
Equivalent inductor for OCS with AT system L_{lAT}	0.0335 Ω/km
Equivalent resistor for OCS with AT system R_{lAT}	0.3 mH/km

Based on operational data, Fig. 28 outlines the train loads included in the simulation:

- L1: An Rc6 locomotive accelerating 12 km from Jörn TPS.
- L2: An Rc6 locomotive accelerating 11 km from Långträsk TPS.
- L3: An X62 locomotive accelerating 6 km from Långträsk TPS.
- L4: An Rc6 locomotive decelerating 10 km from Boden TPS.
- L5: An Rc4 locomotive traveling at constant speed 30 km from Älvsbyn TPS.

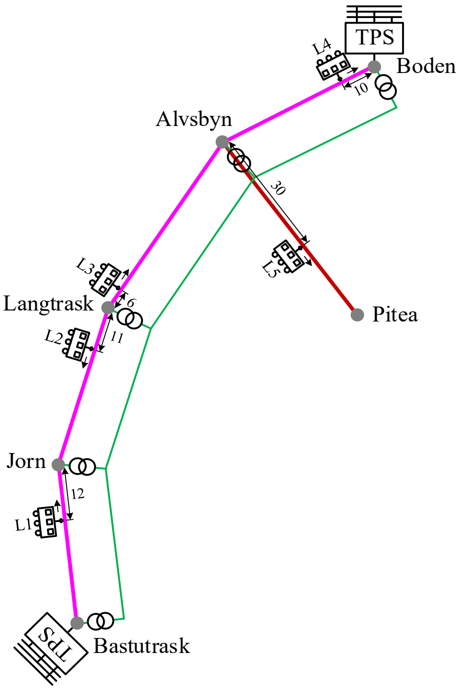

Fig. 28. Loads on the exemplified northern railway traction system used in Case 1

Table V and Table VI detail the parameters for thyristor-based locomotives (Rc6 and Rc4) and voltage source inverter (VSI)-based locomotives (X62). The corresponding power profiles are shown in Fig. 29.

Table V. Parameters of thyristor locomotive used in simulation

PARAMETER	VALUE
Rated apparent power S_{load}	3.6 MVA
Rated power of transformer S_{thy}	4.68 MVA
Turn ratio of transformer k_{thy}	15000/487
Leakage inductor of transformer L_{lthy}	0.0633 p.u.
Leakage resistor of transformer R_{lthy}	0.0384 p.u.
Magnetization inductor L_{mthy}	500 p.u.
Magnetization resistor R_{mthy}	500 p.u.
Armature inductor of DC motor L_{M}	0.74 mH
Base speed of DC motor v_{base}	78 km/h
Maximum EMF voltage of DC motor E_{max}	770 V

Table VI. Parameters of VSI locomotive used in simulation

PARAMETER	VALUE
Rated apparent power S_{load}	2 MVA
Rated power of transformer S_{VSI}	2 MVA
Turn ratio of transformer k_{VSI}	10/1
Leakage inductor of transformer L_{lVSI}	0.1 p.u.
Leakage resistor of transformer R_{lVSI}	0.01 p.u.
Magnetization inductor L_{mVSI}	500 p.u.
Magnetization resistor R_{mVSI}	500 p.u.
Equivalent capacitor C_{d2}	15 mF
Capacitor of resonant filter C_{r}	500 μF
Inductor of resonant filter L_{r}	45.6 mH
Resistor of resonant filter R_{r}	0.01 Ω
Nominal DC-link voltage U_{dr}	2700 V
Proportional gain K_{Udp} in $H_{\mathrm{Ud}}(s)$	0.23

Integral gain K_{Udi} in $H_{\mathrm{Ud}}(s)$	16.7
Proportional gain K_{iLp} in $H_{\mathrm{iL}}(s)$	72.86
Resonant gain K_{iLr} in $H_{\mathrm{iL}}(s)$	2310.7
Bandwidth angular frequency ω_{iLb}	0.2π

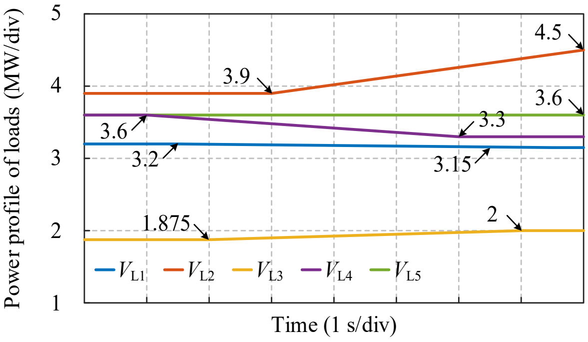

Fig. 29. Power profiles for each load in Case 1

Fig. 30 illustrates the simulated power profiles for TPSs and train loads, where the nominal active and reactive power correspond to the rated values of the DC-link converter. The results indicate that thyristor locomotives generate substantial reactive power, whereas VSI locomotives contribute almost no reactive power. Furthermore, the TPSs dynamically and rapidly adjust to load variations, ensuring stable voltage regulation, as confirmed by the RMS voltage in Fig. 31. The 132 kV HV feeder system effectively maintains pantograph voltages near 1 p.u. even under high-power load conditions.

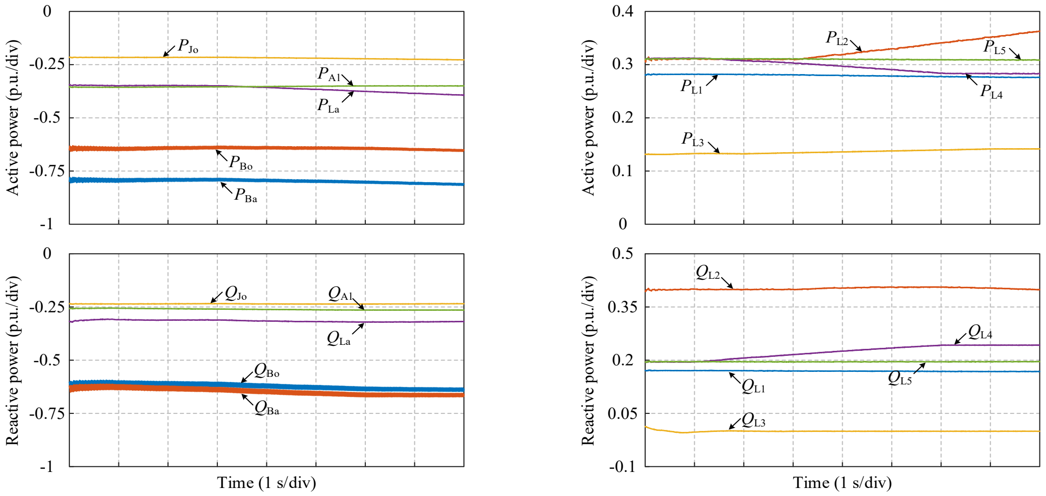

(a) (b)

Fig. 30. Powers of (a) converter-based and transformer-based TPSs and (b) train loads

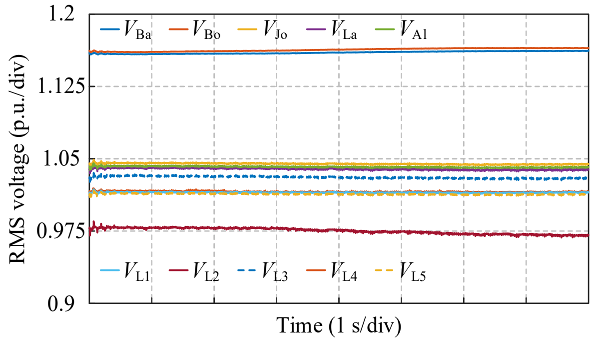

Fig. 31. RMS voltages of TPSs and loads in Case 1

Fig. 32 presents the steady-state single-phase output voltage and current waveforms for Basturäsk and Boden TPSs at the 7th second, along with their respective voltage spectra. Spectral analysis reveals that the DC components of the output voltages are 1.43 V and 1.45 V for Basturäsk and Boden TPSs, respectively. The THD of the output voltage is measured at 1.93% and 1.96%, well within acceptable limits.

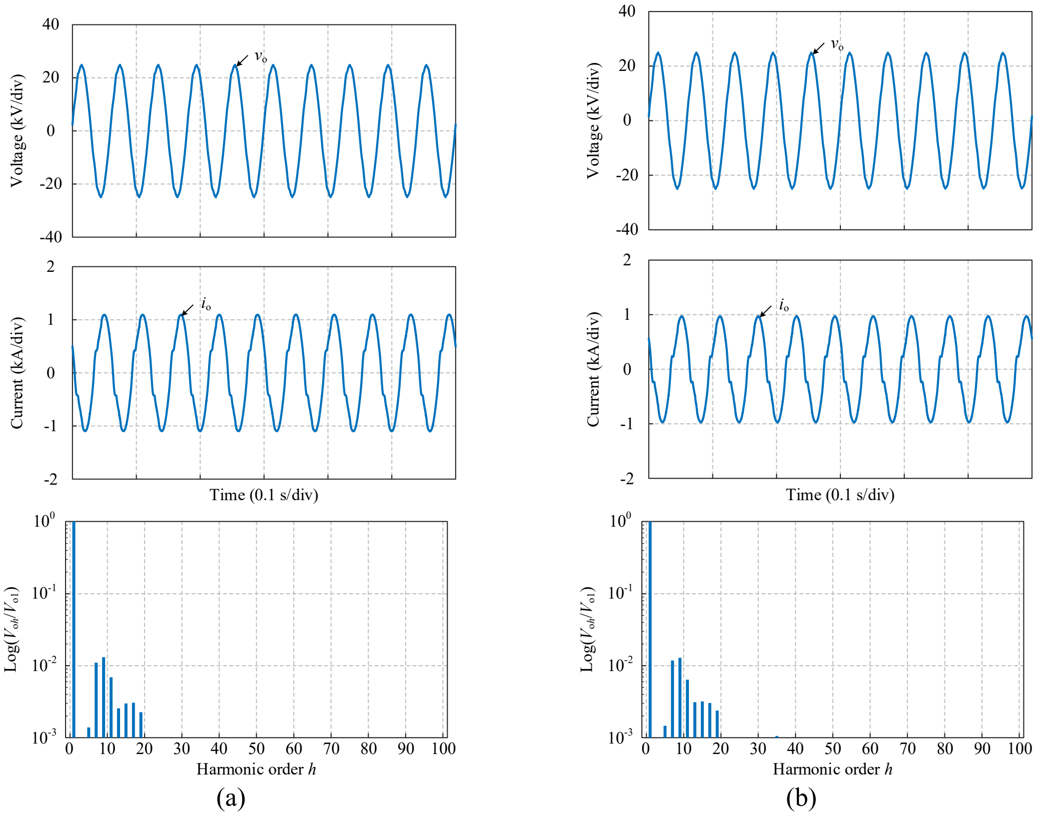

Fig. 32. Performance of single-phase output voltage and current of (a) Basturäsk and (b) Boden TPS

6.1.4.2.2. Case 2 for southern railway traction system

Case 2 focuses on the railway traction system in southern Sweden, covering the route from Malmö to Ystad. Fig. 33 provides a detailed overview of the traction network, including catenary system types and TPS distances.

Fig. 33. Exemplified Swedish southern part of railway traction system

In the simulation, Malmö TPS - comprising two 15 MVA direct converters (YOQC) and one 18 MVA DC-link converter (Megamacs) - is represented by a single 18 MVA DC-link converter, as presented in Section 1.1.3.1. Ystad TPS, consisting of two 9 MVA DC-link converters (Megamacs-6) and one 17 MVA multilevel converter (PLUS), is modeled using a single equivalent 17 MVA multilevel converter. The parameters for the DC-link and multilevel converters remain consistent with Table I and Table II.

The railway network modeled in Case 2 includes the Malmö - Ystad mainline and two branch lines: Malmö - Trelleborg and Ystad - Simrishamn, as shown in Fig. 33. Table IV lists the OCS parameters for BT and AT systems. Passenger traffic along the mainline is operated by Pågatåg using X61 locomotives, while freight transport to Ystad's ferry terminal has been largely discontinued, with only a few remaining freight services. On the Malmö - Trelleborg branch, passenger services use X61 locomotives, and freight trains are operated by Green Cargo using Rd2 and Rc4 locomotives. The Ystad - Simrishamn branch supports only passenger services, also using X61 locomotives.

Fig. 34 presents the simulated train loads:

- L1: An X61 locomotive decelerating 17 km from Fosieby.
- L2: An Rc4 locomotive accelerating 7 km from Fosieby.
- L3: An X61 locomotive accelerating 10 km from Fosieby.
- L4: An X61 locomotive braking 15 km from Ystad TPS.
- L5: An X61 locomotive traveling at constant speed 32 km from Ystad TPS.

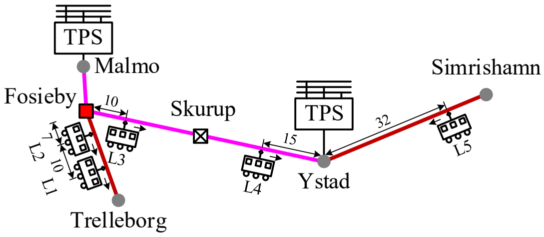

Fig. 34. Loads on the exemplified southern railway traction system used in Case 2

Table V and Table VI list the parameters for Rc4 (thyristor) and X61 (VSI) locomotives. Fig. 35 presents the power profiles, where a single X61 locomotive is rated at 2 MW. The model aggregates multiple locomotives for equivalent simulation.

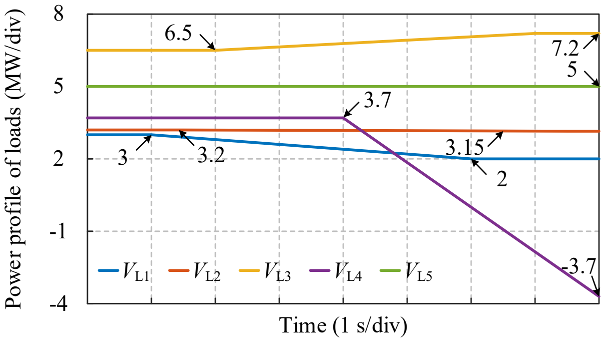

Fig. 35. Power profiles for each load in Case 2

Fig. 36 illustrates the simulated TPS and load power. Notably, the reactive power of VSI locomotives remains near zero, regardless of active power variations. The TPSs dynamically adjust to load fluctuations, ensuring voltage stability, as demonstrated by the RMS voltage waveforms in Fig. 37. When L4 engages regenerative braking, its power is directly absorbed by other loads, causing a temporary reduction in active power at Ystad TPS. Although regenerative braking may introduce voltage fluctuations, the system maintains voltages close to 1 p.u.

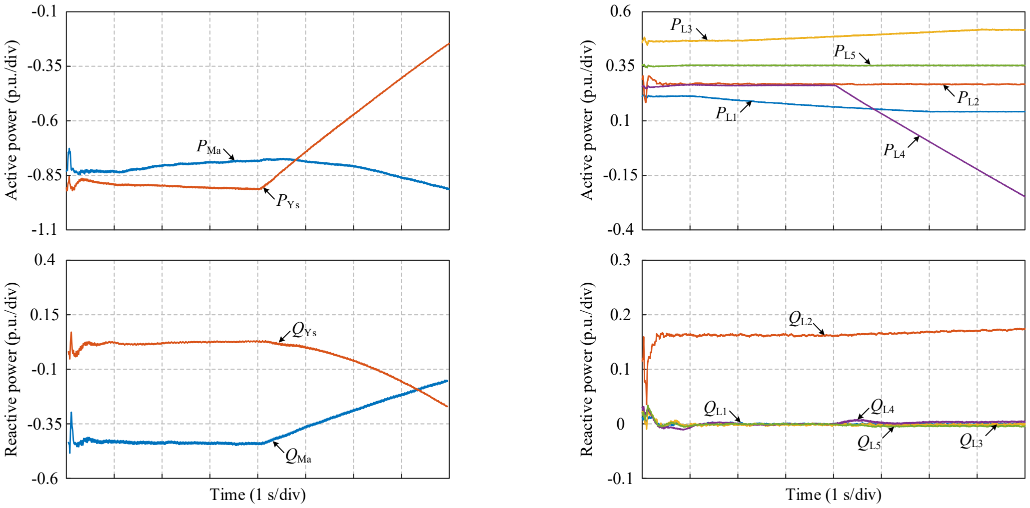

(a) (b)

Fig. 36. Powers of (a) Malmö and Ystad TPSs and (b) train loads

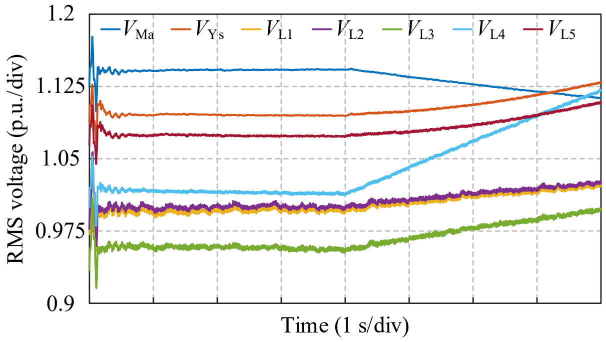

Fig. 37. RMS voltages of TPSs and loads in Case 2

Fig. 38 depicts steady-state waveforms for Malmö and Ystad TPSs at the 7th second, along with their respective voltage spectra. Spectral analysis indicates that the DC components of the output voltage are 12.93 V and 18.27 V for Malmö and Ystad TPSs, respectively. Despite being higher than in Case 1, these values remain negligible compared to the fundamental voltage of 16.5 kV. Moreover, the output voltage THD is 1.08% for Malmö TPS and 0.4% for Ystad TPS, highlighting the superior harmonic suppression capability of the multilevel converter compared to the DC-link converter.

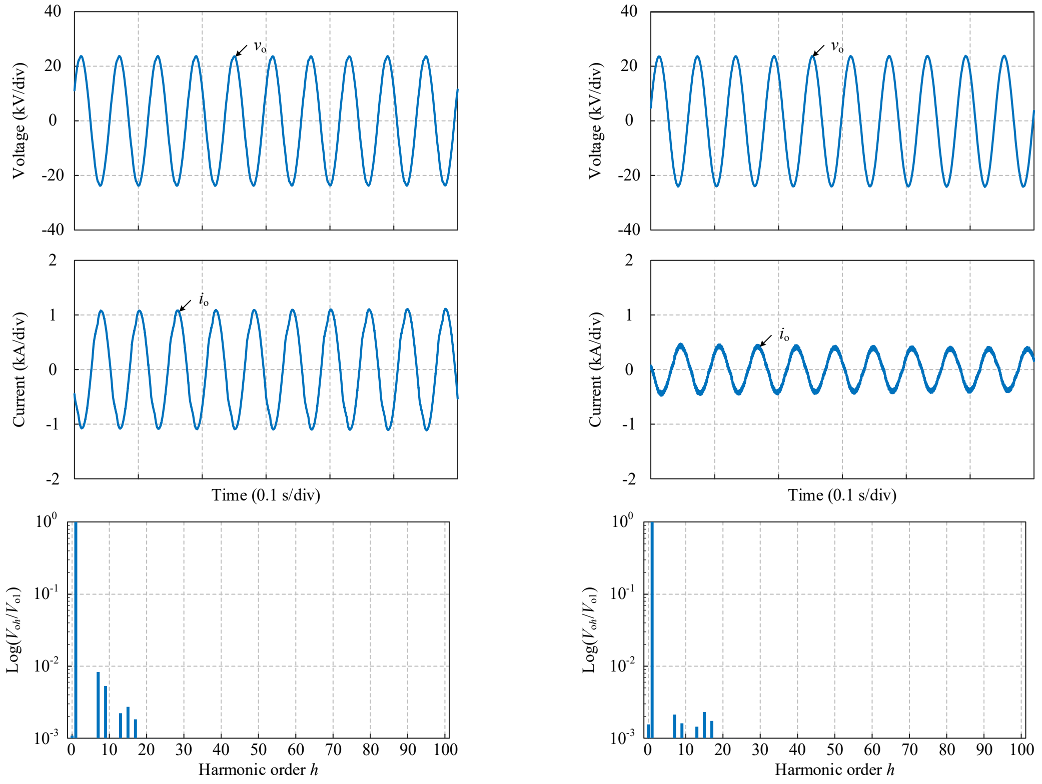

(a) (b)

Fig. 38. Performance of single-phase output voltage and current of (a) Malmö and (b) Ystad TPS

6.1.5. Investigation on energy storage systems for railway applications

One effective approach to enhancing brake energy utilization is the integration of ESSs in trains or substations [11]. This strategy reduces the need for dissipating excess energy through resistors, thereby lowering operational costs. Beyond energy recovery, ESSs contribute to the overall efficiency and performance of railway systems in several ways: (1) mitigating power peaks and their associated economic costs, even as demand increases [12]; (2) stabilizing voltage [11]; (3) enhancing the maximum available power in DC systems [12]; (4) serving as an alternative to constructing new substations in areas prone to significant voltage drops [13]; (5) reducing overall energy consumption without compromising operational efficiency or punctuality; (6) improving network performance during train acceleration while ensuring the stability and safety of the electrical supply network; (7) providing power autonomy in locations where overhead lines cannot be installed; and (8) offering backup support in the event of a power failure, allowing trains to reach a safe location [14].

6.1.5.1. ESS technologies

Energy storage plays a pivotal role in improving energy efficiency and system stability. Significant financial investments have driven the rapid development of diverse storage technologies, which are typically categorized into five main types based on their energy conversion mechanisms: chemical, electrochemical, mechanical, electrical, and thermal [18], [23], [26]. However, certain mechanical storage methods, such as pumped hydroelectric storage (PHES), compressed air energy storage (CAES), and gravity energy storage (GES), as well as thermal storage systems, are excluded from this study due to their unsuitability for railway applications. The advantages and limitations of each technology are summarized in Table VII.

Table VII. Strengths and weaknesses of the different types of ESS

TYPE OF ESS	STRENGTHS	WEAKNESSES
LA	Low cost Established technology	Heavy and bulky Long time to charge Short lifetime Low energy density Low power density Cannot be deeply discharged
Ni-Cd	Proven technology Longer lifetime High sturdiness Wide temperature operating range	Memory effect Requires periodic deep discharge maintenance Hazardous material (cadmium)
Li-ion	High energy density Light weight No memory effect Low self-discharge High efficiency	High price Safety risk (fire) Aging and capacity degradation over cycles
Ni-MH	High energy density	Safety risk (fire)

	High specific energy No memory effect	Low cycle life
VRB	Environmentally friendly Electrolyte can be recycled Long lifetime Can be fully discharged Low self-discharge	High cost Environmental concerns (toxicity of electrolyte) Electrolyte degradation over long-term use Low maturity
FC	High specific energy High efficiency No degradation	Low efficiency High cost Requires hydrogen supply Limited hydrogen infrastructure
Flywheel	High lifetime Fast response time Quick recharge High power density Environmentally friendly	Low energy density High self-discharge Rotor failure risk Friction losses
EDLC	High efficiency High capacity Low maintenance High power density Environmentally friendly Long cycle life (>1M cycles) Fast response time	Low energy density High self-discharge
SMES	High power density Fast response Long lifetime Low degradation	High cost Strong magnetic fields High self-discharge Low energy density Requires low-temperature cooling

6.1.5.1.1. Electrochemical energy storage

Electrochemical ESS are broadly classified into batteries and flow batteries. In batteries, charge is stored within the electrodes, whereas in flow batteries, charge is stored in a liquid electrolyte that is circulated to electrode surfaces [15].

Batteries, composed of one or more electrochemical cells, convert stored chemical energy into electrical energy. Their high efficiency and energy density make them widely adopted in electrified railway systems, such as trams and metro trains [16]. The most relevant battery chemistries for railway applications include:

- **Lead-Acid (LA) Batteries:** As one of the earliest rechargeable battery technologies [17], LA batteries are cost-effective but suffer from low energy and power density, heavy weight, long charging times, and short cycle life [18]. Historically, in 1912 and 1914, they have been deployed in two railway lines as battery posts in parallel with power substations in Japan but were eventually phased out after approximately 15 years of operation due to maintenance challenges. However, in 1980, Japan National Railway reintroduced LA batteries at Nakajima Station for three years for verification testing [16].

- **Nickel-Cadmium (Ni-Cd) Batteries:** Ni-Cd batteries offer long cycle life, reliability, and resilience across a wide temperature range. However, their drawbacks include the memory effect and environmental hazards associated with cadmium, which have led to regulatory restrictions [19], [20].
- **Lithium-Ion (Li-ion) Batteries:** Li-ion batteries are characterized by high energy density, efficiency, and low self-discharge rates [21]. However, their high cost and material supply constraints limit large-scale deployment [22]. Safety concerns, particularly thermal runaway, necessitate ongoing research into improving stability [23].
- **Nickel-Metal Hydride (Ni-MH) Batteries:** Ni-MH batteries replace cadmium with hydrogen, reducing environmental concerns. They offer higher energy density while avoiding memory-effect issues. However, they are susceptible to overcharging, which can lead to excessive heat generation and potential hydrogen release, necessitating complex charging systems. Additionally, they suffer from shortened lifespan under high current discharges (200 - 300 cycles) [19], making them unsuitable for applications such as light rail vehicles (LRVs), which require up to 2 million cycles over a decade [24].

Flow batteries store energy in external liquid electrolytes, enabling extended energy retention and flexible scalability [25]. During charging and discharging, these electrolytes flow through electrochemical cells, converting chemical energy into electrical energy. The energy capacity of flow batteries is determined by the volume of the electrolyte tanks, while power density depends on the design of the electrochemical cell. This design flexibility makes flow batteries suitable for both power- and energy-oriented applications [26]. However, their adoption is hindered by high complexity, cost, and the risk of electrolyte leakage. Furthermore, auxiliary systems, such as pumps required for electrolyte circulation, introduce efficiency losses and spatial constraints [27].

Among these flow battery technologies, vanadium redox batteries (VRBs) are particularly promising, which offer several advantages over conventional batteries. First, their electrolyte production is relatively simple, cost-effective, and transportable. Second, any cross-contamination of electrolytes merely necessitates recharging rather than replacement, ensuring minimal degradation and maintenance [28]. Additionally, VRBs can be fully discharged without sustaining damage. However, their commercialization has been limited by the high cost of ion-exchange membranes [18]. Safety and environmental concerns also arise due to vanadium toxicity [29]. Furthermore, because the electrolyte must be continuously circulated, additional cooling systems are required, increasing both cost and footprint [30].

6.1.5.1.2. Chemical energy storage: Hydrogen and Fuel Cells

Unlike batteries, fuel cells (FCs) require an external fuel and oxidant supply, enabling continuous operation as long as fuel is available [31]. Hydrogen is a key energy carrier due to its high efficiency and environmental sustainability [32]. However, since hydrogen does not exist naturally in its elemental form, it must be synthesized using primary energy sources [31].

Hydrogen-based ESS comprises water electrolysis (for hydrogen generation), buffer tanks (for storage), and fuel cells (for electricity generation). FCs offer high specific energy and long operational lifespans but face challenges such as high capital costs and low round-trip efficiency [32]. In railway applications, FCs have been primarily integrated into diesel-electric hybrid locomotives. Notable examples include Japan’s ‘Kiha E200,’ which achieved a 9% energy efficiency improvement over conventional diesel trains, and Canada’s “Evolution Hybrid

Locomotive," as documented in UIC reports [34]. In Europe, Alstom's hydrogen-powered "Coradia iLint" multiple unit has been operational since 2018, running on a German regional line alongside conventional diesel units [35]. Hybrid systems integrating FCs with Li-ion batteries are under investigation [36]. However, the regeneration of hydrogen from braking energy remains unexplored, making FCs more akin to energy generation than storage devices.

6.1.5.1.3. Mechanical energy storage: Flywheel

Mechanical storage technologies include CAES, PHS, GES, and flywheel systems [15]. Among these, flywheel energy storage is particularly relevant for railway applications.

Flywheels store energy as rotational kinetic energy, which is converted back into electricity via a motor-generator system. The total energy storage capacity is dictated by the rotational speed and size of the flywheel rotor, while the power output is determined by the motor-generator unit [37]. Moreover, they offer high power density, rapid charge-discharge cycles, and minimal environmental impact. These attributes make them well-suited for high-power, short-duration applications in railway systems [37], [38]. However, they exhibit relatively low energy density, high standby losses, and potential safety concerns related to rotor failure, which necessitate protective containment systems [38], [38].

6.1.5.1.4. Electrical energy storage

Electrical energy storage technologies include supercapacitors and superconducting magnetic energy storage (SMES), both of which leverage electric and magnetic fields for energy retention. These systems offer high power output with moderate energy density [17].

Electrical double-layer capacitors (EDLCs), commonly known as supercapacitors, provide high power density, low internal resistance, and superior efficiency in managing dynamic load variations and cyclic operations [40], [41]. They also feature moderate maintenance costs and scalable storage capacity, making them customizable to specific railway applications. While EDLCs exhibit a higher self-discharge rate and lower energy density compared to battery ESS (BESS) [42], they excel in handling cyclic operations and peak power demands. Consequently, they are widely deployed in onboard ESSs for LRVs, including those operating without overhead catenary systems [43], yielding substantial cost savings [44]. Research has also explored their integration into diesel-powered trains [45] and hybrid configurations with BESS to harness the complementary advantages of both storage technologies [46].

In addition to onboard applications, EDLCs are employed in stationary energy storage solutions at substations for voltage stabilization and energy conservation purposes [47]. Notable commercial implementations include the SITRAS SES (Stationary Energy Storage System) developed by Siemens [48], with installations across Spain, Germany, and China [49]. Other key benefits of EDLCs include their use of environmentally friendly materials, minimal heat generation, and enhanced safety [50].

SMES systems store energy through the magnetic field generated by a direct current flowing through a superconducting coil maintained below its critical temperature [40], enabling highly efficient energy retention [21]. Their ability to deliver instantaneous power with virtually unlimited high-efficient charge cycles makes them advantageous for applications requiring continuous operation and full cycling capability [31], [37]. While promising for traction substations and grid stabilization, their direct implementation in railway applications is limited. Only a few numbers of simulation studies have explored its potential role in mitigating fluctuating power demands in railway systems, but these configurations necessitate hybridization with battery systems to enhance performance [51].

Despite their technical advantages, SMES faces significant economic and operational barriers, primarily due to the high capital and maintenance costs associated with cryogenic cooling. Additionally, the strong magnetic fields generated, especially in large-scale implementations, pose safety and interference concerns [40]. Other drawbacks include high self-discharge rates and the susceptibility of superconducting coils to even minor temperature fluctuations [37].

6.1.5.2. Converter topologies for wayside ESSs

ESSs in railway applications can be deployed in two primary configurations: as stationary installations at substations along the railway (wayside ESS, WESS) or as onboard systems integrated into trains. This section focuses on WESS, examining their integration and the associated converter topologies in both DC and AC railway traction networks.

The deployment of WESS in railway networks generally follows two main approaches. One is parallel connection to the power source or DC link (if present in the traction converter), and another is direct connection to the bus of the DC or AC traction network.

For WESS supplying DC voltage and interfaced with the DC terminal of a traction system, direct integration is feasible without the need for an intermediate power converter. This configuration offers notable advantages, including reduced cost, improved energy efficiency, and system simplification. However, it also introduces challenges such as voltage compatibility, control complexity, operational flexibility, and system protection. Consequently, bidirectional DC-DC converters are commonly employed to enhance adaptability and system performance. Flywheel-based ESS, in contrast, inherently generate AC voltage via electromechanical systems such as permanent magnet synchronous machines (PMSMs) or induction machines. In such cases, a three-phase full-bridge AC-DC converter is required to facilitate power transfer to the DC terminal of the traction system [52].

The topology of bidirectional DC-DC converters can be broadly categorized into non-isolated and isolated types. Non-isolated converters are well-suited for applications with low voltage conversion ratios and where galvanic isolation is unnecessary [53], offering advantages such as reduced size, lower weight, and immunity to magnetic interference. Common non-isolated topologies include Buck, Boost, Buck/Boost, Ćuk, and Sepic/Zeta converters, with the Buck/Boost topology (as shown in Fig. 39 (a)) being particularly favored due to its step-up and step-down voltage regulation capabilities and reduced component [54]. However, in high-voltage railway applications, the inherent limitations necessitate advanced configurations such as multiphase or cascaded Buck/Boost converters [55], as depicted in Fig. 39 (b) and Fig. 39 (c), which offer improved power-handling capacity and voltage scalability.

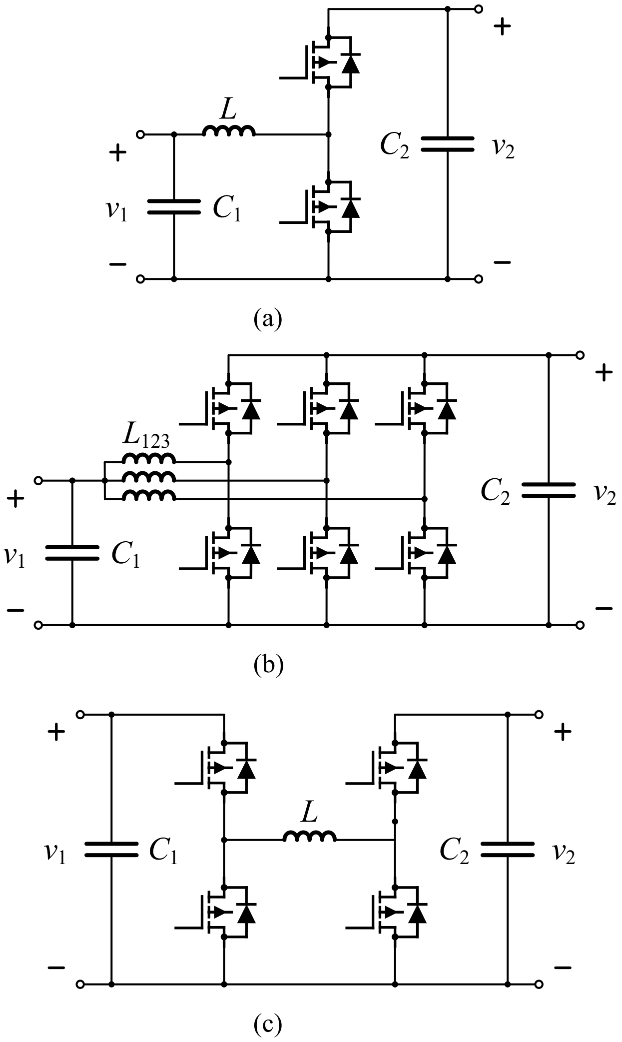

Fig. 39. Common non-isolated DC-DC converters: (a) Buck/Boost converter; (b) multiphase Buck/Boost converter; (c) cascaded Buck/Boost converter

For applications requiring galvanic isolation and high voltage transfer ratios, isolated converters provide a viable solution by first converting DC voltage to AC, transmitting power through a high-frequency transformer, and then rectifying the output back to DC. The inclusion of high-frequency transformers within these converters enables effective voltage matching between different system levels while ensuring compliance with insulation requirements. Therefore, this approach enhances system safety and flexibility at the expense of increased size, cost, and power losses [56]. Among the various isolated topologies, dual active full-bridge (DAB) and dual active half-bridge converters have gained prominence due to their efficiency in handling bidirectional power flow while maintaining isolation [53], as shown in Fig. 40.

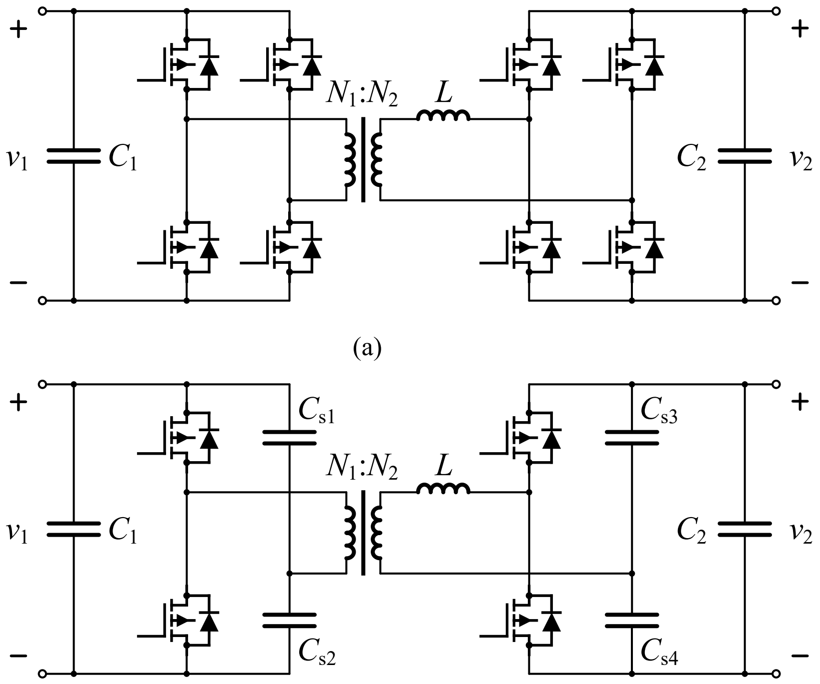

(a)

(b)

Fig. 40. Common isolated DC-DC converters: (a) dual active full-bridge converter; (b) dual active half-bridge converter

The integration of WESSs into AC railway traction networks necessitates DC-AC conversion, which may be complemented by cascaded bidirectional DC-DC conversion to improve system adaptability, as shown in Fig. 41 (a). Flywheel-based ESSs, in contrast, rely on AC-AC or AC-DC-AC converters to facilitate bidirectional power exchange with the traction network. Conventional two-level VSCs remain the predominant approach for interfacing ESSs with AC railway systems. However, their application in high-voltage and high-power scenarios is constrained by high switching losses, reliance on bulky DC-link capacitors, and the need for low-frequency transformers and filters. To mitigate these limitations, multi-level converter topologies such as diode-clamped and neutral-point-clamped (NPC) configurations have been explored. While diode-clamped architectures suffer from DC-link voltage imbalance [57], NPC converters require large filter components to manage neutral-point voltage fluctuations and suppress low-frequency ripple effects, which may impact ESS lifespan [58].

A promising alternative lies in the adoption of modular multi-level converters (MMCs) and cascaded H-bridge (CHB) converters, which offer improved scalability, lower switching losses, and reduced filter requirements, as shown in Fig. 41 (b) and Fig. 41 (c). In certain implementations, energy storage devices are integrated directly into the high-voltage DC side of the MMC, though this approach introduces challenges related to internal energy balance and circulating currents that may compromise system stability [59]. Decentralized integration at the sub-module level of MMCs or CHB converters has been proposed as a means to enhance system scalability while addressing these concerns [60]. Moreover, flywheel-based ESSs benefit from the use of AC-AC matrix converters, which eliminate the need for intermediate energy storage components, thereby improving reliability and power density [61].

Compared to single-stage architectures that exclude bidirectional DC-DC conversion, the incorporation of an additional conversion stage introduces trade-offs in power density and cost. However, this approach significantly enhances ESS performance by improving energy utilization efficiency, increasing operational flexibility, stabilizing voltage and power delivery, extending battery lifespan, simplifying design and maintenance, and enabling adaptation to diverse application scenarios. While conventional bidirectional DC-DC converters provide a robust foundation for railway ESS integration, additional topologies such as quasi-Z-source [62], flyback [63], and series resonant converters [64] can be deployed to address specific operational requirements. For flywheel-based ESSs, back-to-back VSCs, as shown in Fig. 41 (d), enable AC-DC-AC conversion while offering fault ride-through capability, further enhancing system resilience [65]. Additionally, back-to-back VSCs can serve as railway power conditioners and phase compensation devices in three-phase 50 Hz railway traction networks, where ESSs are connected to the DC link to improve overall power quality and system reliability [66].

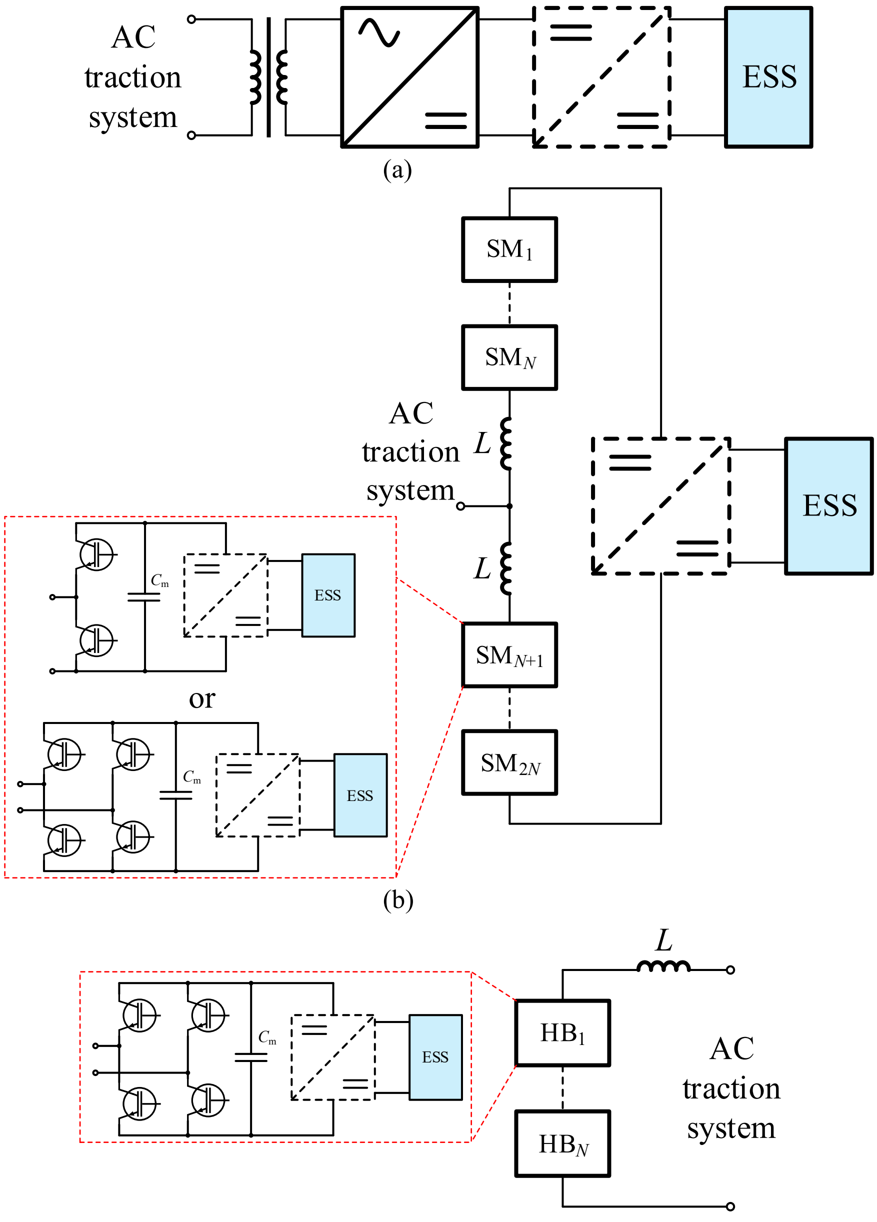

(a)

(b)

(c)

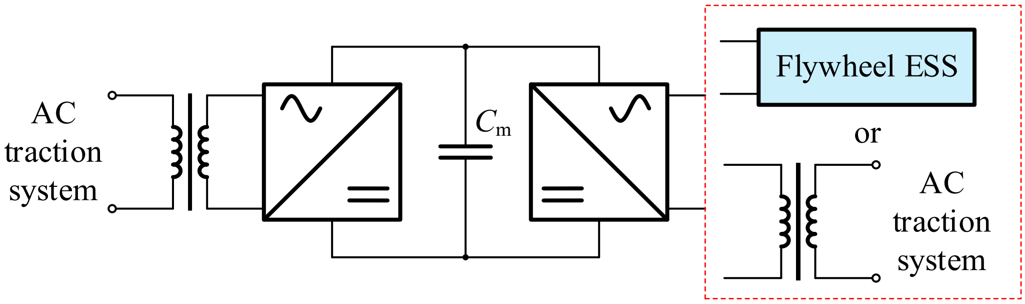

(d)

Fig. 41. Typical conversion for the integration of WESSs into AC railway traction networks: (a) DC-AC converter; (b) multilevel converter; (c) cascaded H-bridge converter; (d) back-to-back converter

6.1.5.3. Control strategy of ESSs

The control strategy of ESSs can be categorized into energy management control and converter control. The energy management control strategy is responsible for power distribution among different energy storage subsystems, ensuring coordinated operation within the ESS. Meanwhile, the converter control strategy governs the charging and discharging states of the ESS by driving the power converter.

It is important to note that the discussion here is confined to energy management strategies at the individual energy storage unit level, whereas broader energy management strategies for the entire railway system will be explored in subsequent sections.

6.1.5.3.1. Energy management

During ESS operation, power distribution and working mode discrimination are crucial aspects [66]. Existing coordination strategies for energy storage management primarily fall into three categories: filtering-based control, fuzzy logic-based control, and model predictive control (MPC) [67].

Filtering-based control separates the high-frequency and low-frequency components of the target power through a filtering algorithm, generating distinct power reference values for different ESS components. This method is structurally simple and easy to implement. A low-pass first-order filter has been utilized to allocate power between supercapacitors and batteries, enhancing the efficient use of regenerative braking energy [66]. However, conventional low-pass filters introduce time delays, the step energy management strategies to mitigate energy exchange issues in hybrid ESSs (HESSs) for railway applications is developed in [67]. Further refinements include improved filtering algorithms that effectively suppress excessive energy exchange and mitigate voltage loop overshoot [68].

The selection of the filter time constant is a critical factor influencing power allocation and capacity utilization in HESSs. To address the challenges of selecting an optimal time constant and dealing with abrupt signal fluctuations, advanced filtering algorithms such as Kalman filtering [69] and wavelet transform-based methods [70] have been explored, providing more adaptive and robust control.

Fuzzy logic control is an intelligent control approach that does not require explicit mathematical relationships between inputs and outputs. A multi-mode hybrid energy storage fuzzy control strategy has been proposed in [71] to optimize energy utilization in railway systems. Hybrid approaches that integrate filtering-based control with fuzzy logic have also been developed, with optimization techniques such as particle swarm optimization used to refine fuzzy membership functions [72]. Additionally, fuzzy logic controllers have been employed for DC bus voltage regulation in railway traction networks [73].

The inputs of a typical fuzzy control strategy commonly include traction load power and the state of charge (SOC) of the ESS, while the output determines the charging/discharging thresholds or power reference values. A dynamic threshold control strategy for urban rail HESSs has also been proposed, utilizing traction substation output and supercapacitor SOC as inputs to determine the no-load voltage of the traction network [74].

The effectiveness of fuzzy control depends heavily on the formulation of fuzzy rules. For instance, when applied to peak shaving and valley filling in railway load management, fuzzy rules consider the power deviation, where charging and discharging decisions are dynamically adjusted based on this deviation. The control accuracy and dynamic performance of fuzzy logic methods are, however, constrained by expert knowledge and heuristic rule formulations, limiting their ability to achieve truly optimal control.

MPC is an optimization-based closed-loop control strategy that utilizes a rolling horizon approach. MPC effectively distributes power among different ESS components by formulating an objective function and constraints to optimize energy storage capacity allocation [75]. It has been used to determine optimal power reference values under various constraints [75] and to develop single-train trajectory optimization and hierarchical energy management models for substations [76].

Beyond power allocation, MPC has also been applied to direct control of ESS converters by optimizing the duty cycle signals. By defining appropriate cost functions and constraints, MPC enhances the performance of bidirectional power converters in railway applications [77]. Given the periodic but stochastic nature of traction load demand that impacted by factors such as weather conditions, holidays, and driving behaviors, MPC has also been extended to multi-timescale optimization strategies, further improving system economic performance and reliability.

6.1.5.3.2. Converter control strategy

The converter control strategy for railway ESSs consists of three main components: (1) compensation current reference calculation, (2) inverter control, and (3) energy storage device control.

Under full compensation conditions, the post-compensation power supply currents are determined analytically [78]. The corresponding compensation current reference value is derived by subtracting the measured current from the computed compensation current [66], [78], [79]. In contrast, under optimal compensation conditions, an optimization model is employed to determine the ideal compensation power using advanced optimization algorithms [80].

In inverter-based ESSs, control objectives primarily focus on ensuring fast reference tracking and stabilizing the DC-link voltage or, in the case of multilevel converters, the module voltage. The most widely adopted approach integrates a double closed-loop voltage and current control structure with an appropriate current tracking mechanism. The outer voltage loop maintains the stability of the DC-side or module voltage, while the inner current loop refines the actual reference values, ensuring precise and responsive control. A comparative assessment of various current tracking control methods is provided in Table VIII [66].

Table VIII. Comparison of tracking control methods

METHOD	ADVANTAGES	DISADVANTAGES
Hysteresis comparison control	Fast response, inherent steady-state accuracy	Unfixed switching frequency, leading to variable switching losses and increased harmonics
Repeated prediction deadbeat control	Ensures smooth current tracking, corrects periodic tracking errors, prevents modulation failure	Control lag, sensitive to predicted values, time-varying nonlinear traction load increases control complexity
Direct fuzzy tracking control	High robustness and fast convergence, capable of handling nonlinear factors	Slower response speed, limited precision in highly dynamic conditions
Fuzzy recursive PI control	Minimizes steady-state error in the system	Slower response compared to deadbeat control methods
Quasi-resonant control	Effectively suppresses harmonic resonance in specific frequency ranges	Performance is highly dependent on system frequency stability and requires precise tuning of control gain

Energy storage devices comprise storage media and, in many cases, bidirectional DC-DC converters. These converters typically implement different control strategies, including constant current control, constant power control [81], and voltage/current double closed-loop control [79]. The selection of an appropriate control mode depends on the power demand of the traction network and the remaining energy capacity of the ESS, ensuring optimal energy utilization and system efficiency.

6.1.5.4. Practical applications of WESSs

WESSs play a critical role in enhancing the energy efficiency and operational resilience of railway networks by capturing and redistributing regenerative braking energy. Unlike onboard ESSs, which are constrained to storing energy generated by a single train, WESSs enable multiple trains to benefit from the recovered energy. By storing excess braking energy that cannot be immediately utilized, these systems allow for its later reinjection into the system to support train acceleration and traction demand [12]. This approach not only enhances energy utilization but also contributes to peak shaving and load balancing, reducing overall power consumption and reliance on external grid supply. Additionally, since WESS installations are independent of train weight and spatial limitations, their deployment does not impact rolling stock performance [40]. In the event of system failures or maintenance requirements, WESSs can be serviced without interrupting railway operations, thereby improving system reliability and maintainability.

The strategic placement of WESSs within railway networks is essential for maximizing energy recovery and minimizing transmission losses. These systems are typically installed in substations or at locations prone to frequent voltage drops, such as railway stations, where they can provide voltage support and improve power quality. However, the physical separation between WESS installations and the trains they support introduces energy transmission losses, which can reduce overall system efficiency. To address this challenge, numerous studies have sought to optimize WESS placement along railway lines to minimize these losses while maintaining effective energy redistribution. By leveraging advanced optimization techniques, researchers have identified optimal deployment strategies that enhance energy recovery rates and improve the overall efficiency of railway electrification systems [82], [83].

Empirical evidence from real-world implementations further underscores the viability and effectiveness of WESS technology in railway applications. Table IX provides an overview of existing WESS installations, highlighting the technologies employed and their operational status. The majority of deployed systems utilize flywheel ESSs, Li-ion batteries, or EDLCs, with a single documented case of a Ni-MH battery and a LA battery installation. Notably, Siemens initially introduced a flywheel ESS-based solution in Germany but subsequently transitioned its focus toward EDLC-based systems, culminating in the development of Sitras SES, which has since been deployed in at least 11 cities worldwide, including locations in the United States, Germany, and Spain. However, it is important to recognize that some WESS implementations, such as the ACE2 and SA2VE pilot projects in Madrid, were experimental in nature and are no longer in operation. These cases highlight the evolving landscape of WESS technologies and the continuous refinement of energy storage solutions to meet the demands of modern railway systems.

Table IX. Application of WESSs in railway traction systems

NAME	MANUFACTURER	ESS					APP.	PLACE	YEAR	REF.
		Type	P (MW)	U (V)	Cap. (kWh)	Discharge time (s)				
-	Siemens	Flywheel	0.6	750	6.6	-	light rail	Cologne, Germany	2000	[84]
Sitras SES	Siemens	EDLC	0.7	750	2.3	-	-	Cologne, Germany	2001	[85]
			1	600	2.3		metro	Madrid, Spain	2002	[85], [87]
			-	600/ 750	-		-	Dresden, Germany	2002	[85]
				600/ 750				Bochum, Germany	2004	
				750				Nuremberg, Germany	2007	[86]
				750				Beijing, China	2007	
				600				Rotterdam, Netherlands	2010	
				600				Toronto, Canada	2011	
				600			light rail	Portland, USA	2015	[85], [86]
-	Woojin Industrial Systems Co	EDLC	-	55000 (AC)	11.68	-	high-speed rail	KTX line, Korea	2009	[104]
			1.865	1500	7.78		metro	Daejeon, Korea	2010	[85], [16], [104]
			-	1500	10.4/13/13/13/10.4		metro	Seoul, Korea	2011/2012/2012/2013/2014	[85], [104]
				1500	5.84		metro	Daegu, Korea	2013	
				750	2.9		-	Incheon, Korea	2014	
				620	2.44			Boston, USA	2015	[104]
EnerGstor	Bombardier	EDLC	0.65	600-1500	1	-	metro	Kingston, Canada	-	[85]
Powerbridge	Piller	Flywheel	1/0.3	600	4.6/5	16	-	Hanover, Germany	1998/ 2004	[85]

			-	750	-	-		Hamburg, Germany	2006	
				750				Paris, France	2007	
				600			trolley	Zürich, Switzerland	2009	
				750			-	Rennes, France	2010	
				750			light rail	Bielefeld, Germany	2012	
			1	750	7.3		-	Freiburg, Germany	2013	[85], [105]
Battery post (1st generation)	RTRI	Lead-acid	-	1500	2	-	regional rail	Shinetsu line, Japan	1912	[16]
					1.5			Yamanote line, Japan	1914	
					-			Nakajima station, Japan	1980	
Enviline ESS/Envistor	Envitech Energy (ABB group)	Li-ion (Saft Intensium Max)	2.2	660	420	-	-	Philadelphia, USA	2012	[85]
		EDLC	2.2	1500	6.66		metro	Melbourne, Australia	-	
			3.3	750	11.1			Warsaw, Poland	2016	
NeoGreen Power ES	Adetel	EDLC	1	750	3	-	light rail	Lyon, France	2011	[85], [106]
			0.66	750	2			Tours, France	2014	
NeoStab			-	850	-		regional rail	St.Gervais-Vallorcine line, France	2015	[85]
Capapost	Meidensha Corporation	EDLC	3	1500	-	-	metro	Hong Kong, China	2016	[85]
			-	1500	19.26		regional rail	Tokyo, Japan	2016	
Vycon REGEN	Vycon (Calnetix)	Flywheel	2	750	8.32	15	metro	Los Angeles, USA	2014	[85], [108],
-	Rosseta Technik GmbH	Flywheel	0.5	600/750	6	-	tram	Dessau, Germany Zwickau, Germany	2006	[85]
GTR system	Kinetic Traction Systems (Urenco Power Technology + Pentadyne Power Corporation)	Flywheel	-	750	-	-	metro	Paris, France	-	[85], [109]
			0.3	630	3			London, UK	2000	[85], [87], [16]
			1	-	-		-	New York, USA	2002	[85], [109]
			0.6	750				Lyon, France	2003-2004	
B-CHOP	Hitachi	Li-ion	1/0.5/1/2	1500	37.4/-/-/-	20	metro	Kobe, Japan	2005/2007	[85], [107], [50], [110]
			1	1500	-	-	-	Seoul, Korea	2011	[85]
			2	1500	76.12		regional rail	Hajima station, Japan	2013	[85], [111]
			0.1	750	-		-	Osaka, Japan	2014	[85]

			2	1500	137.02		regional rail	Okegawa station, Japan	2014	[85], [111]
			2.145	1500	-			Horinouchi station, Japan	2014	[85]
			-	750		-		Hong Kong, China	2016	
Gigacell Battery Power System (BPS)	Kawasaki	Ni-MH	1.9	670	367	-	metro	New York, USA	2010	[85], [112]
			5.6	750	205			Osaka, Japan	2011, 2013	[85], [50], [112]
				750	385			Washington D.C., USA	2012	
			-	750	204			Sapporo, Japan	2013	[85], [112]
				-	203		monorail	Tokyo, Japan	2013, 2014	
SCiB	Toshiba	Li-ion	0.5	-	18.7	-	regional rail	Nagoya line, Japan	-	[107], [50]
			0.25		18.1		tram	Kagoshima, Japan	2007	
-		Flywheel	2	-	25	-	regional rail	Zushi station, Japan	1988	[16], [107], [50]
-		EDLC	2.56	1500	6.875	-	regional rail	Agono and Shumarusub stations, Japan	2007	
ACE2 (project)	-	Flywheel	0.35	3000	55	-	-	Madrid, Spain	2003	[85], [16]
SA2VE (project)			5.6		0.88				2006	

6.1.5.5. Analysis of WESSs

Regardless of the specific functional requirements an ESS must meet, no single technology can comprehensively satisfy all criteria, necessitating trade-offs in system design and implementation. The optimal selection of an ESS is inherently application-dependent, as different storage technologies exhibit distinct advantages and limitations shaped by their operational characteristics.

To identify the most suitable solutions for storing and reusing regenerative braking energy in railway systems, an initial screening of existing deployments (summarized in Table IX) has been conducted. This analysis has led to the selection of three primary technologies: EDLCs, flywheel ESSs, and Li-ion batteries, based on their maturity and demonstrated performance in railway applications. Additionally, while SMES remains an emerging technology in this context, it has been included due to its unique characteristics that may offer advantages in railway operations. Conversely, hydrogen FCs have been excluded, as their current role in rail applications aligns more closely with power generation rather than ESS.

The following subsection provides clear and simple selection guidelines to support technology choice for typical railway use cases. In particular, Table X links representative deployments to their primary objectives, key selection drivers, and the issues each technology was intended to address. The performance of these storage technologies can be assessed through multiple key parameters based on the data presented in Table A1 of appendix [113].

6.1.5.5.1. Selection guidelines for WESS technology

The key parameters discussed in the following subsections are synthesised into practical guidance for selecting wayside energy storage technologies in railway systems. The selection should be application dependent and should follow a consistent sequence from the intended function to the required discharge time and power, and finally to the trade-offs implied by efficiency and lifetime, energy and power density, and total capital cost. Table X links this selection logic to representative deployments reported in Table IX and summarises the objective, the main selection drivers, and the issues each solution was intended to address.

- Application objective

Selection should start by defining the intended function in the traction power network. In railway systems, WESS is primarily applied to increase the utilization of regenerative braking energy and to support traction demand. It is also used to mitigate power peaks and stabilise voltage where network constraints limit performance.

- Discharge time and power

The objective should then be translated into the required discharge time and power. Short, frequent events place priority on rapid response and high power capability, while longer support over minutes requires higher usable energy capacity. As shown in Fig. 47 in subsection 6.1.5.5.4, EDLCs and Flywheel ESS are positioned for short discharge time and high power operation, while Li-ion batteries extend toward longer discharge time for energy management. SMES is also positioned within the desired operational range for short discharge time applications. This step provides the first selection between high power buffering and energy shifting solutions.

- Efficiency and lifetime

Efficiency should be considered together with lifetime for the expected duty cycle. For strongly cyclic use cases, high cycle life and stable performance over repeated charge and discharge can outweigh small differences in efficiency. In 6.1.5.5.2, Fig. 42 shows that EDLCs, Flywheel ESS, and SMES exhibit efficiency closely following 90%, while Li-ion batteries demonstrate comparatively low efficiency, and the lifetime comparison indicates that lifetime should be checked together with the duty cycle. Fig. 44 further supports that EDLCs and Flywheel ESS offer a favourable balance between efficiency and cycle life for strongly cyclic use cases. Standby losses and self discharge should also be checked because they reduce the net recovered energy.

- Energy and power density

Energy and power density guide the match between technology and site constraints. High power density favours fast power exchange, whereas higher energy density supports longer discharge duration and higher throughput. As shown in Fig. 45 and Fig. 46 in 6.1.5.5.3, EDLCs offer notable advantages in power density, while Li-ion batteries and SMES exhibit higher energy density, and Flywheel ESS and SMES outperform the other solutions in specific power. These trends help confirm whether the selected technology matches the required discharge duration and throughput. Available space, permissible mass, and integration constraints should be verified at this stage.

- Total capital cost

Total capital cost should be assessed from a life cycle perspective that reflects capital expenditure, maintenance needs, and replacement intervals driven by ageing and duty cycle. In 6.1.5.5.5, Fig. 48 to Fig. 50 provide capital cost comparisons per unit power and per unit energy for Li-ion batteries, Flywheel ESS, EDLCs, and SMES, and Fig. 51 highlights the contribution of replacement cost and operation and maintenance cost within the overall life cycle cost. These comparisons support a selection that is consistent with the required power and discharge time identified in the previous step. Safety, siting, and maintenance requirements must be addressed to confirm feasibility. The following table summarises how these factors have influenced deployed choices in practice.

Table X. Mapping representative WESS deployments to selection rationale and targeted issues

DEPLOYMENT SYSTEM	ESS TYPE	RAIL CONTEXT	PRIMARY OBJECTIVE	KEY SELECTION RESONS	ISSUES ADDRESSED / TRADE-OFFS	REF.
Sitras SES (Madrid)	EDLC	Metro (600 V)	Regenerative energy recuperation and voltage support	Fast response; very high cycle life; high power density	Addresses frequent braking cycles; trade-offs: low energy capacity and self-discharge	[85], [87]
EnerGstor (Kingston)	EDLC	Metro (600-1500 V)	Peak power reduction and energy recuperation	High power capability; high cycle life; mature deployment	Addresses substation peaks; trade-offs: limited energy and standby losses	[85]
Enviline ESS/Envistor (Melbourne)	EDLC	Metro (1500 V)	Voltage stabilisation and braking energy reuse	Fast power support; high cycling; robust interface	Addresses voltage dips/peaks; trade-offs: low energy density	[85]
NeoStab (St.Gervais-Vallorcine)	EDLC	Regional rail (850 V)	Power quality support and energy recuperation	Fast response; frequent cycling; long lifetime	Addresses fluctuating load; trade-offs: limited discharge duration	[85]
Powerbridge (Hanover)	Flywheel	Urban rail (600 V)	High-power energy recuperation and peak shaving	High power; rapid charge/discharge; long lifetime	Addresses short high-power events; trade-offs: self-discharge and mechanical containment	[85]
Vycon REGEN (Los Angeles)	Flywheel	Metro (750 V)	Regenerative energy capture and traction support	High power; fast response; high cycling capability	Addresses repeated braking events; trade-offs: standby losses and mechanical safety constraints	[85], [108]
GTR system (London)	Flywheel	Metro (630 V)	Energy recuperation and power support	High power density; long cycle life; fast response	Addresses voltage/power fluctuations; trade-offs: self-discharge	[85], [87], [16]
ACE2 (Madrid)	Flywheel	Traction supply (3000 V)	Energy recuperation / power bridging	Fast response; high cycling; short-duration support	Addresses transient power demand; trade-offs: mechanical complexity	[85], [16]
Enviline ESS/Envistor (Philadelphia)	Li-ion battery	Urban rail (660 V)	Energy recuperation and energy management	Higher energy capacity; longer discharge; good efficiency	Addresses energy shifting beyond seconds; trade-offs: aging and thermal management	[85]
B-CHOP (Kobe)	Li-ion battery	Metro (1500 V)	Braking energy reuse and peak shaving	Higher energy; flexible discharge duration; mature integration	Addresses energy recuperation with longer support; trade-offs: safety/thermal	[85], [107], [50], [110]

					management	
SCiB (Kagoshima)	Li-ion battery	Tram	Energy recuperation and auxiliary power support	Higher energy density; battery cycling robustness (design dependent)	Addresses repeated braking cycles; trade-offs: capacity fade over lifetime	[107], [50]
Gigacell BPS (New York)	Ni-MH battery	Metro (670 V)	Energy recuperation and peak shaving	Higher energy capacity; established battery technology	Addresses energy management; trade-offs: lower energy density and replacement planning	[85], [112]

6.1.5.5.2. Efficiency and lifetime

Efficiency and operational lifetime play a crucial role in determining system viability. EDLCs and SMES exhibit efficiencies exceeding 90%, with Flywheel ESS closely following at 90%, while Li-ion batteries demonstrate comparatively lower efficiency, as illustrated in Fig. 42. A further evaluation of lifespan, depicted in Fig. 43, reveals that Flywheel ESS, EDLCs, and SMES are characterized by long service lives, whereas Li-ion batteries have a shorter lifespan. However, lifetime must also be considered in terms of charge-discharge cycles rather than absolute years, as frequent cycling accelerates degradation, particularly in electrochemical storage systems. For instance, Flywheel ESS longevity is primarily dictated by the durability of mechanical components [31], whereas Li-ion batteries experience performance deterioration due to chemical and electrolyte degradation [26]. By contrast, SMES, which operates without moving parts or chemical reactions, boasts superior cycle life [114]. Fig. 44 presents a comparative analysis of ESS technologies based on efficiency and cycle life, underscoring that EDLCs and Flywheel ESSs offer the most favorable balance between these factors.

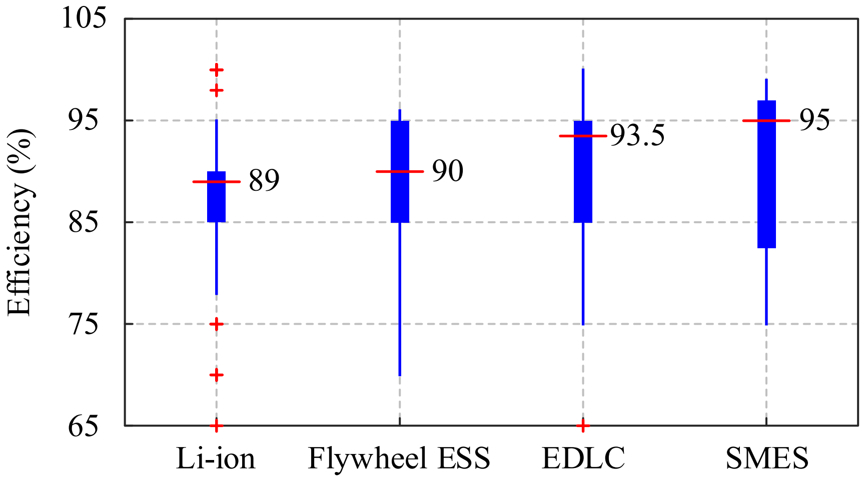

Fig. 42. Efficiency of ESS (Data from Table A1)

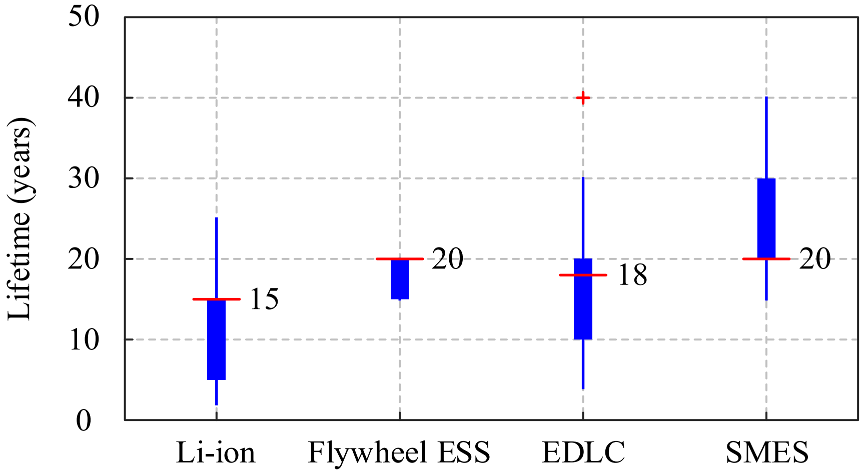

Fig. 43. ESS lifetime in years (Data from Table A1)

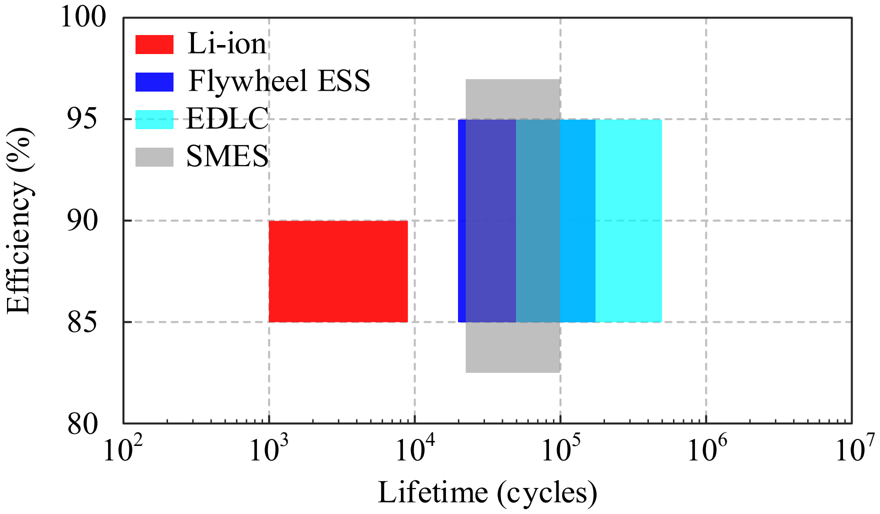

Fig. 44. Efficiency and cycle life of ESS (Data from Table A1)

6.1.5.5.3. Energy and power density

Beyond efficiency and longevity, energy and power density serve as critical parameters for determining storage applicability, where spatial and weight constraints are significant. The Ragone plot [115] in Fig. 45 provides a comparative evaluation of mass-to-energy and mass-to-power ratios among ESS technologies. Li-ion batteries, as expected, demonstrate high energy and power density. EDLCs also offer notable advantages in power density, while SMES and Flywheel ESS occupy intermediate positions. Similarly, specific energy and specific power (Fig. 46) further reinforce these findings, indicating that EDLCs and SMES excel in high-power applications requiring rapid energy discharge, while Li-ion batteries emerge as the most lightweight and energy-dense option.

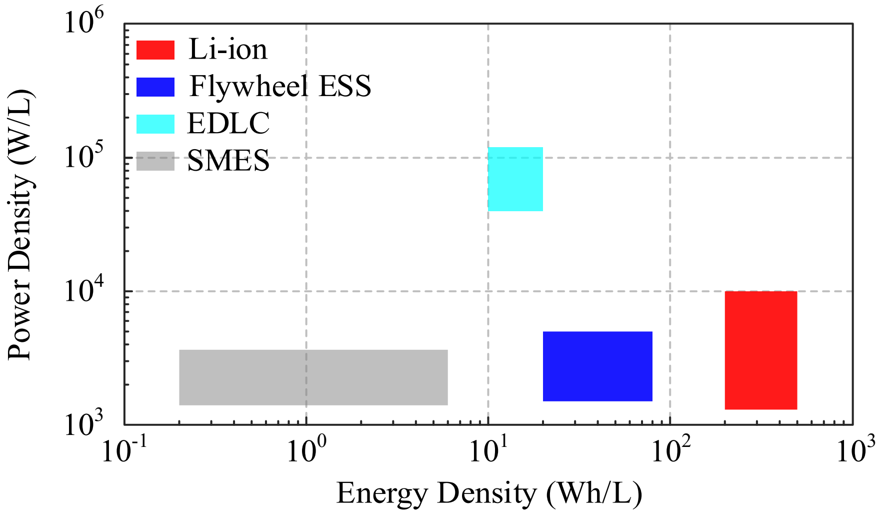

Fig. 45. Comparison of ESSs depending on power and energy density (Data from Table A1)

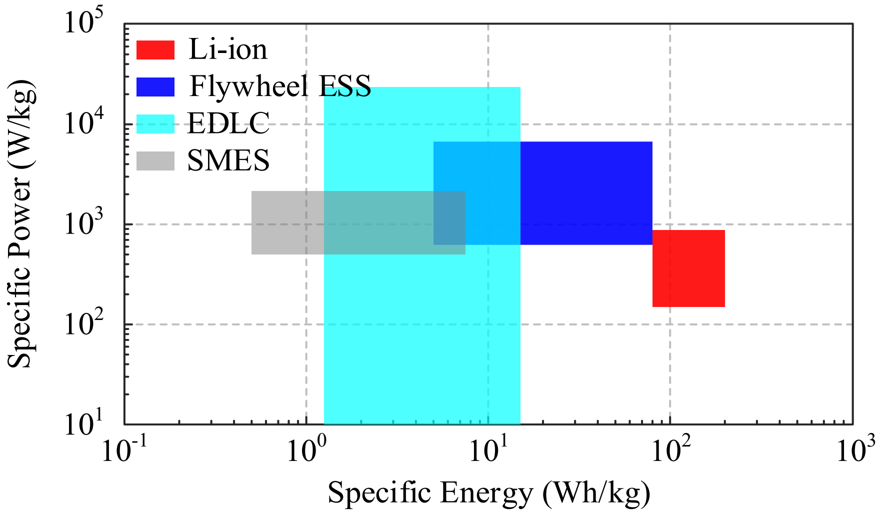

Fig. 46. Comparison of ESSs depending on specific power and energy (Data from Table A1)

6.1.5.5.4. Discharge time and power

Considering the operational demands of railway braking and acceleration cycles, discharge time is another crucial parameter. As shown in Fig. 47, different storage technologies align with distinct functional applications: energy management (requiring long-duration storage and discharge), bridging power (providing emergency backup and continuity of service), and power quality/uninterruptible power supply (UPS) applications [116], where rapid charge-discharge capability is essential. Among the selected technologies, Flywheel ESS, Li-ion batteries, EDLCs, and SMES are positioned within the desired operational range, making them well-suited for railway applications.

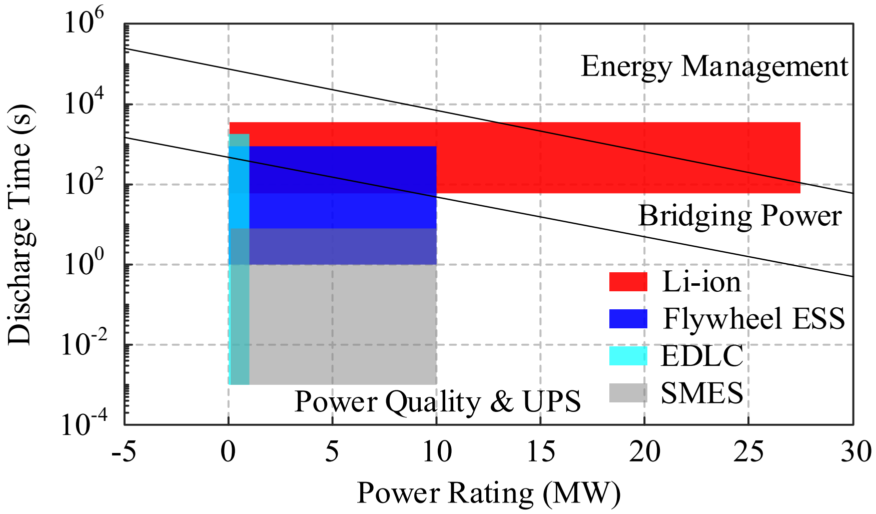

Fig. 47. Power and discharge time (Data from Table A1)

6.1.5.5.5. Total capital cost

The economic feasibility of ESS deployment is also a key consideration, with total capital cost (TCC) serving as a primary metric for commercial viability. The TCC of different ESSs is influenced by multiple cost components [26], [38], [117], expressed as

$$TCC = C_{\mathrm{PCS}} + C_{\mathrm{BOP}} + C_{SU} \cdot h \tag{15}$$

where C_{PCS}, C_{SU} and C_{BOP} represent the power conversion system (PCS) cost per unit power (SEK/kW), storage unit cost per unit energy (SEK/kWh), and balance-of-plant (BOP) costs per unit power (SEK/kW), and h is the charging/discharging time.

Fig. 48 highlights the relative cost distribution among technologies, revealing that Flywheel ESS, EDLCs, and SMES exhibit lower power costs than energy costs, making them more suitable for high-power, short-duration applications [18]. Conversely, Li-ion batteries, with their higher energy cost component, are better suited for longer-duration energy storage. Fig. 49 further illustrates the capital cost per unit power across different technologies, while Fig. 50 refines the analysis by incorporating the life cycle [40], [31], [33], which account for the frequency of charge-discharge cycles. This perspective underscores that Li-ion batteries, despite their high energy density, exhibit a relatively higher cost per cycle, impacting long-term economic feasibility.

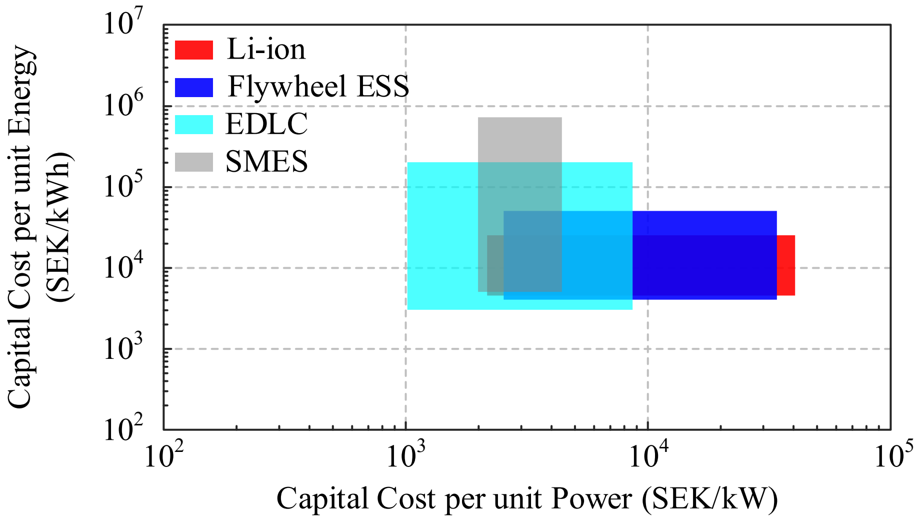

Fig. 48. Power cost vs energy cost of ESSs (Data from Table A1 using an exchange rate of 1 USD = 10.15 SEK)

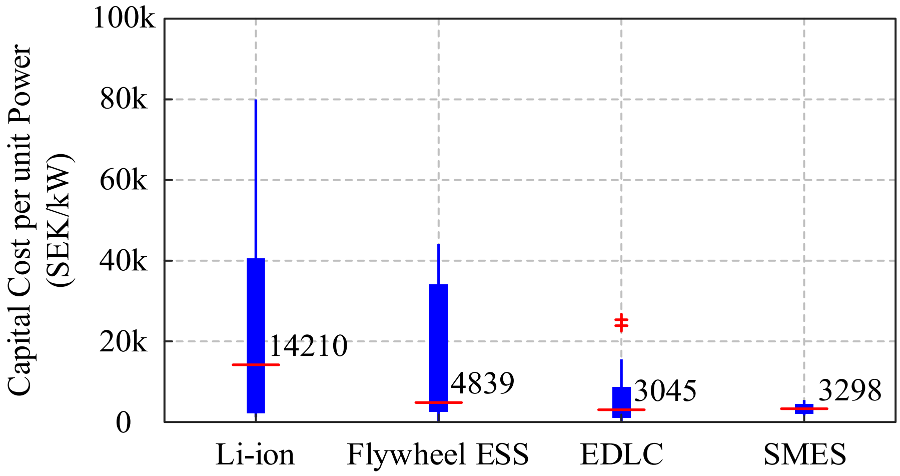

Fig. 49. Capital cost per unit power of ESSs (Data from Table A1 using an exchange rate of 1 USD = 10.15 SEK)

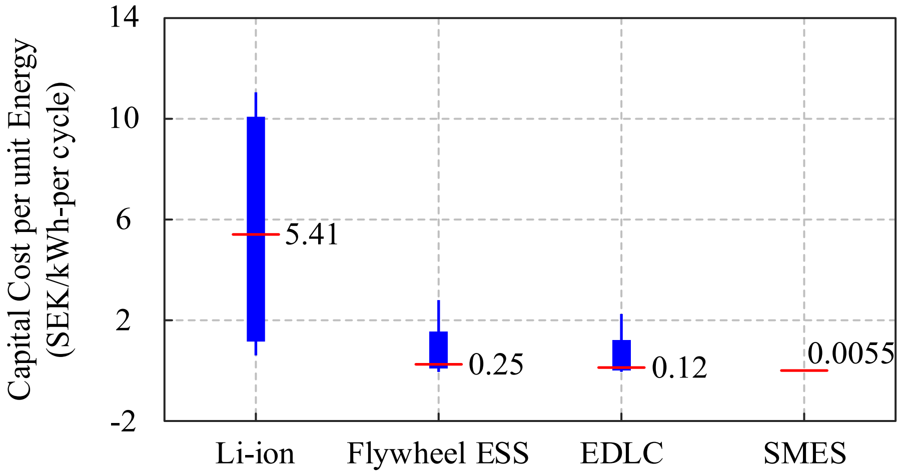

Fig. 50. Capital cost per unit energy of ESSs (Data from Table A1 using an exchange rate of 1 USD = 10.15 SEK)

A broader economic assessment, incorporating replacement and maintenance costs [118], provides a more comprehensive perspective on ESS cost-effectiveness. Some studies, such as Mostafa et al. [117], extend the analysis to life cycle cost (LCC) calculations, which account for replacement costs (C_{REP}), end-of-life disposal and recycling costs (C_{EOL}), and total operation and maintenance (O&M) costs (C_{OM}) over the system's lifetime, expressed as

$$LCC = TCC + C_{OM} + C_{REP} + C_{EOL} \,. \tag{16}$$

The LCC framework, as represented in Fig. 51, offers insights into the long-term financial implications of ESS deployment. Notably, EDLCs present the most favorable LCC profile among railway storage technologies. However, these findings are contingent upon assumptions regarding project duration and system lifetime. Sensitivity analyses indicate that LCC decreases with extended project lifespan until ESS end-of-life is reached, at which point replacement costs contribute to a slight increase.

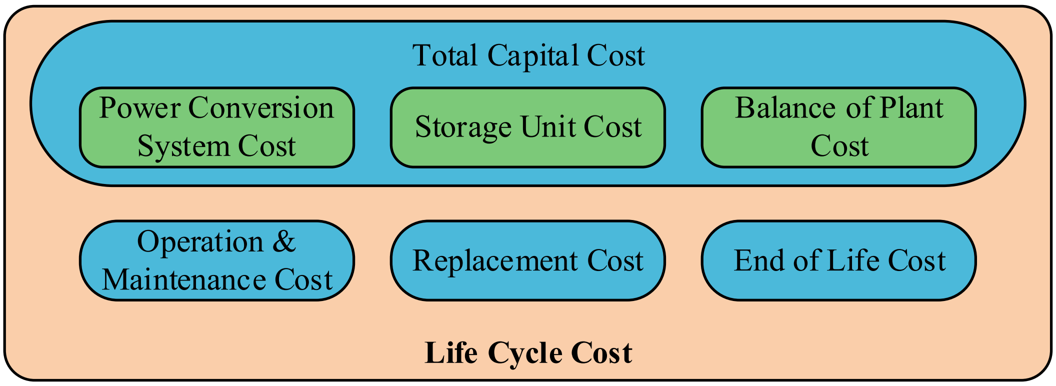

Fig. 51. Overall life cycle cost structure of ESS

6.1.6. System performance improvement with ESSs

6.1.6.1. Comparison of DC-AC converter with ESSs for Swedish railway traction system

6.1.6.1.1. Design and control of additional converter interfacing ESSs

In this work, a solution is proposed to enhance railway system performance and recover regenerative braking energy by integrating an additional parallel DC-AC converter with an ESS into TPSs. The simulation model of the proposed converter comprises a four-quadrant converter (4QC) for AC-side voltage and power control, and an ESS for DC-link voltage regulation and energy management. The structural configuration of this system is illustrated in Fig. 52.

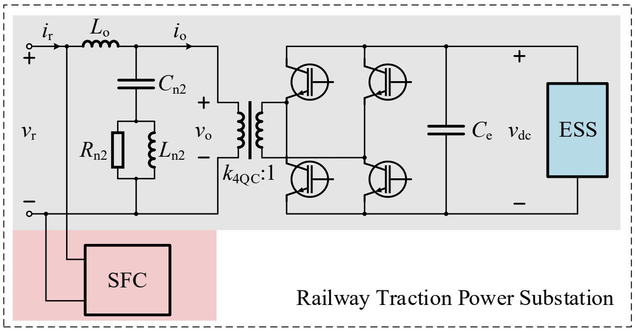

Fig. 52. Structure of DC-AC converter with ESS in simulation model

As depicted in Fig. 52, the 4QC includes an IGBT-based H-bridge and a single-phase transformer, which is characterized by its rated power (S_{4QC}), turn ratio (k_{4QC}), leakage impedance (Z_{l4QC}), and magnetization impedance (Z_{m4QC}). The DC link is equipped with an equivalent capacitor (C_e) to stabilize the DC voltage. To mitigate high-frequency harmonics induced by switching actions, a resonant filter (C_{n2}, L_{n2}, R_{n2}) is incorporated, while an output inductor (L_o) is added to form an LCL-type filter, further enhancing harmonic attenuation. The single-phase voltage and current at the TPS are denoted as v_r and i_r, respectively, while the current flowing into the transformer and the high-voltage-side voltage of the transformer are represented as i_o and v_o, respectively. The DC-link voltage is denoted as v_{dc}.

The control strategy of the 4QC is designed to ensure effective peak active power support, enable efficient recovery of braking energy, and provide dynamic reactive power compensation to maintain voltage stability within an acceptable range. The corresponding control scheme, implemented in the simulation model, is depicted in Fig. 53.

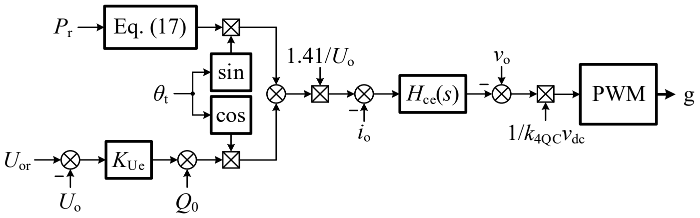

Fig. 53. Control scheme of 4QC

To optimize the active power flow and minimize abrupt disturbances in the railway traction power system, we employ a power-capping tracking strategy for the 4QC. This strategy is based on sliding mode control, which continuously adjusts the 4QC output by monitoring the TPS power in real time. By detecting fluctuations in power demand, the controller dynamically regulates the 4QC's contribution to ensure that peak power is delivered and braking energy is effectively recovered, all while maintaining a stable total active power within the TPS. This approach allows for smoother power transitions, better adaptability to sudden load variations, and greater robustness against system uncertainties and measurement noise.

The mathematical formulation of the power-capping tracking strategy is given by

$$P_{\mathrm{ESS}} = P_{\mathrm{ESSr}} - K\mathrm{sat}(S) - \lambda S \tag{17}$$

where P_{ESSr} represents the desired active power of the 4QC, S is the sliding surface, sat(S) is the saturation function, K is the sliding mode gain, and λ is the convergence law parameter.

The desired active power of the 4QC is further expressed as

$$P_{\mathrm{ESSr}} = \begin{cases} \max(0, P_{\mathrm{th}} - P_{\mathrm{r}}), & P_{\mathrm{r}} < 0 \\ P_{\mathrm{r}}, & P_{\mathrm{r}} > 0 \end{cases} \tag{18}$$

where P_{r} denotes the TPS active power, and P_{th} represents the active power threshold for the 4QC.

The saturation function is given by

$$\mathrm{sat}(S) = \begin{cases} 1, & S > \phi \\ S/\phi, & |S| \le \phi \\ -1, & S < -\phi \end{cases} \tag{19}$$

where ϕ is the boundary layer thickness.

The sliding surface S is designed as

$$S = e_{\mathrm{P}} + C\int e_{\mathrm{P}} dt \tag{20}$$

where C is a positive coefficient that regulates the system's convergence rate, and e_{P} is the power error, defined as $e_{\mathrm{P}} = P_{\mathrm{ESSr}} - P_{\mathrm{ESS}}$.

To further regulate reactive power, a V-Q droop control strategy is introduced, expressed as

$$Q_{\mathrm{ESS}} = Q_0 + K_{\mathrm{Ue}}(U_{\mathrm{or}} - U_{\mathrm{o}}) \tag{21}$$

where U_{o} is the RMS value of v_{o}, U_{or} is the nominal RMS value of v_{o}, K_{Ue} is the droop coefficient, and Q_0 is the reactive power base value.

Based on the phase angle θ_{t} of v_{o} obtained from the PLL, the current reference is generated using the calculated active and reactive power components, as depicted in Fig. 53.

Similar to the SFCs used in railway traction systems, the 4QC employs a multiple quasi-PR controller for current regulation. This controller is particularly effective in tracking the fundamental current component while simultaneously mitigating distortions caused by the third- and fifth-order harmonics. The controller is mathematically formulated as

$$H_{\mathrm{ce}}(s) = K_{\mathrm{cep}} + \sum_{n=1,3,5} \frac{2K_{\mathrm{cer}n}\omega_{\mathrm{ceb}}s}{s^2 + 2\omega_{\mathrm{ceb}}s + (n\omega_{\mathrm{r}})^2} \tag{22}$$

where K_{cep} is the proportional gain for current control, while $K_{\mathrm{cer}n}$ represents the resonant gain of quasi-PR regulator for the n-th harmonic component. The parameters ω_{ceb} corresponds to the bandwidth angular frequencies of quasi-PR regulators.

6.1.6.1.2. Simulation model of ESSs

Based on the analysis in previous section, four ESSs (Li-ion battery, EDLC, SMES, and flywheel ESS) are considered and built in this simulation model.

- Li-ion battery

In simulations, the Li-ion battery is typically represented using an equivalent electrical model to balance accuracy and computational efficiency. Among various modeling approaches, the

Thevenin-based model is the most widely used due to its ability to effectively capture battery dynamics while maintaining a reasonable level of complexity.

As illustrated in Fig. 54 (a), this model consists of a series resistor (R_{ser}) and an RC parallel network (R_{tra} and C_{tra}). This configuration allows the model to predict the battery's response to transient load variations at a given SOC while assuming a constant open-circuit voltage (V_{OC}). The inclusion of the RC parallel network accounts for the transient behavior, enabling a more realistic representation of voltage fluctuations under dynamic operating conditions.

In MATLAB/Simulink, an alternative approach is available through the built-in battery block, as shown in Fig. 54 (b). This parametric model, which is structurally similar to the Thevenin-based model, is based on equivalent circuit principles and can be directly implemented in simulations. The battery block provides flexibility in defining key parameters such as nominal voltage (v_{bn}), rated capacity (C_{bn}), initial SOC, SOC-OCV characteristics, and internal resistance (R_b). This makes it well-suited for simulating energy ESSs in power converters, facilitating accurate analysis of battery behavior in railway electrification and other energy management applications.

(a) (b)

Fig. 54. Electrical battery models: (a) Thevenin-based model, and (b) built-in battery block

- EDLC

Similarly, equivalent circuit models are widely used to represent EDLC behavior, with the RC model being one of the most practical choices due to its balance of computational efficiency and physical accuracy. As illustrated in Fig. 55 (a), this model consists of a capacitor (C) in parallel with a leakage resistor (R_{lk}) and a series resistor (R_{ESR}). The capacitor represents the core energy storage mechanism, while the series resistor accounts for ohmic losses during charge and discharge cycles. The leakage resistor models the self-discharge effect, which causes stored energy to dissipate over time.

For ease of implementation, MATLAB/Simulink provides a built-in supercapacitor block, as shown in Fig. 55 (b), which allows for parameter customization, including rated capacitance (C_{cn}), equivalent DC series resistance (R_{ESR}), rated voltage (v_{cn}), as well as the number of series (N_{ser}) and parallel capacitors (N_{par}). Additionally, users can define the initial voltage, enabling precise modeling of supercapacitor behavior in power stabilization, regenerative braking, and hybrid energy storage systems.

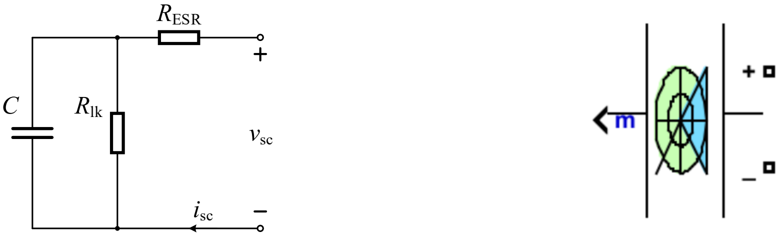

(a) (b)

Fig. 55. Electrical supercapacitor (EDLC) models: (a) RC model, and (b) built-in supercapacitor block

- SMES

In SMES systems, the superconducting magnet is typically assumed to remain in its superconducting state throughout operation. Under this condition, energy losses are negligible, allowing the magnet to be modeled as an ideal inductor in simulations. Due to its intrinsic current-source characteristics, a DC-DC chopper is employed to regulate the voltage across the magnet, ensuring the desired power exchange with the external system. This chopper not only facilitates efficient energy transfer but also effectively decouples the superconducting magnet from AC-side disturbances, enhancing system stability and protection.

As depicted in Fig. 56 (a), the power stage model of SMES consists of an inductor (L_{SM}), an H-bridge circuit comprising two IGBT switches (G_1 and G_2) and two diodes (D_1 and D_2), along with an output filter capacitor (C_{oSM}). The DC output voltage is denoted as v_{oSM}, while i_{SM} represents the current flowing through the superconducting magnet.

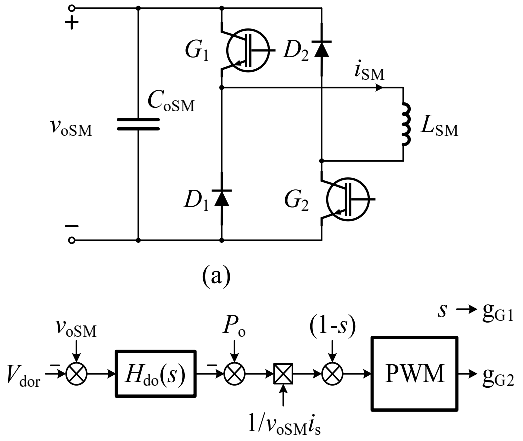

(a)

(b)

Fig. 56. SMES models: (a) power stage model, and (b) control

The DC chopper operates in two fundamental modes. In charging mode, the chopper absorbs active power from the AC side to charge the superconducting magnet. During this mode, G_1 remains continuously switched on, while G_2 alternates between on and off states. When G_2 is on, the magnet is charged through G_1 and G_2 in series. Conversely, when G_2 is off, the magnet current circulates through G_1 and D_1, maintaining continuous conduction. In discharging mode, the chopper delivers stored energy from the superconducting magnet back to the AC system. In this mode, G_1 is kept off, while G_2 continues switching. When G_2 is on, the magnet current bypasses through G_2 and D_2. When G_2 is off, the magnet discharges through diodes D_1 and D_2 to the DC link, enabling energy transfer back to the AC system. The control scheme for SMES operation is illustrated in Fig. 56 (b).

The primary objective of DC chopper control is to maintain a stable output DC voltage, ensuring that the superconducting magnet can deliver rated power, even in low-energy states. The nominal output DC voltage, denoted as V_{dor}, is designed as

$$V_{\mathrm{dor}} = V_{\mathrm{IOC}} - K_{\mathrm{do}} i_{\mathrm{s}} \tag{23}$$

where V_{IOC} represents the theoretical open-circuit voltage of the SMES, and K_{do} is the V-I droop coefficient, which regulates voltage deviations based on current variations.

To achieve precise voltage regulation, a PI controller with power feedforward compensation, denoted as $H_{do}(s)$, is implemented. The controller consists of a proportional gain (K_{dop}) and an integral gain (K_{doi}).

Since the DC chopper operates in either charging or discharging mode, the active power flowing into the chopper (P_o) serves as the switching condition for control states. Specifically, if $P_o > 0$, the system operates in charging mode ($s = 1$), while if $P_o < 0$, the system operates in discharging mode ($s = 0$). This adaptive control approach ensures seamless energy exchange between the SMES unit and the power system, enhancing overall system efficiency and reliability.

- Flywheel ESS

The flywheel ESS primarily consists of a rotor, bearing system, drive motor, and housing. To achieve a compact design and minimize mechanical vibrations, an interior permanent magnet synchronous motor (IPMSM) is directly mounted on the flywheel shaft without mechanical couplings. Compared to induction motors or brushless DC motors, an integrated IPMSM offers higher rotational speeds with lower energy losses, making it particularly suitable for high-speed energy storage applications. Consequently, controlling the flywheel ESS essentially translates to controlling the motor coupled to the flywheel.

In simulation models, the flywheel ESS is represented as an IPMSM connected to a three-phase full-bridge converter, where the flywheel's rotational inertia is incorporated into the motor's rotor dynamics, as illustrated in Fig. 57 (a). The DC link of the converter is stabilized using an equivalent capacitor (C_{oF}), ensuring a steady DC bus voltage (v_{oF}). The three-phase IPMSM armature current is denoted as i_{Mabc}.

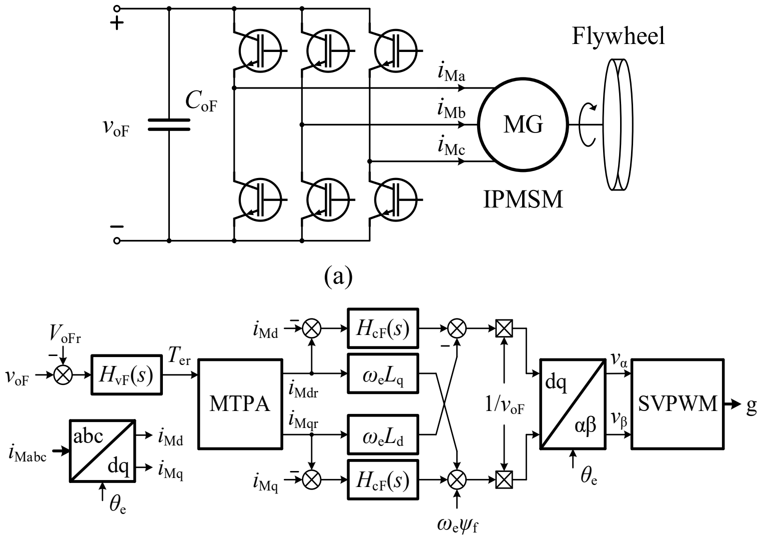

(a)

(b)

Fig. 57. Flywheel ESS models: (a) power stage model, and (b) control

The primary objective of flywheel ESS control is to maintain a constant DC bus voltage while dynamically adjusting the flywheel's rotational speed. The corresponding control structure is illustrated in Fig. 57 (b).

It is assumed that the flywheel operates within its nominal speed range, where constant torque control is implemented. Within this constant torque region, the maximum torque per ampere (MTPA) strategy is employed to optimize efficiency by minimizing current consumption. The reference q-axis armature current (i_{Mqr}) is determined by solving:

$$T_{\mathrm{er}} = \frac{3}{4} p i_{\mathrm{Mqr}} \left(\sqrt{{\psi_{\mathrm{f}}}^2 + 4(L_{\mathrm{q}} - L_{\mathrm{d}})^2 {i_{\mathrm{Mqr}}}^2} + \psi_{\mathrm{f}} \right) \tag{24}$$

where p is the number of pole pairs, ψ_{f} represents the rotor permanent magnet flux linkage, and L_{d} and L_{q} denote the d- and q-axis stator inductances, respectively.

The reference d-axis armature current (i_{Mdr}) is subsequently derived from:

$$i_{\mathrm{Mdr}} = \frac{\psi_{\mathrm{f}}}{2(L_{\mathrm{q}} - L_{\mathrm{d}})} - \sqrt{\frac{{\psi_{\mathrm{f}}}^2}{4(L_{\mathrm{q}} - L_{\mathrm{d}})^2} + {i_{\mathrm{Mqr}}}^2} \tag{25}$$

A decoupled dq-frame current control strategy is implemented to regulate the d- and q-axis armature currents, ensuring that they accurately track their respective references. This control employs a PI controller, denoted as $H_{\mathrm{cF}}(s)$, which consists of a proportional gain (K_{cFp}) and a integral gain (K_{cFi}).

The electrical angular velocity is defined as $\omega_{\mathrm{e}} = p\omega_{\mathrm{m}}$, where ω_{m} represents the mechanical angular velocity. The control signals are subsequently transformed into the αβ-frame based on the electrical angular phase: $\theta_{\mathrm{e}} = p\theta_{\mathrm{m}}$, where θ_{m} is the rotor's mechanical angle. Finally, space vector pulse-width modulation (SVPWM) is employed to generate the switching signals for the converter.

To regulate the DC bus voltage, the flywheel's rotational speed is adjusted by either accelerating or decelerating the rotor. The required torque reference (T_{er}) is obtained from a PI controller acting on the DC voltage error, where $H_{\mathrm{vF}}(s)$ is a PI controller, consisting of a proportional gain (K_{vFp}) and a integral gain (K_{vFi}), and V_{oFr} is the DC bus voltage reference.

By adjusting the flywheel's rotational speed, the system maintains a stable DC link voltage, ensuring efficient energy exchange and reliable operation of the flywheel ESS in dynamic applications.

6.1.6.1.3. Simulation verification based on case study

To evaluate the performance of the proposed converter with various ESSs in the Swedish railway traction system, the southern railway line from Malmö to Ystad is selected as a representative case study. This particular segment is more vulnerable to power quality and voltage stability issues due to the absence of 132 kV HV feeders, which makes it an ideal candidate for demonstrating the benefits of ESS integration.

In Case 3, the simulation setup mirrors that of Case 2. The parameters of the DC-link and multilevel converter are detailed in Table I and Table II, while the OCS parameters for BT and AT systems are listed in Table IV. The specifications of Rc4 (thyristor) and X61 (VSI) locomotives are provided in Table V and Table VI, respectively. The spatial distribution of train loads and TPSs is illustrated in Fig. 34. A 60 kWh ESS integrated with the proposed converter is deployed at the Malmö TPS. The technical specifications of the converter, Li-ion battery, supercapacitor, SMES, and flywheel ESS are presented in Table XI, Table XII, Table XIII, Table XIV, Table XV, respectively. Fig. 58 depicts the power profiles of individual loads.

Table XI. Parameters of proposed DC-AC converter used in simulation

PARAMETER	VALUE	PARAMETER	VALUE
Rated apparent power S_b	9 MVA	Nominal RMS voltage U_{or}	15 kV
Rated active power P_b	7.2 MW	Reactive power base value Q_0	0
Rated reactive power Q_b	5.4 MVar	Droop coefficient K_{Ue}	3000
Equivalent DC link capacitor C_e	0.24 F	Sliding mode gain K	14.4×10^6
Rated power of transformer S_{4QC}	9 MVA	Convergence law parameter λ	0.1
Turn ratio of transformer k_{4QC}	18.75/1	Active power threshold P_{th}	-9 MW
Leakage inductor of transformer L_{l4QC}	0.1 p.u.	Boundary layer thickness ϕ	28.8×10^6
Leakage resistor of transformer R_{l4QC}	0.01 p.u.	Positive coefficient C	0.1
Magnetization inductor L_{m4QC}	500 p.u.	Proportional gain K_{cep} in $H_{ce}(s)$	25.76
Magnetization resistor R_{m4QC}	500 p.u.	Resonant gain K_{cer1} in $H_{ce}(s)$	4465.6
Capacitor of resonant filter C_{n2}	10 µF	Resonant gain K_{cer3} in $H_{ce}(s)$	2359.7
Inductor of resonant filter L_{n2}	25.33 µH	Resonant gain K_{cer5} in $H_{ce}(s)$	3948.7
Resistor of resonant filter R_{n2}	50 Ω	Bandwidth angular frequency ω_{ceb}	0.2π
Output filtering inductor L_o	32 mH		

Table XII. Parameters of Li-ion battery used in simulation

PARAMETER	VALUE
Nominal voltage v_{bn}	1700 V
Rated capacity C_{bn}	40 Ah
Cut-off voltage	1275 V
Fully charged voltage	1979 V
Internal resistance R_b	0.092 Ω

Table XIII. Parameters of supercapacitor used in simulation

PARAMETER	VALUE
Rated capacitance C_{cn}	55 F
Equivalent DC series resistance R_{ESR}	15.57 mΩ
Rated voltage v_{cn}	2800 V
Number of series capacitors N_{ser}	934
Number of parallel capacitors N_{par}	18

Table XIV. Parameters of SMES used in simulation

PARAMETER	VALUE
Superconducting magnet L_{SM}	17.28 H
Output filter capacitor C_{oSM}	0.96 F
Theoretical open-circuit voltage V_{IOC}	4536 V
V-I droop coefficient K_{do}	0.6048
Proportional gain K_{dop} in $H_{do}(s)$	10^5
Integral gain K_{doi} in $H_{do}(s)$	10^7

Table XV. Parameters of flywheel ESS used in simulation

PARAMETER	VALUE
IPMSM and flywheel rotor inertia J	20 kg·m^2
Rated revolutions per minute	45000 rpm
Equivalent capacitor C_{oF}	0.96 F
Number of pole pairs p	2
Rotor permanent magnet flux linkage ψ_f	0.0506 Wb
d-axis stator inductances L_d	6 µH
q-axis stator inductances L_q	12 µH
Stator phase resistance R_s	10 mΩ
DC bus voltage reference V_{oFr}	1500 V
Proportional gain K_{vFp} in $H_{vF}(s)$	17.08
Integral gain K_{vFi} in $H_{vF}(s)$	1515.75
Proportional gain K_{cFp} in $H_{cF}(s)$	0.17
Integral gain K_{cFi} in $H_{cF}(s)$	798

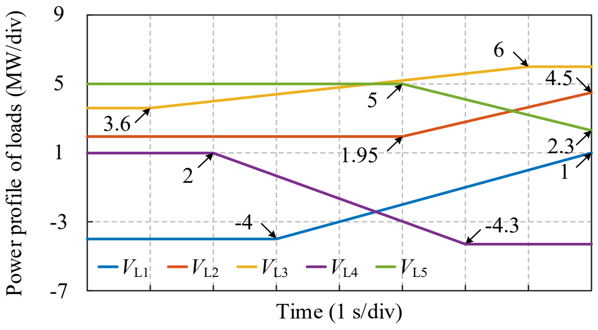

Fig. 58. Power profiles for each load in Case 3

Fig. 59 presents the simulated power exchanges between TPSs and loads with ESS integration at Malmö, where the Li-ion battery case is shown as a representative example due to the similar effects of the other ESSs on the AC-side system under standard conditions. Fig. 60 (a) contrasts the power distribution at Malmö and Ystad TPSs in both scenarios, where the active and reactive power of Malmö and Ystad TPS with ESS integration at Malmö is denoted as P_{Ma1}, P_{Ys1}, Q_{Ma1}, and Q_{Ys1}, respectively. Without ESS integration, Malmö TPS delivers no active power from 0 to 4 seconds, as the DC-link converter-based SFC is incapable of capturing regenerative braking energy. This energy is instead absorbed by distant loads through the OCS, reducing the load on Ystad TPS. Around 8 seconds, Malmö TPS reaches its negative power limit (-1 p.u.) to support local braking energy absorption.

In contrast, with ESS integration, the converter at Malmö TPS recovers regenerative braking energy during the 0 - 4 second interval, storing it in the ESS, and later discharges this energy around 8 seconds to alleviate the SFC's peak power stress. Fig. 60 (b) confirms this behavior by showing the powers of the SFC and the ESS at Malmö TPS.

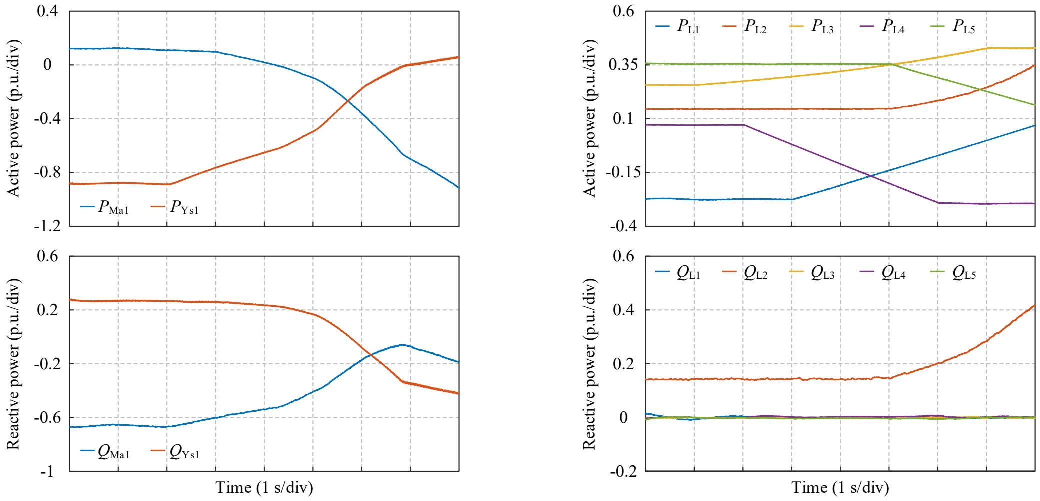

(a) (b)

Fig. 59. Powers of (a) Malmö and Ystad TPSs and (b) train loads, where the converter with ESS is integrated in Malmö TPS

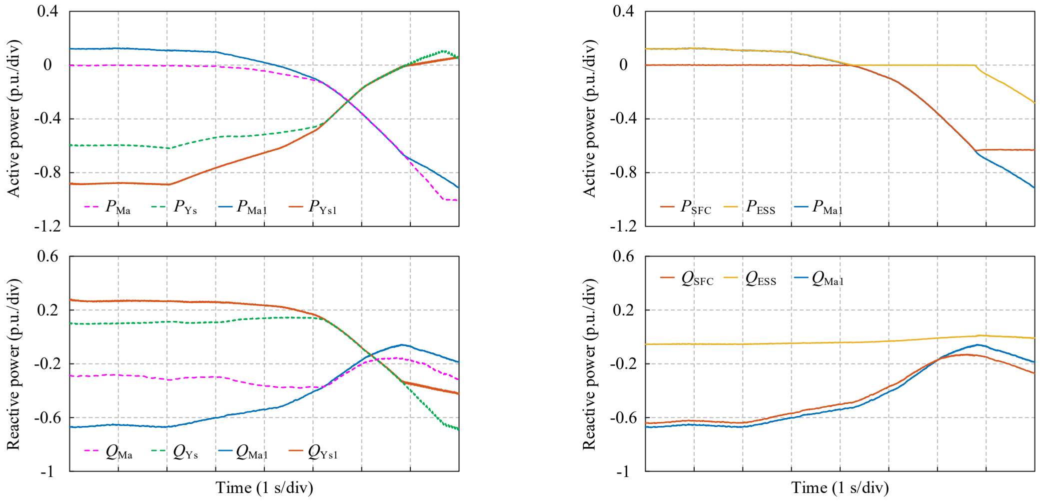

(a) (b)

Fig. 60. Power distributions (a) of Malmö and Ystad TPSs w/ or w/o ESS integration and (b) within Malmö TPS considering ESS

Fig. 61 illustrates the RMS voltages at TPSs and loads in both cases. The inclusion of the ESS slightly raises Malmö's output voltage and mitigates voltage drops around 8 seconds, maintaining the system voltage within ±10% of nominal (1.0 - 1.2 p.u.), thereby enhancing voltage stability.

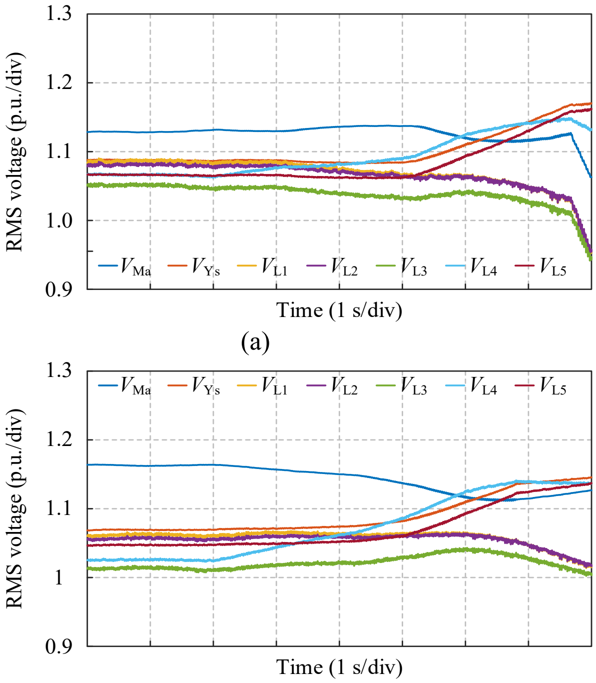

(a)

(b)

Fig. 61. RMS voltages of TPSs and loads: (a) without ESS integration in Malmö TPS and (b) with ESS integration in Malmö TPS

Fig. 62 shows the DC-link voltage and SOC of each ESS. For Li-ion batteries and supercapacitors directly interfaced with the converter DC-link, their terminal voltages reflect the link voltage. Due to internal resistance, voltage fluctuations occur with power variation. Li-ion batteries, with higher internal resistance, exhibit larger voltage swings and lower efficiency than supercapacitors, as evident from their respective SOC dynamics.

In the case of SMES, although voltage variation exists, it stems from current-dependent characteristics rather than internal resistance, thus preserving high charge/discharge efficiency. In contrast, the flywheel ESS, through its integrated converter, maintains a constant DC-link voltage, simplifying converter design and improving system performance. Its efficiency, however, is influenced by the IPMSM design and is moderate in this study.

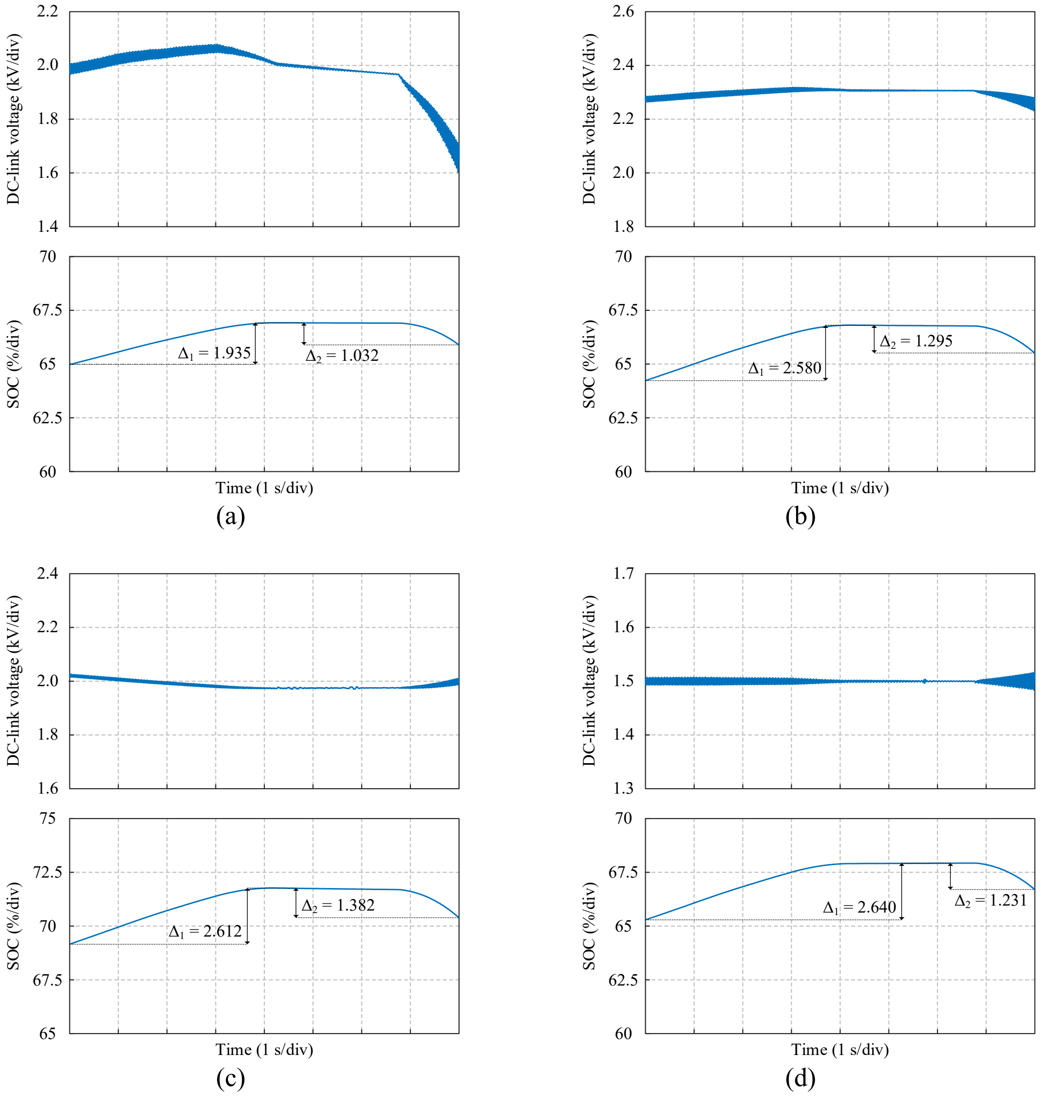

(a) (b)

(c) (d)

Fig. 62. DC-link voltage and SOC of (a) Li-ion battery, (b) EDLC, (c) SMES, and (d) flywheel ESS

In terms of cost evaluation, the effective capacity of each ESS is considered. The Li-ion battery system requires approximately 4600 cells (3.7V/4Ah, 21700 type), with about 75% usable capacity due to the converter's minimum DC-link voltage constraint. The supercapacitor system requires around 16812 units (3V/3000F), also yielding up to 75% usable capacity. For SMES, four 15 kWh/4.32 H units are used, with similar usable energy. The flywheel system employs three 20 kWh high-speed units, with an estimated usable discharge capacity of 89%, considering a lower speed limit of 15000 rpm.

These cost-performance comparisons are summarized in Table XVI. While Li-ion batteries currently offer a clear cost advantage due to declining cell prices, the analysis does not account for auxiliary components such as battery management, protection, and thermal systems. Moreover, their shorter cycle life (as shown in Fig. 44) implies higher long-term maintenance and replacement costs.

Table XVI. Evaluation of cost of ESSs used in simulation

TYPE	SPECIFICATION	TOTAL	PRICE PER CELL OR	COST	CAPACITY	ACTUAL COST

OF ESS		NUMBER	UNIT (SEK)	(SEK)	UTILIZATION	(SEK)
Li-ion battery	3.7V/4Ah cell	4600	20 – 100	0.092M – 0.46M	75%	0.123M – 0.61M
EDLC	3V/3000F cell	16812	90 – 450	1.5M – 7.5M	75%	2M – 10M
SMES	15kWh/4.32H unit	4	6M – 15M	24M – 60M	75%	32M – 80M
Flywheel ESS	20kWh unit	3	1M – 1.6M	3M – 4.8M	89%	3.37M – 5.39M

Considering factors such as efficiency, cycle life, and cost, supercapacitors and flywheel ESSs emerge as more suitable options for third-party ESS integration via DC-AC converters in parallel with existing TPS infrastructure.

6.1.6.1.4. Considering DC-DC converter

As shown in Table XVI, the available capacity of Li-ion batteries and EDLCs directly connected to the DC link of the converter is limited to approximately 75%, primarily due to the minimum DC-link voltage requirement. Additionally, the fluctuating DC-link voltage necessitates the use of high-voltage, high-current-rated components in the DC-AC converter, further increasing the overall cost of ESS integration.

To address these limitations, a bidirectional DC-DC converter can be introduced between the ESS and the DC-AC converter. The typical topologies of bidirectional DC-DC converters and their respective advantages and disadvantages have been reviewed in Section 1.1.5.2. In this study, the DAB converter is employed as a representative example to illustrate the benefits of such an integration. The power stage model of the DAB converter is shown in Fig. 63 (a). It includes two capacitors, C_{oD} on the output side and C_{iD} on the ESS side, as well as a high-frequency transformer characterized by its rated power (S_{DAB}), turns ratio (k_{DAB}), leakage impedance (Z_{lDAB}), and magnetization impedance (Z_{mDAB}), which is connected in series with an inductor L_D between two H-bridges. The voltages on the output and ESS sides of the DAB converter are denoted as v_{oD} and v_{ESS}, respectively.

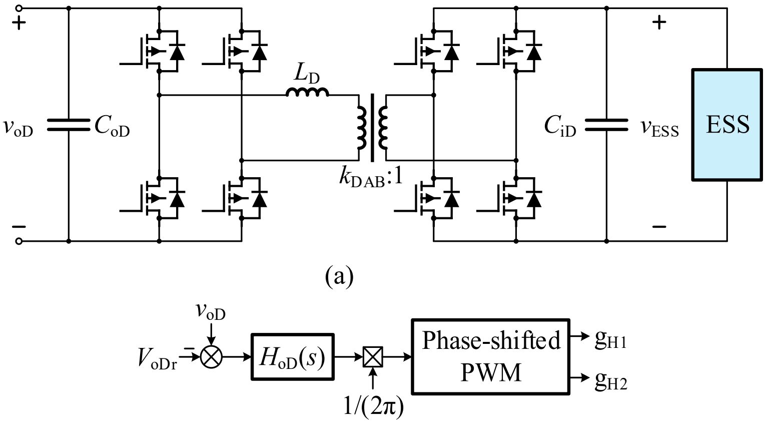

(a)

(b)

Fig. 63. DAB in simulation model: (a) power stage, and (b) control

The control objective of the DAB converter is to regulate the output DC voltage at a stable reference value. The corresponding control scheme is depicted in Fig. 63 (b), where a PI controller, $H_{oD}(s)$, consisting of proportional gain (K_{oDp}) and integral gain (K_{oDi}), is employed to achieve accurate voltage regulation. The nominal DC output voltage is denoted as V_{oDr}. The simulation parameters for the DAB converter are summarized in Table XVII.

Unlike Li-ion batteries, the usable capacity of EDLCs is highly dependent on their output voltage. Therefore, the performance of the DAB converter is evaluated using a supercapacitor (EDLC) as the connected ESS. Since the integration of a DC-DC converter does not affect the power distribution on the AC side of the system, only the output voltage of the DAB (i.e., the stabilized DC bus voltage), the EDLC terminal voltage, and its SOC are shown in (a)

(b)

Fig. 64 (a).

Table XVII. Parameters of DAB used in simulation

PARAMETER	**VALUE**
Series inductor L_D	2.43 µH
Rated power of high-frequency transformer S_{DAB}	7.2 MVA
Turn ratio of high-frequency transformer k_{DAB}	0.81/1
Leakage inductor of transformer L_{lDAB}	0.1 p.u.
Leakage resistor of transformer R_{lDAB}	0.02 p.u.
Magnetization inductor L_{mDAB}	500 p.u.
Magnetization resistor R_{mDAB}	500 p.u.
Capacitor in output side C_{oD}	0.96 F
Capacitor in ESS side C_{iD}	0.24 F
Nominal output DC voltage V_{oDr}	1500 V
Proportional gain K_{oDp} in $H_{oD}(s)$	0.05
Integral gain K_{oDi} in $H_{oD}(s)$	3

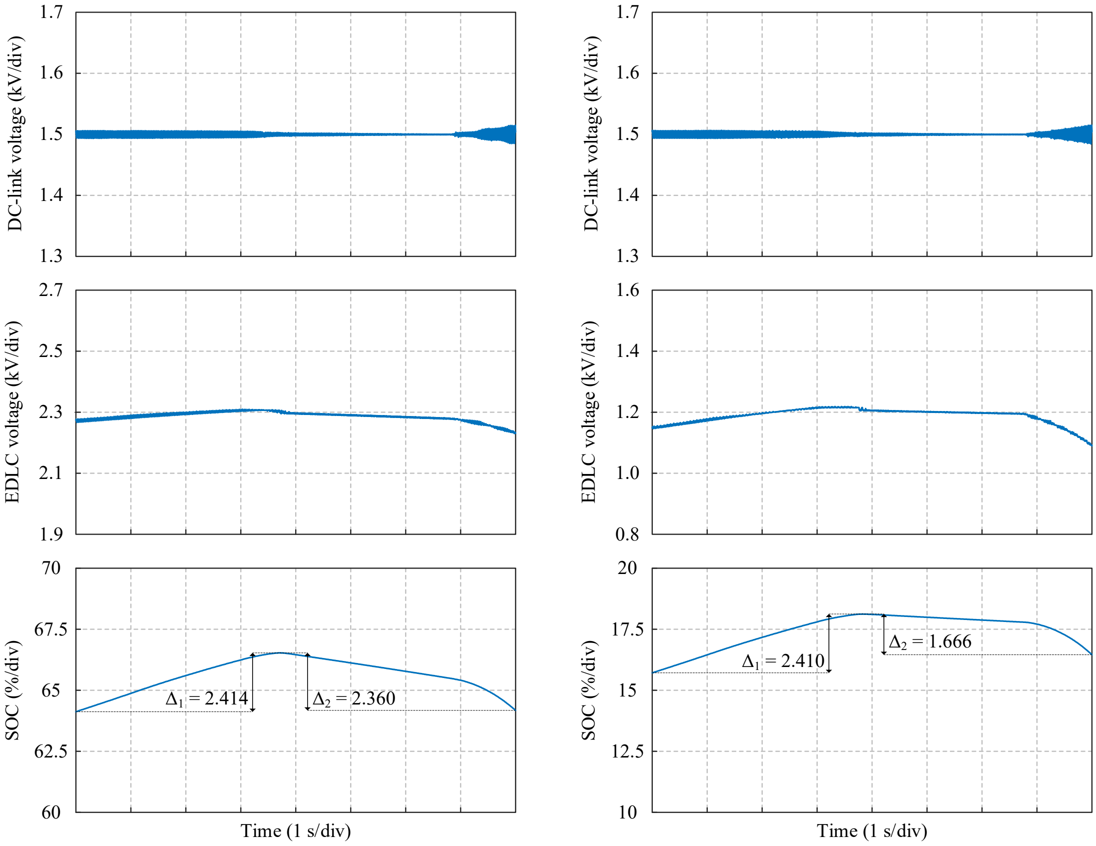

(a) (b)

Fig. 64. Output voltage of DAB converter and voltage and SOC of EDLC under (a) normal SOC condition and (b) low SOC condition

The results indicate that with the DAB converter, the DC link voltage is effectively regulated at 1500 V, and the voltage fluctuations of the EDLC are significantly reduced. This contributes to improved EDLC longevity. However, the inclusion of the DAB converter slightly impacts the charge/discharge efficiency of the EDLC, which is generally lower than the direct connection scenario.

Beyond the stability and lifetime improvements, the DAB converter also enhances the capacity utilization of the EDLC. (a) (b)

Fig. 64 (b) presents the simulation results under low SOC conditions, where the EDLC terminal voltage falls below the 1400 V minimum required by the DC-AC converter. Despite this, the DAB converter maintains the DC bus voltage at 1500 V, ensuring uninterrupted system operation.

In this setup, the allowable voltage range on the ESS side of the DAB converter is 900 - 2800 V. This extended operating range increases the theoretically utilizable capacity of the EDLC to approximately 90%. Consequently, integrating a DC-DC converter can reduce the actual cost of EDLCs, resulting in up to a 15%. Nonetheless, the DAB converter itself introduces additional costs. Therefore, the decision to integrate such a converter should be based on a comprehensive trade-off analysis between system performance requirements and economic considerations. A comparative cost evaluation of the EDLC system with and without the DC-DC converter is summarized in Table XVIII.

Table XVIII. Cost evaluation of EDLC w/ or w/o DC-DC converter

	TOTAL NUMBER	PRICE PER CELL (SEK)	CAPACITY UTILIZATION	ACTUAL COST (SEK)
EDLC without DC-DC converter	16812	90 – 450	75%	2M – 10M
EDLC with DC-DC converter			90%	1.68M – 8.4M

6.1.6.2. Proposed control strategy of multilevel converter with ESSs for Swedish railway traction system

The real-world current characteristics of the Ystad traction substation over a one-month period are illustrated in Fig. 65. The data reveals that the ratio between the maximum load current and the half-load current reaches up to 7.5, while peak loads typically occur for only a few minutes per day. These short-duration high-power demands are critical considerations in the design of TPSs, particularly for three-phase industrial grid infrastructures.

Furthermore, as demonstrated in Case 3, the Ystad substation is capable of feeding regenerative braking energy back into the industrial grid under specific operating conditions. However, this energy feedback is currently unprofitable and may induce disturbances in the grid.

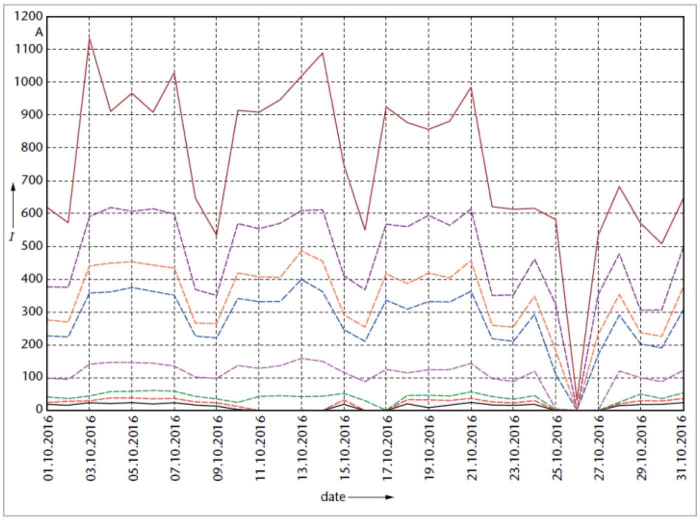

Fig. 65. Current characteristics for Ystad substation: black for minimum, red for 1%, green for 10%, magenta for 50%, blue for 90%, orange for 95%, purple for 99%, and brown for maximum [119]

Given these observations, integrating an ESS capable of capturing regenerative braking energy and shaving transient peak power is a promising approach for enhancing energy efficiency in railway TPSs. One method, previously discussed in Section 1.1.6.1, involves the addition of a parallel DC-AC converter with an ESS. This solution enables both energy recovery and improved voltage stability. However, it also introduces challenges such as increased installation and maintenance costs, as well as spatial constraints, which limit its practical deployment.

6.1.6.2.1. Design and control of existing SFC access to ESSs

To address these issues, this section proposes a more cost-effective strategy: integrating the ESS directly into existing SFCs within TPSs. Compared to the approach involving additional converters, this solution significantly reduces both installation and maintenance expenses.

Taking the multilevel converter at the Ystad substation as an example, the proposed architecture incorporates the ESS within each submodule of the converter, as illustrated in Fig. 66.

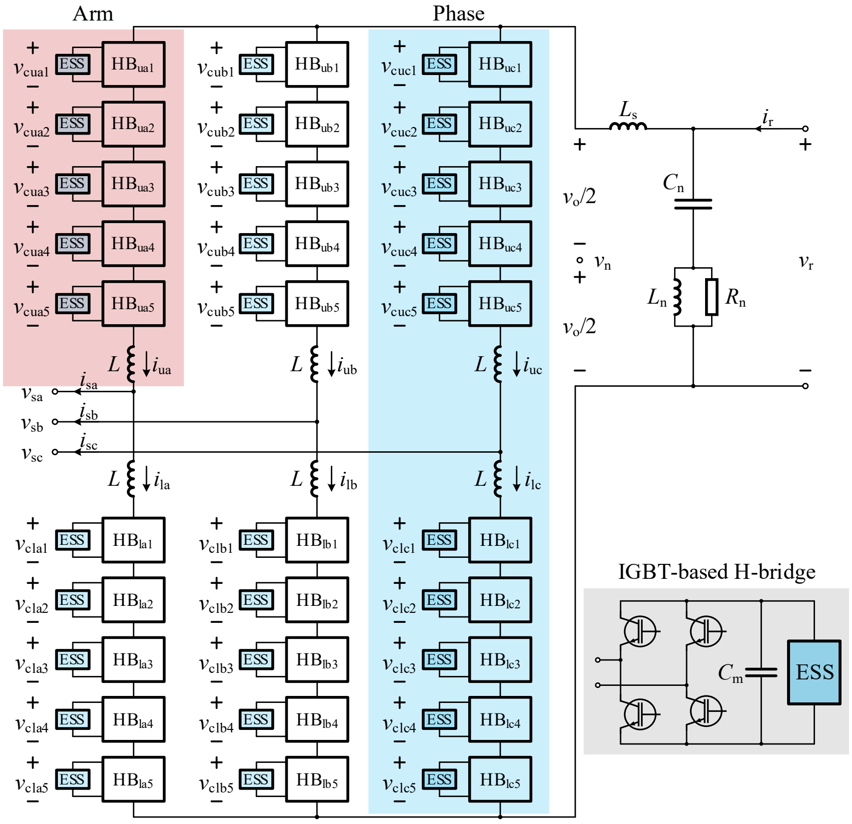

Fig. 66. Power stage schematic of multilevel converter with ESS in each module

The corresponding control scheme is shown in Fig. 71. Compared to the scheme in Fig. 15, the regulation of the overall module voltage is replaced with ESS power control to manage the charge/discharge behavior. A finite control set model predictive control (FCS-MPC) strategy is employed to enhance system dynamics and expand the allowable voltage range of the ESS. In the PVBC, the total voltage of each phase is no longer controlled to a constant reference but to the average of the module voltages in order to equalize them across the phases.

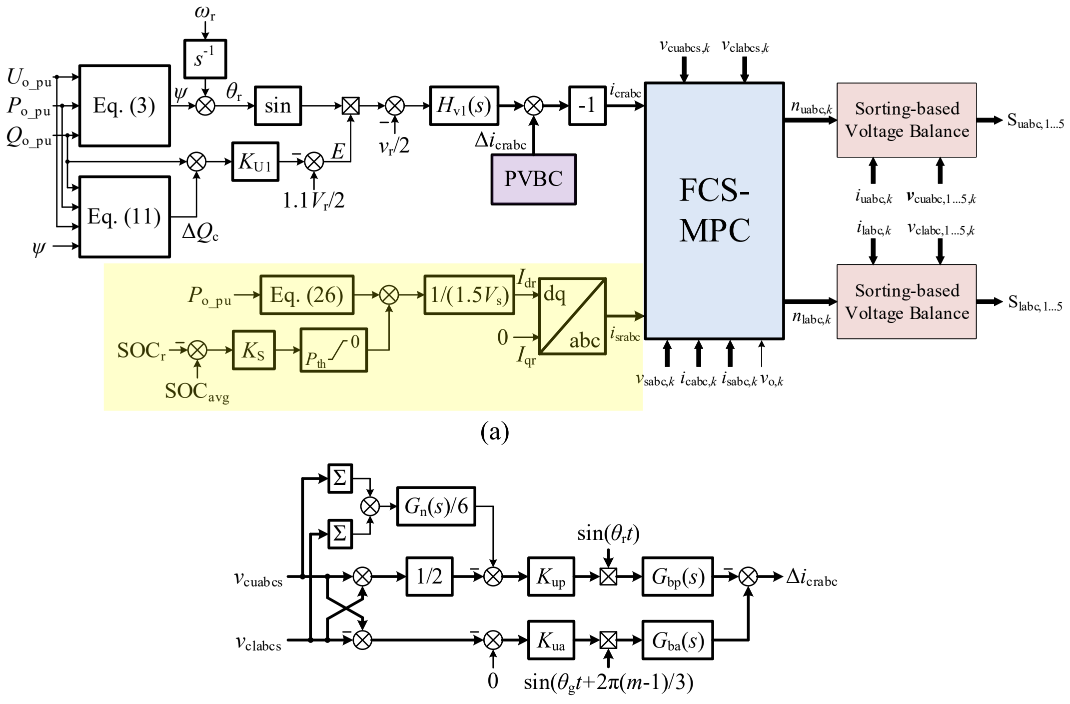

(a)

(b)

Fig. 67. Control scheme of multilevel converter integrating ESS in the modules: (a) overall control, and (b) PVBC

To achieve regenerative braking energy recovery and peak power shaving, the ESS is controlled to absorb all regenerative power when the converter output is positive. Conversely, when the output power is negative and below a defined threshold P_{th}, the ESS compensates for the power gap. This control logic is formulated as

$$P_{dr} = \begin{cases} (P_{o\_pu}P_b - P_{th})G_{HPF}(s) + P_{th}, & P_o < P_{th} \\ P_{o\_pu}P_b, & P_{th} \le P_o < 0 \\ 0, & P_o \ge 0 \end{cases} \tag{26}$$

where $G_{HPF}(s) = T_c s/(1+T_c s)$ represents a high-pass filter with time constant T_c.

Additionally, the control strategy includes a SOC regulation mechanism that ensures the average ESS SOC, denoted as SOC_{avg}, tracks a reference SOC_r. This is achieved through a proportional gain K_S, which can be dynamically adjusted, for example, to enable charging during periods of low electricity prices. To avoid interference with peak shaving and energy recovery functions, the control output is constrained within the range [P_{th}, 0].

FCS-MPC is a particularly promising technique for multilevel converters due to its capability to manage multiple control objectives and system complexities. In this work, FCS-MPC is used to improve transient performance and extend the ESS voltage operating range by considering the neutral-point voltage v_n on the single-phase side.

Based on an averaged model, the dynamic equations for injected and circulating currents are

$$\frac{L}{2}\frac{di_{sx}}{dt} + \frac{R}{2}i_{sx} = v_n - \frac{v_{ux} - v_{lx}}{2} - v_{sx} \tag{27}$$

$$L\frac{di_{cx}}{dt}+Ri_{cx}=\frac{v_{\mathrm{o}}}{2}-\frac{v_{\mathrm{u}x}+v_{\mathrm{l}x}}{2} \tag{28}$$

where $x = \mathrm{a, b, c}$, and $v_{\mathrm{u}x}$, $v_{\mathrm{l}x}$ are the upper and lower arm voltages, respectively.

In a balanced three-phase three-wire system, the sum of the injected currents is zero: $i_{\mathrm{sa}} + i_{\mathrm{sb}} + i_{\mathrm{sc}} = 0$, which leads to the neutral point voltage:

$$v_{\mathrm{n}}=\frac{1}{6}\sum_{x=\mathrm{a,b,c}}(v_{\mathrm{u}x}-v_{\mathrm{l}x}) \tag{29}$$

Assuming balanced capacitor voltages, the arm voltages are related to the insertion levels $n_{\mathrm{u}x}$, $n_{\mathrm{l}x}$ and summed module voltages $v_{\mathrm{cus}x}$, $v_{\mathrm{cls}x}$ as

$$\begin{cases} v_{\mathrm{u}x}=\dfrac{n_{\mathrm{u}x}}{N}v_{\mathrm{cus}x}, & n_{\mathrm{u}x}\in\left[-N,\ldots,0,\ldots,N\right] \\ v_{\mathrm{l}x}=\dfrac{n_{\mathrm{l}x}}{N}v_{\mathrm{cls}x}, & n_{\mathrm{l}x}\in\left[-N,\ldots,0,\ldots,N\right] \end{cases} \tag{30}$$

where $n_{\mathrm{u}x}$, $n_{\mathrm{l}x}$ and $v_{\mathrm{cus}x}$, $v_{\mathrm{cls}x}$ are insertion levels and sum of module capacitor voltages for the upper and lower arms in each phase.

Using forward Euler approximation with sampling time T_{s}, the discrete-time state-space model is

$$\mathbf{x}_{k+1}=\mathbf{A}\mathbf{x}_k+\mathbf{B}\mathbf{X}_k\mathbf{T}\mathbf{u}_k+\mathbf{d}_k \tag{31}$$

where $\mathbf{x}_k = [\mathbf{i}_{\mathrm{sabc},k}, \mathbf{i}_{\mathrm{cabc},k}]^{\mathrm{T}}$ is the state vector, $\mathbf{u}_k = [\mathbf{n}_{\mathrm{uabc},k}, \mathbf{n}_{\mathrm{labc},\,k}]^{\mathrm{T}}$ is the input vector, and $\mathbf{d}_k = [-(2T_{\mathrm{s}}/L)\mathbf{v}_{\mathrm{sabc},k}, (T_{\mathrm{s}}/2/L)v_{\mathrm{o},k}\mathbf{I}_{1\times 3}]^{\mathrm{T}}$ is the disturbance vector. Each term in these vectors is defined as a three-phase variable extended into a vector of dimensions 1 × 3, e.g., $\mathbf{i}_{\mathrm{sabc},k} = [i_{\mathrm{sa},k}, i_{\mathrm{sb},k}, i_{\mathrm{sc},k}]$. Additionally, $\mathbf{I}_{m\times n}$ and $\mathbf{O}_{m\times n}$ represent identity and zero matrices of dimensions $m \times n$, respectively, where $\mathbf{I}_n$ and $\mathbf{O}_n$ are shorthand notations for square matrices ($m = n$).

Subsequently, the matrices in (31) are expressed as follows:

$$\mathbf{A}=\begin{bmatrix}(1-\dfrac{T_{\mathrm{s}}R}{L})\mathbf{I}_3 & \mathbf{O}_3 \\ \mathbf{O}_3 & (1-\dfrac{T_{\mathrm{s}}R}{L})\mathbf{I}_3\end{bmatrix} \tag{32}$$

$$\mathbf{B}=\begin{bmatrix}-\dfrac{T_{\mathrm{s}}}{3NL}(3\mathbf{I}_3-\mathbf{G}) & \dfrac{T_{\mathrm{s}}}{3NL}(3\mathbf{I}_3-\mathbf{G}) \\ -\dfrac{T_{\mathrm{s}}}{2NL}\mathbf{I}_3 & \dfrac{T_{\mathrm{s}}}{2NL}\mathbf{I}_3\end{bmatrix} \tag{33}$$

$$\mathbf{X}_k=\mathrm{diag}(\mathbf{x}_k) \tag{34}$$

$$\mathbf{T}=\begin{bmatrix}\mathbf{I}_3 & \mathbf{O}_3 \\ \mathbf{O}_3 & \mathbf{I}_3\end{bmatrix} \tag{35}$$

where **G** represents a 3 × 3 all-ones matrix.

A cost function based on the ℓ_1-norm is defined to select the optimal set of insertion indices by minimizing tracking errors of injected and circulating currents:

$$J_k = \lambda_1 \left\| \mathbf{x}^{(1)}_{k+1} - \mathbf{x}^{(1)}_{\mathrm{r},k+1} \right\|_1 + \lambda_2 \left\| \mathbf{x}^{(2)}_{k+1} - \mathbf{x}^{(2)}_{\mathrm{r},k+1} \right\|_1 \tag{36}$$

where the reference vector is defined as $\mathbf{x}_{\mathrm{r},k} = [\mathbf{i}_{\mathrm{srabc},k}, \mathbf{i}_{\mathrm{crabc},k}]$, and $\mathbf{i}_{\mathrm{srabc},k}$, $\mathbf{i}_{\mathrm{crabc},k}$ are the reference sub-vectors for three-phase injected and circulating currents, respectively.

The reference vectors are obtained via Lagrange extrapolation. For each possible combination of n_{ux} and n_{lx}, the predicted behavior is evaluated using (31), and the one minimizing J is selected.

A modified sorting-based submodule voltage (or SOC) balancing algorithm is integrated into the control. The process, illustrated in Fig. 68, ensures effective module voltage management based on arm current direction and insertion level. Depending on whether charging or discharging is required, the submodules are sorted in ascending or descending order of their voltages, respectively, and the appropriate modules are inserted accordingly.

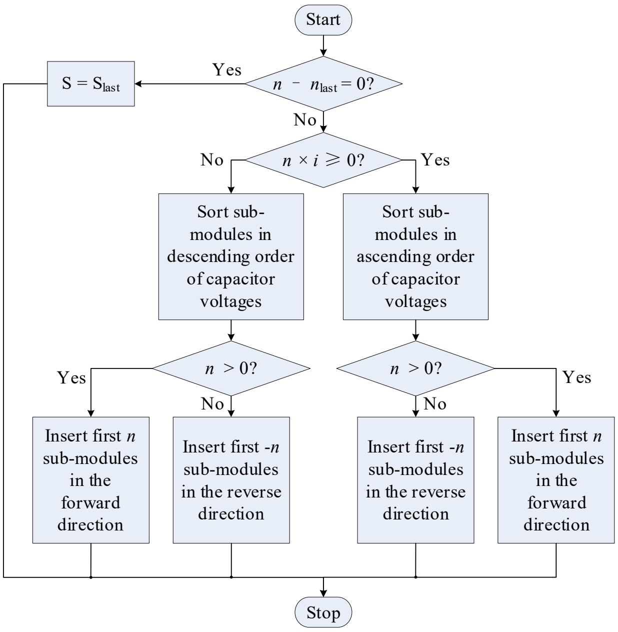

Fig. 68. Flow chart of sorting-based voltage balancing algorithm

6.1.6.2.2. Simulation verification based on case study

Case 3 is further employed to evaluate the performance of the proposed multilevel converter with integrated ESS in a Swedish railway traction power system. The parameters of the DC-link converter are provided in Table I, while the characteristics of the OCS for the BT and AT systems are listed in Table IV. Locomotive specifications for Rc4 and X61 are summarized in Table V and Table VI, respectively. The distance between train loads and TPSs is shown in Fig. 34, and the power profiles of individual loads are depicted in Fig. 58. A portion of the parameters for the proposed multilevel converter with ESS integration is listed in Table II, while the remaining parameters relevant to ESS power control and the FCS-MPC strategy are provided in Table XIX.

Table XIX. Parameters of ESS power control and FCS-MPC strategy for proposed multilevel converter with ESS integration

PARAMETER	VALUE
Active power threshold P_{th}	-6.8 MW
Time constant T_c in $G_{\mathrm{HPF}}(s)$	0.01
Weighting factor λ_1	1
Weighting factor λ_2	1.58

Although all four previously discussed ESS technologies could theoretically be integrated into this system, practical constraints, such as installation space and system compatibility, make Li-ion batteries and EDLCs more suitable for this application. In this study, EDLCs are used to demonstrate the impact of ESS integration into the multilevel converter via simulation.

Assuming a total design usable capacity of 60 kWh for the EDLC integrated into the multilevel converter, the usable capacity per submodule is set to 2 kWh (equivalent to 7.2 MJ). Similar to DC-link converters, the multilevel converter also imposes a minimum operating voltage constraint on each module. For this simulation, the submodule operating voltage is defined between 4500 V and 5500 V. Based on this voltage range and energy capacity, the required capacitance for each supercapacitor is calculated as 1.63 F. The detailed specifications of the supercapacitor are provided in Table XX.

Table XX. Parameters of supercapacitor installed in each module

PARAMETER	VALUE
Rated capacitance C_{cn}	1.63 F
Equivalent DC series resistance R_{ESR}	0.275 Ω
Rated voltage v_{cn}	5500 V
Number of series capacitors N_{ser}	1834
Number of parallel capacitors N_{par}	2

Fig. 69 presents the simulated power profiles of the TPS and load, where EDLCs are integrated into the multilevel converter at the Ystad substation. Since this integration does not increase overall system capacity, it does not directly improve power distribution or voltage stability. This is confirmed by the simulation results in Fig. 69 and Fig. 70, which show power and voltage behavior similar to those observed in the case without ESS integration. The system still operates under power limitations at a single station and experiences significant voltage fluctuations.

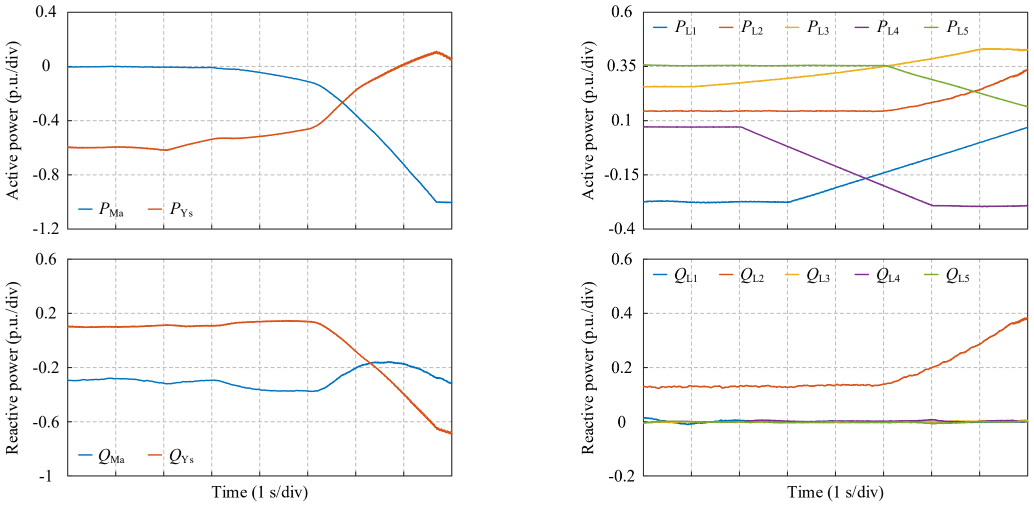

(a) (b)

Fig. 69. Powers of (a) Malmö and Ystad TPSs and (b) train loads, where the EDLCs are integrated in multilevel converter at Ystad TPS

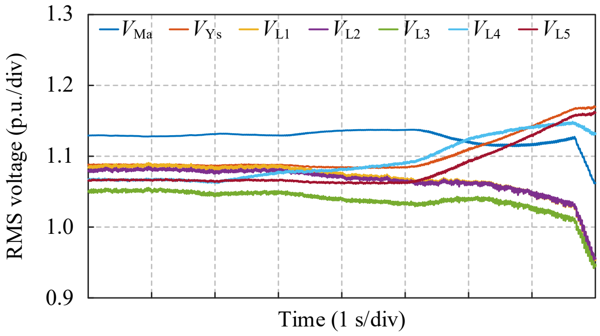

Fig. 70. RMS voltages of TPSs and loads when multilevel converter at Ystad TPS is integrated with EDLCs

Nevertheless, a key advantage of integrating EDLCs within the multilevel converter is demonstrated in Fig. 71 (a). The power drawn from the three-phase industrial grid is limited to a maximum of -0.5 p.u., and the residual power demand of the traction system is compensated by the EDLC. This is reflected in the decline of average module voltage and SOC between 0 and 4 seconds, as shown in Fig. 71 (b). Conversely, during regenerative braking (7–8 seconds), the recovered energy is not injected into the industrial grid but instead used to recharge the EDLC, as shown by the increase in module voltage and SOC in the same figure.

These results clearly demonstrate that modifying existing SFCs to incorporate ESS allows for full utilization of regenerative braking energy. This, in turn, contributes to reducing both capital and operational costs of TPSs while promoting energy efficiency.

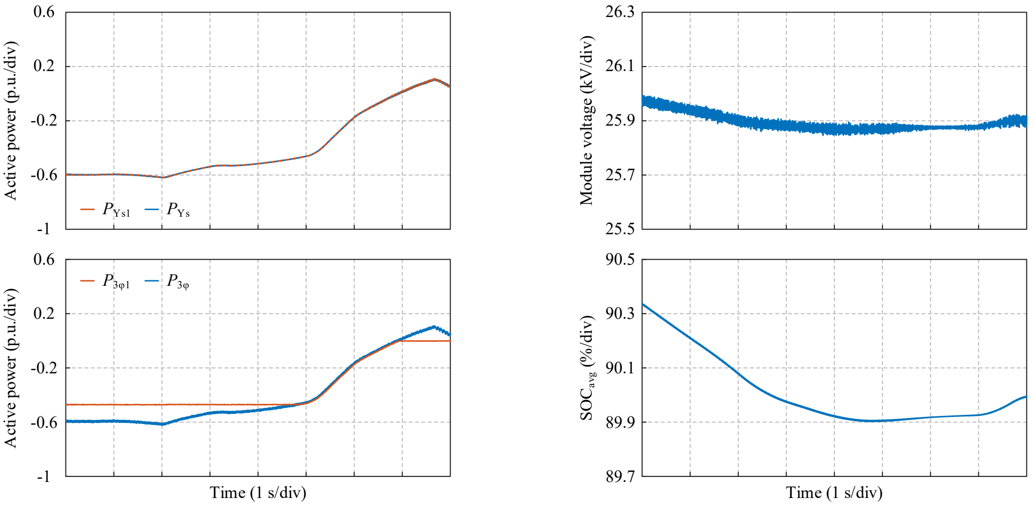

(a) (b)

Fig. 71. Simulated results of (a) single-phase side and three-phase side active power with or without EDLCs integrated in multilevel converter, and (b) averaged module voltage and SOC

Beyond improved dynamic response, another significant advantage of FCS-MPC, especially when accounting for the neutral-point voltage v_n, is its ability to expand the operating voltage range of submodules, thereby increasing the available capacity of the integrated EDLC.

Simulation results for the FCS-MPC-controlled multilevel converter with EDLC, operating continuously at rated active power under low SOC conditions, are shown in Fig. 72. The corresponding steady-state waveforms and FFT spectra of single-phase voltage and phase-a current are presented in Fig. 73. These results reveal minimal waveform distortion, with the DC component of the single-phase output voltage measured at only 2.5 V, which is negligible. Moreover, the THD for the single-phase output voltage and phase-a current are 0.575% and 0.452%, respectively, well below the 5% limit typically required for grid compliance.

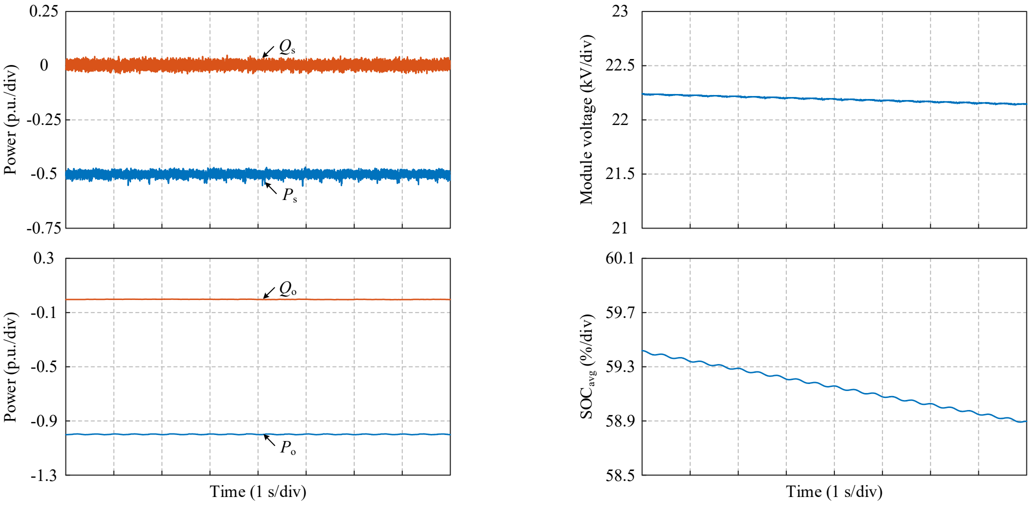

(a) (b)

Fig. 72. Simulated results of multilevel converter using FCS-MPC under low SOC condition: (a) three-phase and single-phase side power, and (b) averaged module voltage and SOC

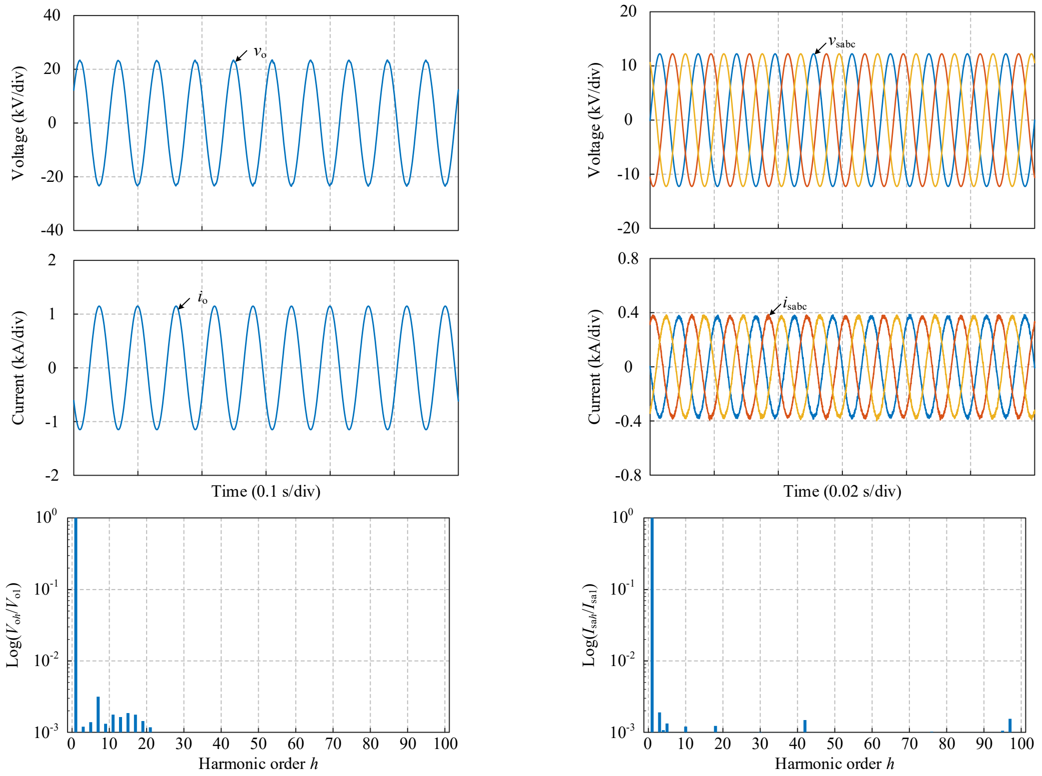

(a) (b)

Fig. 73. Performance of converter using FCS-MPC under low SOC condition: (a) single-phase side voltage and current and voltage spectrum, and (b) three-phase side voltages and currents and phase-a current spectrum

For comparison, simulation results using conventional current control under the same low SOC condition are shown in Fig. 74. Significant harmonic oscillations can be observed on the three-phase power side. Corresponding steady-state waveforms and FFT spectra are provided in Fig. 75. While the output voltage on the single-phase side shows slight distortion, the three-phase injected current exhibits severe harmonic content. Spectral analysis indicates that the THD of the single-phase output voltage and phase-a current are 1.339% and 16.327%, respectively, with the latter dominated by low-order harmonics.

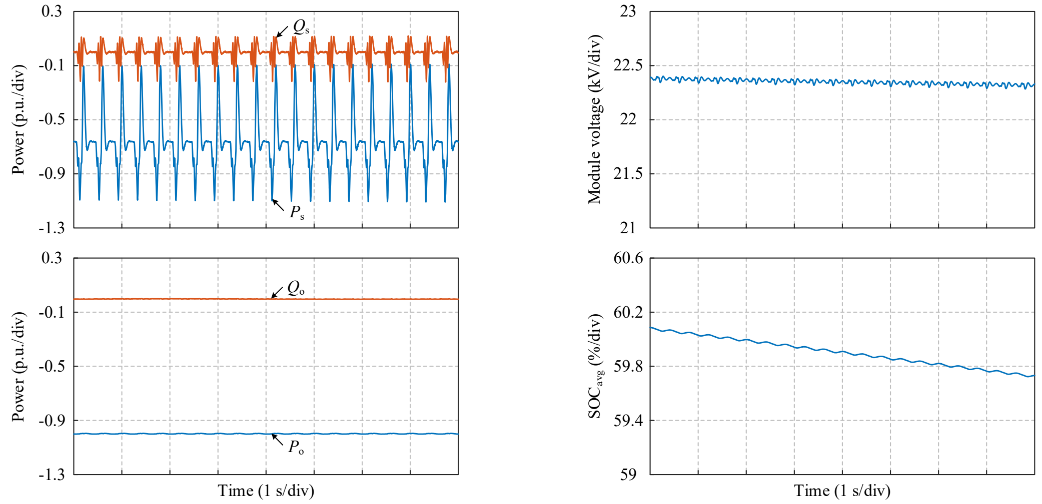

(a) (b)

Fig. 74. Simulated results of converter using conventional current control under low SOC condition: (a) three-phase and single-phase side power, and (b) averaged module voltage and SOC

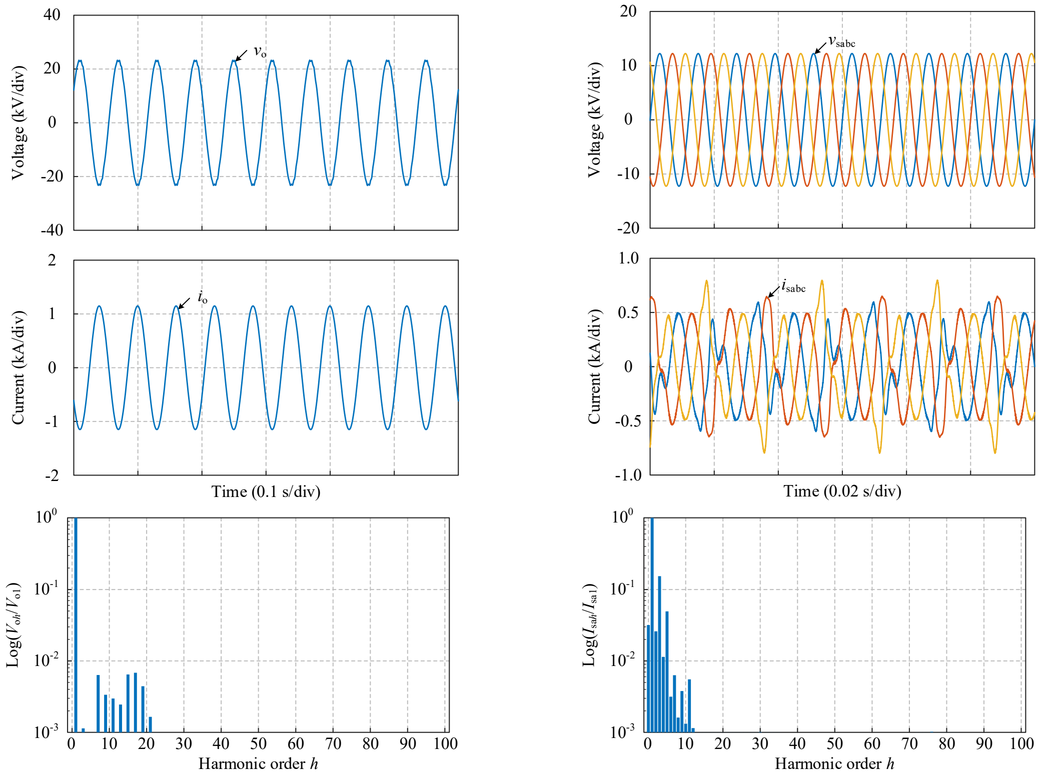

(a) (b)

Fig. 75. Performance of converter using conventional current control under low SOC condition: (a) single-phase side voltage and current and voltage spectrum, and (b) three-phase side voltages and currents and phase a current spectrum

Under these low-voltage (SOC) conditions, integrating ESSs via conventional current-controlled multilevel converters degrades single-phase voltage quality and introduces considerable harmonics into the three-phase currents. This makes the converter unsuitable for grid connection and non-compliant with standard power quality requirements.

Furthermore, the allowable submodule voltage range with FCS-MPC is extended from 4500 V to 5500 V, whereas traditional current control restricts this range to 5000 V to 5500 V. As a result, the usable energy capacity of the EDLC is fully utilized under FCS-MPC (100% utilization), but only 52.5% is accessible with traditional current control. This inefficiency leads to a 1.9-fold increase in the actual cost per unit of usable energy. A comparative cost analysis between the FCS-MPC and conventional control schemes is summarized in Table XXI.

Table XXI. Cost evaluation between the FCS-MPC and conventional current control schemes

	TOTAL NUMBER	PRICE PER CELL (SEK)	CAPACITY UTILIZATION	ACTUAL COST (SEK)
EDLC integrated in multilevel converter using conventional current control	110040	50 – 250	52.5%	10.5M – 52.4M
EDLC integrated in multilevel			100%	5.5M – 27.5M

converter using FCS-MPC		

8. Conclusions

In this work, a comprehensive global simulation model of the Swedish railway traction power system has been successfully developed based on real-world field data. The system-level model incorporates detailed sub-models of static frequency converters, covering both DC-link and multilevel converter topologies, as well as electrical locomotives, overhead catenary systems, HV feeder lines, and traction transformers. The accuracy and reliability of the model have been validated through two representative case studies: one involving a single SFC under varying operating conditions to verify key performance metrics, and the other simulating two large-scale, real-world systems, namely the northern traction corridor from Bastuträsk to Boden and the southern network originating from Malmö.

Building upon this simulation platform, advanced energy storage solutions and corresponding interface converter technologies have been explored to address voltage instability and power quality challenges in railway traction systems. Through a thorough investigation of energy storage technologies and their practical applicability for WESS deployment, four technologies, including Li-ion batteries, EDLCs, flywheel ESS, and SMES, were selected for detailed analysis. Among them, EDLCs and FESS emerged as the most promising candidates due to their high power density, fast response capability, and favorable efficiency characteristics. However, Li-ion batteries, despite their declining cell prices, remain the most costly per cycle due to their relatively limited lifecycle.

To support these ESSs, a dedicated DC-AC converter topology was developed and integrated in parallel with the existing TPSs. The system was evaluated through simulations under various configurations, with the same design capacity applied to each ESS. The results show that flywheels offer the highest capacity utilization, while Li-ion batteries present a cost advantage due to market trends. Nevertheless, when considering lifecycle, efficiency, and overall cost, EDLCs and flywheels demonstrate superior suitability. Additionally, the integration of a bidirectional DC-DC converter into the ESS interface was evaluated using EDLCs as a case study. This integration enhanced the usable energy capacity and reduced the overall ESS cost, albeit at the expense of added converter complexity and cost.

In parallel, a novel approach was proposed to integrate ESSs directly into existing SFCs to enable peak power shaving and effective utilization of regenerative braking energy. This minimizes the load on the three-phase industrial grid. Using a multilevel converter equipped with EDLCs as an example, an FCS-MPC strategy was implemented and benchmarked against traditional control methods. The results demonstrate that FCS-MPC significantly improves dynamic response, suppresses harmonics, and maximizes energy utilization. Specifically, it enables near-complete use of the EDLC's design capacity, whereas conventional control achieves only about half, leading to higher operational costs and lower efficiency.

In summary, the developed system-level model and proposed ESS integration strategies present a validated and cost-effective pathway to enhance the reliability, energy efficiency, and power quality of the Swedish railway traction network. Future work will focus on finalizing the optimal ESS installation capacity and placement, guided by insights from the completed comparative assessments.

9. References

[1] Brenna, Morris, Federica Foiadelli, and Dario Zaninelli. Electrical railway transportation systems. John Wiley & Sons, 2018.

[2] Steimel, Andreas. "Power-electronics issues of modern electric railway systems." Advances in Electrical and Computer Engineering 10, no. 2 (2010): 3-10.

[3] Aeberhard, M., C. Courtois, and Philippe Ladoux. "Railway traction power supply from the state of the art to future trends." SPEEDAM 2010 (2010): 1350-1355.

[4] Schmid, F., C. J. Goodman, and C. Watson. "Overview of electric railway systems." In 7th IET Professional Development Course on Railway Electrification Infrastructure and Systems (REIS 2015), pp. 1-15. IET, 2015.

[5] Kaleybar, Hamed Jafari, Morris Brenna, Federica Foiadelli, Seyed Saeed Fazel, and Dario Zaninelli. "Power quality phenomena in electric railway power supply systems: An exhaustive framework and classification." Energies 13, no. 24 (2020): 6662.

[6] Ufert, M. "Static frequency converters for use in 50 Hz railway traction power supply substations." Computers in Railways XV: Railway Engineering Design and Operation 162 (2016): 203.

[7] Bueno, Alexander, Jose M. Aller, Jose A. Restrepo, Ronald Harley, and Thomas G. Habetler. "Harmonic and unbalance compensation based on direct power control for electric railway systems." IEEE Transactions on Power Electronics 28, no. 12 (2013): 5823-5831.

[8] Olofsson, Magnus. "Power flow analysis of the Swedish railway electrical system." PhD diss., KTH Royal Institute of Technology, 1993.

[9] Abrahamsson, Lars, Daniel Serrano Jimenez, John Laury, and Math Bollen. "AC Cables Strengthening Railway Low Frequency AC Power Supply Systems." In ASME/IEEE Joint Rail Conference, vol. 50718, p. V001T09A004. American Society of Mechanical Engineers, 2017.

[10] Mahmood, Yasser Ahmed, Alireza Ahmadi, Ramin Karim, Uday Kumar, Ajint Verma, and Niklas Fransson. "Comparison of frequency converter outages: a case study on Swedish TPS system." In World Academy of Science, Engineering and Technology Conference, 2012.

[11] Sagareli, Sergo, and Vitaly Gelman. "Implementation of new technologies in traction power systems." In ASME/IEEE Joint Rail Conference, vol. 41634, pp. 141-146. 2004.

[12] Gunselmann, Walter. "Technologies for increased energy efficiency in railway systems." In 2005 European conference on power electronics and applications, pp. 10-pp. IEEE, 2005.

[13] Rufer, Alfred, David Hotellier, and Philippe Barrade. "A supercapacitor-based energy storage substation for voltage compensation in weak transportation networks." IEEE Transactions on power delivery 19, no. 2 (2004): 629-636.

[14] De-Leon, S., and D. Turner. "Understanding rail wayside energy storage requirements and relative costs for high-power, high-cyclable technologies." Metro Report International (2017).

[15] Mitali, J., S. Dhinakaran, and A. A. Mohamad. "Energy storage systems: A review." Energy Storage and Saving 1, no. 3 (2022): 166-216.

[16] Ratniyomchai, Tosaphol, Stuart Hillmansen, and Pietro Tricoli. "Recent developments and applications of energy storage devices in electrified railways." IET Electrical Systems in Transportation 4, no. 1 (2014): 9-20.

[17] Hossain, Eklas, Hossain Mansur Resalat Faruque, Md Samiul Haque Sunny, Naeem Mohammad, and Nafiu Nawar. "A comprehensive review on energy storage systems: Types, comparison, current scenario, applications, barriers, and potential solutions, policies, and future prospects." Energies 13, no. 14 (2020): 3651.
[18] Krishan, Om, and Sathans Suhag. "An updated review of energy storage systems: Classification and applications in distributed generation power systems incorporating renewable energy resources." International Journal of Energy Research 43, no. 12 (2019): 6171-6210.
[19] Ghaviha, Nima, Javier Campillo, Markus Bohlin, and Erik Dahlquist. "Review of application of energy storage devices in railway transportation." Energy Procedia 105 (2017): 4561-4568.
[20] Díaz-González, Francisco, Andreas Sumper, Oriol Gomis-Bellmunt, and Roberto Villafáfila-Robles. "A review of energy storage technologies for wind power applications." Renewable and sustainable energy reviews 16, no. 4 (2012): 2154-2171.
[21] Koohi-Fayegh, Seama, and Marc A. Rosen. "A review of energy storage types, applications and recent developments." Journal of Energy Storage 27 (2020): 101047.
[22] Vazquez, Sergio, Srdjan M. Lukic, Eduardo Galvan, Leopoldo G. Franquelo, and Juan M. Carrasco. "Energy storage systems for transport and grid applications." IEEE Transactions on industrial electronics 57, no. 12 (2010): 3881-3895.
[23] IEC, electrical energy storage. Switzerland: International Electrotechnical Commission; 2011.
[24] Novales, Margarita. "Light rail systems free of overhead wires." Transportation research record 2219, no. 1 (2011): 30-37.
[25] Hajiabady, Siavash. "Energy storage system for railway applications & analysis and modelling of electrochemical batteries for conductor rail gap DC railway." PhD diss., University of Birmingham, 2014.
[26] Rahman, Md Mustafizur, Abayomi Olufemi Oni, Eskinder Gemechu, and Amit Kumar. "Assessment of energy storage technologies: A review." Energy Conversion and Management 223 (2020): 113295.
[27] Carnegie, Rachel, Douglas Gotham, David Nderitu, and Paul V. Preckel. "Utility scale energy storage systems." State Utility Forecasting Group. Purdue University 1 (2013): 27.
[28] Cunha, Álvaro, Jorge Martins, Nuno Rodrigues, and F. P. Brito. "Vanadium redox flow batteries: a technology review." International Journal of Energy Research 39, no. 7 (2015): 889-918.
[29] Cavanagh, Kate, J. K. Ward, Sam Behrens, Anand Bhatt, E. L. Ratnam, Erin Oliver, and J. Hayward. "Electrical energy storage: technology overview and applications." Australia:[sn] (2015).
[30] IEA. Prospects for large-scale energy storage in decarbonised power grids. Paris: International Energy Agency; 2009.
[31] Chen, Haisheng, Thang Ngoc Cong, Wei Yang, Chunqing Tan, Yongliang Li, and Yulong Ding. "Progress in electrical energy storage system: A critical review." Progress in natural science 19, no. 3 (2009): 291-312.
[32] Winter, Carl-Jochen. "Hydrogen energy—Abundant, efficient, clean: A debate over the energy-system-of-change." International journal of hydrogen energy 34, no. 14 (2009): S1-S52.
[33] Nikolaidis, Pavlos, and Andreas Poullikkas. "Cost metrics of electrical energy storage technologies in potential power system operations." Sustainable Energy Technologies and Assessments 25 (2018): 43-59.

[34] UIC, Keeping Climate Change Solutions on Track. The role of rail. 2010.
[35] Fedele, Emanuele, Diego Iannuzzi, and Andrea Del Pizzo. "Onboard energy storage in rail transport: Review of real applications and techno-economic assessments." IET electrical systems in transportation 11, no. 4 (2021): 279-309.
[36] Akhoundzadeh, M. Haji, S. Panchal, E. Samadani, K. Raahemifar, M. Fowler, and R. Fraser. "Investigation and simulation of electric train utilizing hydrogen fuel cell and lithium-ion battery." Sustainable Energy Technologies and Assessments 46 (2021): 101234.
[37] Luo, Xing, Jihong Wang, Mark Dooner, and Jonathan Clarke. "Overview of current development in electrical energy storage technologies and the application potential in power system operation." Applied energy 137 (2015): 511-536.
[38] Akhil, Abbas Ali, Georgianne Huff, Aileen B. Currier, Benjamin C. Kaun, Dan M. Rastler, Stella Bingqing Chen, Andrew L. Cotter, Dale T. Bradshaw, and William D. Gauntlett. DOE/EPRI electricity storage handbook in collaboration with NRECA. No. SAND2015-1002. Sandia National Lab.(SNL-NM), Albuquerque, NM (United States), 2015.
[39] Evans, Annette, Vladimir Strezov, and Tim J. Evans. "Assessment of utility energy storage options for increased renewable energy penetration." Renewable and sustainable energy reviews 16, no. 6 (2012): 4141-4147.
[40] González-Gil, Arturo, Roberto Palacin, and Paul Batty. "Sustainable urban rail systems: Strategies and technologies for optimal management of regenerative braking energy." Energy conversion and management 75 (2013): 374-388.
[41] Gay, Sebastien E., and Mehrdad Ehsani. "On-board electrically peaking drive train for electric railway vehicles." In Proceedings IEEE 56th vehicular technology conference, vol. 2, pp. 998-1001. IEEE, 2002.
[42] Barrero, Ricardo, Xavier Tackoen, and Joeri Van Mierlo. "Stationary or onboard energy storage systems for energy consumption reduction in a metro network." Proceedings of the Institution of Mechanical Engineers, Part F: Journal of Rail and Rapid Transit 224, no. 3 (2010): 207-225.
[43] Miyatake, Masafumi, Hiroto Haga, and Satoshi Suzuki. "Optimal speed control of a train with on-board energy storage for minimum energy consumption in catenary free operation." In 2009 13th European conference on power electronics and applications, pp. 1-9. IEEE, 2009.
[44] Miyatake, Masafumi, and Kunihiko Matsuda. "Energy saving speed and charge/discharge control of a railway vehicle with on-board energy storage by means of an optimization model." IEEJ Transactions on Electrical and Electronic Engineering 4, no. 6 (2009): 771-778.
[45] Agenjos, Elena, Antonio Gabaldon, Francisco G. Franco, Roque Molina, Sergio Valero, Mario Ortiz, and Rafael J. Gabaldon. "Energy efficiency in railways: Energy storage and electric generation in diesel electric locomotives." In CIRED 2009-20th International Conference and Exhibition on Electricity Distribution-Part 1, pp. 1-7. IET, 2009.
[46] Arboleya, Pablo, Islam El-Sayed, Bassam Mohamed, and Clement Mayet. "Modeling, simulationand analysis of on-board hybrid energy storage systems for railway applications." Energies 12, no. 11 (2019): 2199.
[47] Chen, Junyu, Haitao Hu, Yinbo Ge, Ke Wang, Wenlong Huang, and Zhengyou He. "An energy storage system for recycling regenerative braking energy in high-speed railway." IEEE Transactions on Power Delivery 36, no. 1 (2020): 320-330.

[48] Maher, Bobby. "Ultracapacitors provide cost and energy savings for public transportation applications." Battery Power Product & Technology 10, no. 6 (2006): 27.

[49] Brenna, Morris, Vittorio Bucci, Maria Carmen Falvo, Federica Foiadelli, Alessandro Ruvio, Giorgio Sulligoi, and Andrea Vicenzutti. "A review on energy efficiency in three transportation sectors: Railways, electrical vehicles and marine." Energies 13, no. 9 (2020): 2378.

[50] Konishi, Takeshi, Hiroaki Morimoto, Toru Aihara, and Masaru Tsutakawa. "Fixed energy storage technology applied for DC electrified railway." IEEJ Transactions on Electrical and Electronic Engineering 5, no. 3 (2010): 270-277.

[51] Ise, Toshifumi, Masanori Kita, and Akira Taguchi. "A hybrid energy storage with a SMES and secondary battery." IEEE Transactions on Applied Superconductivity 15, no. 2 (2005): 1915-1918.

[52] Chang, Xiaoyong, Yongli Li, Weiya Zhang, Nan Wang, and Wei Xue. "Active disturbance rejection control for a flywheel energy storage system." IEEE Transactions on Industrial Electronics 62, no. 2 (2014): 991-1001.

[53] Abad, Gonzalo, ed. Power electronics and electric drives for traction applications. John Wiley & Sons, 2016.

[54] Schupbach, Roberto M., and Juan C. Balda. "Comparing DC-DC converters for power management in hybrid electric vehicles." In IEEE International Electric Machines and Drives Conference, 2003. IEMDC'03., vol. 3, pp. 1369-1374. IEEE, 2003.

[55] Gorji, Saman A., Hosein G. Sahebi, Mehran Ektesabi, and Ahmad B. Rad. "Topologies and control schemes of bidirectional DC–DC power converters: An overview." IEEE access 7 (2019): 117997-118019.

[56] Chakraborty, Sajib, Hai-Nam Vu, Mohammed Mahedi Hasan, Dai-Duong Tran, Mohamed El Baghdadi, and Omar Hegazy. "DC-DC converter topologies for electric vehicles, plug-in hybrid electric vehicles and fast charging stations: State of the art and future trends." Energies 12, no. 8 (2019): 1569.

[57] Jayasinghe, SD Gamini, D. Mahinda Vilathgamuwa, and Udaya K. Madawala. "Diode-clamped three-level inverter-based battery/supercapacitor direct integration scheme for renewable energy systems." IEEE Transactions on Power Electronics 26, no. 12 (2011): 3720-3729.

[58] Teston, Silvio Antonio, Marcello Mezaroba, and Cassiano Rech. "ANPC inverter with integrated secondary bidirectional DC port for ESS connection." IEEE Transactions on Industry Applications 55, no. 6 (2019): 7358-7367.

[59] Baruschka, Lennart, and Axel Mertens. "Comparison of cascaded H-bridge and modular multilevel converters for BESS application." In 2011 IEEE Energy Conversion Congress and Exposition, pp. 909-916. IEEE, 2011.

[60] Kawakami, Noriko, Satoru Ota, Hironobu Kon, Shuji Konno, Hirofumi Akagi, Hiromu Kobayashi, and Naotaka Okada. "Development of a 500-kW modular multilevel cascade converter for battery energy storage systems." IEEE Transactions on Industry Applications 50, no. 6 (2014): 3902-3910.

[61] B. Wang and G. Venkataramanan, "Dynamic Voltage Restorer Utilizing a Matrix Converter and Flywheel Energy Storage," in IEEE Transactions on Industry Applications, vol. 45, no. 1, pp. 222-231, Jan.-feb. 2009

[62] Guo, Wenyong, Dafei Li, Fuyu Cai, Chuang Zhao, and Liye Xiao. "Z-source-converter-based power conditioning system for superconducting magnetic energy storage system." IEEE Transactions on Power Electronics 34, no. 8 (2018): 7863-7877.

[63] Kim, Kwang-Seop, Sung-Ho Lee, Woo-Jun Cha, Jung-Min Kwon, and Bong-Hwan Kwon. "Bidirectional single power-conversion DC–AC converter with noncomplementary active-clamp circuits." IEEE Transactions on Industrial Electronics 63, no. 8 (2016): 4860-4867.

[64] Ibanez, Federico Martin. "Bidirectional series resonant DC/AC converter for energy storage systems." IEEE Transactions on Power Electronics 34, no. 4 (2018): 3429-3444.

[65] Daoud, Mohamed I., Ahmed M. Massoud, Ayman Samy Abdel-Khalik, Ahmed Elserougi, and Shehab Ahmed. "A flywheel energy storage system for fault ride through support of grid-connected VSC HVDC-based offshore wind farms." IEEE Transactions on Power Systems 31, no. 3 (2015): 1671-1680.

[66] Deng, Wenli, Chaohua Dai, Weirong Chen, and H. Zhang. "Research progress of railway power conditioner." CSEE 40 (2020): 4640-4655.

[67] G. Anqi, Hu Haitao, Z. Yuwei, C. Junyu, Ge Yinbo, Control strategy of HESS for electrified railway based on step energy management, J. Electr. Technol. 36 (23) (2021) 4916–4925.

[68] Yaai, Chen, Lin Yankang, Wang Sai, and Zhou Jinghua. "Optimal control strategy of hybrid energy storage based on filter allocation method." transactions of china electrotechnical society 35, no. 19 (2020): 4009-4018.

[69] Li, Xiangjun. "Fuzzy adaptive Kalman filter for wind power output smoothing with battery energy storage system." IET Renewable Power Generation 6, no. 5 (2012): 340-347.

[70] H. Xiaojuan, C. Yueyan, Z. Hao, et al., Application of hybrid energy storage technology based on wavelet packet decomposition in stabilizing power fluctuation of wind farms, China J. Electr. Eng. 33 (19) (2013) 8–13. +24.

[71] Feng, Xue, H. B. Gooi, and S. X. Chen. "Hybrid energy storage with multimode fuzzy power allocator for PV systems." IEEE Transactions on Sustainable Energy 5, no. 2 (2014): 389-397.

[72] Chong, Lee Wai, Yee Wan Wong, Rajprasad Kumar Rajkumar, and Dino Isa. "An optimal control strategy for standalone PV system with Battery-Supercapacitor Hybrid Energy Storage System." Journal of Power Sources 331 (2016): 553-565.

[73] Cabrane, Zineb, Mohammed Ouassaid, and Mohamed Maaroufi. "Battery and supercapacitor for photovoltaic energy storage: a fuzzy logic management." IET Renewable Power Generation 11, no. 8 (2017): 1157-1165.

[74] L. Yuyan, Y. Zhongping, L. Fei, et al., Sun Hu. Research on adaptive energy management and capacity optimization of urban rail ground HESS, J. Electr. Technol. 36 (23) (2021) 4874–4884.

[75] Garcia-Torres, Felix, and Carlos Bordons. "Optimal economical schedule of hydrogen-based microgrids with hybrid storage using model predictive control." IEEE Transactions on Industrial Electronics 62, no. 8 (2015): 5195-5207.

[76] Novak, Hrvoje, Vinko Lešić, and Mario Vašak. "Hierarchical coordination of trains and traction substation storages for energy cost optimization." In 2017 IEEE 20th International Conference on Intelligent Transportation Systems (ITSC), pp. 1-6. IEEE, 2017.

[77] Hredzak, Branislav, Vassilios G. Agelidis, and Minsoo Jang. "A model predictive control system for a hybrid battery-ultracapacitor power source." IEEE Transactions on Power Electronics 29, no. 3 (2013): 1469-1479.

[78] Wei, Wenjing, Haitao Hu, Ke Wang, J. Chen, and Z. He. "Energy storage scheme and control strategies of high-speed railway based on railway power conditioner." Transactions of China Electrotechnical Society 34, no. 6 (2019): 1290-1299.

[79] Luo, Pei, Weimin Yang, and Min Zhang. "Optimization of Negative Sequence Current in Public Power Grid under Regenerative Braking Condition of High Speed Railway." China Railway Science 39, no. 6 (2018): 126-132.

[80] Hillers, André, and Jürgen Biela. "Optimal design of the modular multilevel converter for an energy storage system based on split batteries." In 2013 15th european conference on power electronics and applications (epe), pp. 1-11. IEEE, 2013.

[81] M. Qian, G. Xin, L. Pei, et al., A new railway power regulator based on super capacitor ESS, J. Electr. Technol. 33 (06) (2018) 1208–1218.

[82] Lamedica, Regina, Alessandro Ruvio, Laura Palagi, and Nicola Mortelliti. "Optimal siting and sizing of wayside energy storage systems in a DC railway line." Energies 13, no. 23 (2020): 6271.

[83] Iannuzzi, Diego, Davide Lauria, and Pietro Tricoli. "Optimal design of stationary supercapacitors storage devices for light electrical transportation systems." Optimization and Engineering 13 (2012): 689-704.

[84] UIC - international union of railways, technologies - stationary energy storage. https://www.railway-energy.org/tfee/index.php?ID=220&TECHNOLOGYID=50&SEL=210&SEKTION=Sec4_closed#a_Economic%20criteria.

[85] Meishner, Fabian, and Dirk Uwe Sauer. "Wayside energy recovery systems in DC urban railway grids." ETransportation 1 (2019): 100001.

[86] Siemens AG. Increasing energy efficiency optimized traction power supply in mass transit systems. https://kipdf.com/rail-electrification_5ac3f2361723dd3a8f78ae1c.html; 2011.

[87] Radcliffe, Paul, James S. Wallace, and Lily H. Shu. "Stationary applications of energy storage technologies for transit systems." In 2010 IEEE Electrical Power & Energy Conference, pp. 1-7. IEEE, 2010.

[88] Mongird, Kendall, Vilayanur V. Viswanathan, Patrick J. Balducci, Md Jan E. Alam, Vanshika Fotedar, V. S. Koritarov, and Boualem Hadjerioua. Energy storage technology and cost characterization report. No. PNNL-28866. Pacific Northwest National Laboratory (PNNL), Richland, WA (United States), 2019.

[89] Aneke, Mathew, and Meihong Wang. "Energy storage technologies and real life applications–A state of the art review." Applied Energy 179 (2016): 350-377.

[90] Zhao, Haoran, Qiuwei Wu, Shuju Hu, Honghua Xu, and Claus Nygaard Rasmussen. "Review of energy storage system for wind power integration support." Applied energy 137 (2015): 545-553.

[91] Mahlia, Teuku Meurah Indra, T. J. Saktisahdan, Ali Jannifar, Muhammad Heikal Hasan, and H. S. C. Matseelar. "A review of available methods and development on energy storage; technology update." Renewable and sustainable energy reviews 33 (2014): 532-545.

[92] Sabihuddin, Siraj, Aristides E. Kiprakis, and Markus Mueller. "A numerical and graphical review of energy storage technologies." Energies 8, no. 1 (2014): 172-216.

[93] IEC, electrical energy storage. Switzerland: International Electrotechnical Commission; 2011. https://www.iec.ch/basecamp/electrical-energy-storage.

[94] Taylor, Peter, Ronan Bolton, Dave Stone, Xiao-Ping Zhang, Chris Martin, and Paul Upham. "Pathways for energy storage in the UK." Report for the centre for low carbon futures, York (2012).

[95] Olabi, Abdul Ghani, C. Onumaegbu, Tabbi Wilberforce, Mohamad Ramadan, Mohammad Ali Abdelkareem, and Abdul Hai Al–Alami. "Critical review of energy storage systems." Energy 214 (2021): 118987.

[96] Simbolotti G, Kempener R. Electricity storage. Technology brief, energy technology systems analysis programme ETSAP, international energy agency IEA, Paris (France). Bonn (Germany), Netherlands: International Renewable Energy Agency IRENA; 2012.

[97] Gür, Turgut M. "Review of electrical energy storage technologies, materials and systems: challenges and prospects for large-scale grid storage." Energy & environmental science 11, no. 10 (2018): 2696-2767.

[98] Palizban, Omid, and Kimmo Kauhaniemi. "Energy storage systems in modern grids—Matrix of technologies and applications." Journal of Energy Storage 6 (2016): 248-259.

[99] Nadeem, Furquan, SM Suhail Hussain, Prashant Kumar Tiwari, Arup Kumar Goswami, and Taha Selim Ustun. "Comparative review of energy storage systems, their roles, and impacts on future power systems." IEEE access 7 (2018): 4555-4585.

[100] Zakeri, Behnam, and Sanna Syri. "Electrical energy storage systems: A comparative life cycle cost analysis." Renewable and sustainable energy reviews 42 (2015): 569-596.

[101] Faias, Sérgio, Patrícia Santos, Jorge Sousa, and Rui Castro. "An overview on short and long-term response energy storage devices for power systems applications." RE&PQJ 6, no. 1 (2008).

[102] Guerrero, Miguel A., Enrique Romero, Fermin Barrero, María Isabel Milanés, and Eva Gonzalez. "Supercapacitors: Alternative energy storage systems." Przeglad Elektrotechniczny 85, no. 10 (2009): 188-195.

[103] Khodaparastan, Mahdiyeh, Ahmed A. Mohamed, and Werner Brandauer. "Recuperation of regenerative braking energy in electric rail transit systems." IEEE Transactions on Intelligent Transportation Systems 20, no. 8 (2019): 2831-2847.

[104] Woojin Industrial Systems. Energy storage system for railways. https://www.wjis.co.kr/en/business/energy_storage_railway.php.

[105] Flosch. Projekt station¨arer energiespeicher landwasser abschlussbericht. https://www.badenova.de/mediapool/media/dokumente/unternehmensbereiche_1/stab_1/innovationsfonds/abschlussberichte/2012_13/2012-06_AB_Energiespeicher_Landwasser.pdf.

[106] Croset A. Energy storage for existing DC networks and catenary free solutions. https://trid.trb.org/view/1412038.

[107] Konishi, Takeshi, Hiroaki Morimoto, Toru Aihara, and Masaru Tsutakawa. "Fixed energy storage technology applied for DC electrified railway." IEEJ Transactions on Electrical and Electronic Engineering 5, no. 3 (2010): 270-277.

[108] Solis, Octavio, Frank Castro, Leonid Bukhin, Kinh Pham, David Turner, and Gary Thompson. "Saving money every day: LA metro subway wayside energy storage substation." In ASME/IEEE Joint Rail Conference, vol. 56451, p. V001T07A002. American Society of Mechanical Engineers, 2015.

[109] Tarrant CD. Kinetic energy storage: solving problems for power engineers around the world. https://www.sandia.gov/ess-ssl/EESAT/2003_papers/Tarrant.pdf.

[110] Takahashi H, Kato T, Ito T, Gunji F. Energy storage for traction power supply systems. http://www.sze.hu/~szenasy/VILLVONT/r2008_01_004.pdf.

[111] Iino, Yuuki, Hitoshi Hayashiya, Masami Hino, Shotaro Abe, Katsutoshi Nakao, and Kishin Kudo. "Evaluation of installation effect of the energy storage system in dc traction power supply system." In 2016 IEEE International Power Electronics and Motion Control Conference (PEMC), pp. 280-285. IEEE, 2016.

[112] Kawasaki. Battery power system for railways. https://global.kawasaki.com/en/energy/solutions/battery_energy/download/pdf/catalog_bps.pdf.

[113] Domínguez, M., A. Fernández-Cardador, A. Fernández-Rodríguez, A. P. Cucala, R. R. Pecharromán, P. Urosa Sánchez, and I. Vadillo Cortázar. "Review on the use of energy storage systems in railway applications." Renewable and Sustainable Energy Reviews 207 (2025): 114904.

[114] Nikolaidis, Pavlos, and Andreas Poullikkas. "A comparative review of electrical energy storage systems for better sustainability." Journal of power technologies 97, no. 3 (2017): 220-245.

[115] Ragone, David V. Review of battery systems for electrically powered vehicles. No. 680453. SAE Technical Paper, 1968.

[116] Amercan Clean Power Association, Energy Storage Association | ESA 2023. https://energystorageassociationarchive.org/.

[117] Mostafa, Mostafa H., Shady HE Abdel Aleem, Samia G. Ali, Ziad M. Ali, and Almoataz Y. Abdelaziz. "Techno-economic assessment of energy storage systems using annualized life cycle cost of storage (LCCOS) and levelized cost of energy (LCOE) metrics." Journal of Energy Storage 29 (2020): 101345.

[118] Khodaparastan, Mahdiyeh, and Ahmed Mohamed. "Flywheel vs. supercapacitor as wayside energy storage for electric rail transit systems." Inventions 4, no. 4 (2019): 62.

[119] Biedermann, Niklas, T. Schütte, K. Elschner, and C. Hinze. "Peak load management-reducing power peaks for a 1 AC 15 kV 16, 7 Hz railway." eb-Elektrische Bahnen 115 (2017): 1-12.

10. Appendices

Table A1. Technical characteristics of ESSs in academic articles

ESS	Power rating (MW)	Storage capacity (kWh)	Response time	Discharge time	Efficiency	Self discharge per day (%)	Specific energy (Wh/kg)	Specific power (W/kg)	Energy density (Wh/L)	Power density (W/L)	Lifetime	Cycle life	Ref.
Li-ion			1 s		86						10	3500	[88]
	0-0.1			min-h	90-100 (85-90)	0.1-0.3	75-200	150-315	200-500		5-15	1000-10000+	[32] ([89])
	0-0.1		<s	min-h	65-75	0.1-0.3			200-400	1300-10000	5-100	600-1200	[90]
					90-100		80-150						[91]
	0-3				70-100	0.03-0.33	30-300	8-2000	94-500	56.8-800	2-20	250-10000	[92]
			20ms-s	min-h		0.1-0.3	100-250	230-340	250-620	1300-10000	8-15	500-6000	[29]
			<s	h	85-98		60-200		200-400	1300-10000	5-15	500-10000	[93]
	1-100			0.15-1h	75-90						5-15	4000-100000	[94]
	0.1-50				78-88	1-5	80-150	245-500			14-16	1500-3500	[95]
					70-85		100-200	360				500-2000	[22]
	0.1-5	5-10	s	min-h	90		125-250		140-630		8-15	3000	[96]
	0.05-100		<s	1min-8h	85-95	0.1-0.3			200-400	1300-10000			[97]
	<100	250-25000		<1h	<90						<15		[98]

	0.05-100	250-25000	ms	1min-h	85-95	0.15-0.3	120-230	150-2000			20-25	1000-10000	[99]
	0.01			min-h	85-95	0.1-0.3	150-350	50-2000			5-15	1500-4500	[100]
	0.1		ms	min-h	85-90	0.1-0.3	75-200				5-15	4500	[39]
	5			15min-h	90						15		[30]
FESS			0.25 s		86						>20	200000	[88]
	0-0.25			ms-15min	90-95 (85-95)	100	10-30	400-1500	20-80	1000-2000	~15	20000+	[32] ([89])
	0-0.25		<s	s-h	80-90	100			20-80	5000	15-20	10000-10000000	[90]
					90		30-100						[91]
	0.001-10				70-96	24-100	5-200	400-30000	0.25-424	40-2000	15-20	1000-10000	[92]
			<4ms-s	15s-15min		20-100	5-130	400-1600	20-80	5000	>20	10000000	[29]
			<s	s	80-90		5-30		20-80	5000	15-20	20000-10000000	[93]
	0.4-20				80-95						15-20		[94]
	0.1-20				85	100	5-100	11900			20	100000-10000000	[95]
					95		5-30/>50	1000/5000				>20000	[22]
	0.01-10	1-25	s	15min	>85						20	50000-100000	[96]
	0.001-20		<s	s-min	70-95	1.3-100			20-80	5000		20000-100000	[97]
	<20	<10000	<10ms	<1h	<85						<20		[98]
	0.01-0.25	25-5000	s	s-15min	90-95	1.3-100	5-80	700-12000			15-20	20000-100000	[99]
	0.25			ms-15min	93-95	100	5-100	1000			15-20	20000-100000	[100]
	0.25			ms-15min	93-95	100	10-30				~15	>100000	[39]

	0.75-1.65			15s-15min	93						20		[30]
	<10				90							1000000	[101]
	0.005-90	0.005-200	12min		80-95						20		[102]
					~95		>50	5000				>20000	[103]
EDLC			16 ms		92						16	10^6	[88]
	0-0.3			ms-60min	90-100 (90-95)	20-40	2.5-15	500-5000	10-30	100000+	20+	100000+	[32] ([89])
	0-0.3		<s	ms-60min	85-98	20-40			10-20	40000-120000	4-12	10000-100000	[90]
					85-98		0.1-5						[91]
	0-5				65-99	0.46-40	0.07-85.6	5.44-100000	1-35	15-4500	5-20	10000-1000000	[92]
			8ms	ms-1h		2-40	0.1-15	0.1-10	10-20	40000-120000	>20	500000	[29]
			<s	s	85-98		1-15		10-20	40000-120000	4-12	10000-100000	[93]
	0-10			ms-s	75-98						8-20+	25000-1000000	[94]
	0.05-0.25						2-69	800-23600					[95]
					95		<50	4000				>50000	[22]
	0.1-10		s	s	90							50000	[96]
	0.01-1		<s	ms-min	80-95	20-40			10-20	40000-120000		10000-100000	[97]
	<1	100-500	<10ms	<1min	<95						<40		[98]
	0.01-0.3	0.001-5	ms	ms-min	85-95	10-40	0.05-15	10-1000000			25-30	100000-500000	[99]
	0.3			ms-60min	85-95	20-40	2.5-50	800-23500			10-20	>100000	[100]
	0.3			ms-60min	90-95	20-40	2.5-15				>20	>100000	[39]

	10			<30s	90							>500000	[30]
	<10				90							1000000	[101]
	<1	0.001-1	ms		>95						>10		[102]
					~95			>4000				>50000	[103]
SMES	0.1-10			ms-8s	95-98	10-15	0.5-5	500-2000	0.2-2.5	1000-4000	20+	100000+	[32] ([89])
	0.1-10		<s	ms-8s	75-80	10-15			6	2600			[90]
					97-98								[91]
	0.01-200				80-99	1-15	0.27-75	500-15000	0.2-13.8	300-4000	20-30	10000-100000	[92]
			<100ms	ms-8s		10-15	10-75	2600	0.006		20	10000-100000	[29]
			<s	s	75-80				6	2600			[93]
	0.1-10			ms-s	90-97+						20-30		[94]
					80-95	10-15					20	10000-100000	[95]
	0.1-10+				>90							50000	[96]
	0.1-1		<s	ms-s	80-95	10-15			6	2600		100000	[97]
	<10	1000-3000	<10ms	<1min	<95						<40		[98]
	0.01-10	15-100	ms	ms-s	90-97	10-15	0.5-5	500-2000			20-30	20000-100000	[99]
	0.1-10			ms-8s	95-98	10-15	0.5-5	500-2000			15-20	>100000	[100]
	0.1-10			ms-8s	95-98	10-15	0.5-5				>20	>100000	[39]
	1-3			1-3s	90							>30000	[30]
	<100				95							1000000	[101]
	0.17-100	0.11-27	ms		95						30		[102]